

Graphene: From Diffusive to Ultraclean-Interacting Systems

Inauguraldissertation

zur
Erlangung der Würde eines Doktors der Philosophie
vorgelegt der
Philosophisch-Naturwissenschaftlichen Fakultät
der Universität Basel

von

**Frank Daniel Freitag
aus Deutschland**



Basel, 2012

Genehmigt von der Philosophisch-Naturwissenschaftlichen Fakultät
auf Antrag von
Prof. Dr. C. Schönenberger
Prof. Dr. H. Bouchiat
Dr. J. Smet
Dr. J. Trbovic

Basel, 21.02.2012

Prof. Dr. Martin Spiess
Dekan

Contents

1. Introduction	1
2. The Properties of Graphene	3
2.1. Band Structure of Graphene	3
2.1.1. Single Layer Graphene	3
2.1.2. Bilayer Graphene	8
2.2. Electron-Electron Interaction in Graphene	10
3. Universal Conductance Fluctuations	13
4. Superconductivity and Andreev Reflection	17
4.1. Superconductivity	17
4.2. Andreev Reflection at the Superconductor-Graphene Interface	19
5. Quantum Hall Effect in Graphene	23
5.1. Hall Effect	23
5.2. Integer Quantum Hall Effect	24
5.3. Quantum Hall Effect in Graphene	27
6. Device Fabrication, Characterisation and Measurement Set-up	31
6.1. Graphene Flake Deposition	31
6.2. Optical Characterisation	33
6.3. Raman Spectroscopy	34
6.4. Atomic Force Microscopy on Graphene	36
6.5. Lithography and Metallisation	36
6.5.1. PMMA Mask	38
6.5.2. PMMA/MA Mask	39
6.5.3. Aluminium Oxide Sacrificial Layer	39
6.6. Suspending Graphene	40
6.7. Current Annealing	42
6.8. Measurement Set-up	43
7. Conductance Fluctuations in Graphene with Superconducting Contacts	45
7.1. Basic Transport Properties	46

7.2. Enhancement of the CF by Andreev Reflection	48
7.3. Gate-dependence of the UCF	53
7.4. Summary	54
8. Suspended Two-terminal Single Layer Graphene	57
8.1. Quantum Hall Effect and Lifted Degeneracy	58
8.2. Insulating State and Fractional Conductance Plateaus	59
8.3. The $\nu = \pm 2$ State at Vanishing Magnetic Field	62
8.4. Summary	63
9. Suspended Two-terminal Bilayer Graphene	65
9.1. Gate Response of B1 and B2	67
9.2. QHE in Suspended Bilayer Graphene Devices	67
9.3. dI/dV Spectroscopy of a Spontaneously Gapped State at Zero Magnetic Field	71
9.4. dI/dV Spectroscopy of Samples with $G_{min} \approx 4 e^2/h$	75
9.5. Summary	77
10. Suspended Bilayer Graphene Hall Crosses	79
10.1. Homogeneity of Current Annealed Bilayer Graphene Devices	79
10.2. Measurement of Quantised σ_{xy}	82
10.3. dI/dV Spectroscopy and Evolution of the Gap in Magnetic Field	87
10.4. Summary	91
11. Summary and Outlook	93
A. Flake deposition	103
B. E-beam lithography, metallisation and HF etching	105
Curriculum Vitae	109
Publications	111
Acknowledgements	113

INTRODUCTION

Graphene, a one-atom thick layer of hexagonally packed carbon, has been studied by theoreticians since the 1940's [1]. It is an ideal two-dimensional (2D) system, in which the charge carriers can be seamlessly tuned from electrons to holes. In contrast to the massive charge carriers found in most metallic or semiconducting systems, the graphene's carriers are mass-less and behave relativistic [2]. Other carbon allotropes were already well-known and experimentally studied: the 3D graphite and diamond, the 1D carbon nanotubes [3, 4] since the 1990's and the 0D Buckminster fullerene [5] since 1985. However, graphene could only be studied theoretically. It was not until 2004 that the first successful experimental isolation of graphene was reported by the Manchester-based group of A. Geim and K. Novoselov [6], who received the Nobel prize in 2010 for their discovery. The strong interest in the special properties of graphene sparked research activities mainly focusing on electronic transport and the mechanical properties of this thin membrane.

More importantly, the isolation of the graphene turned out to be a straightforward process compared to its semiconducting counterparts, since all that is needed to isolate graphene is graphite and adhesive tape to receive high quality samples. This accessibility is another reason for graphene's popularity today.

In relatively short time, graphene managed to not only be of academic interest, but also attracted industrial research [7] due to a wide range of applications, such as touch screens, microprocessors or conductive coatings.

Furthermore, when cooling to cryogenic temperatures, additional physical phenomena start influencing the electronic transport in the graphene flake. A major correction to the measured conductance stems from the so-called universal conductance fluctuations. They are found in micrometre sized samples and can be used to study the graphene. Depending on the transport-limiting length scale, differently strong developed fluctuations will manifest.

Moreover, the fact that the graphene lies openly on substrates makes it easy to contact it with various metals with different physical properties. For example,

superconducting contacts such as aluminium open a path to applications like quantum computation.

The intrinsic 2D nature of single layer graphene and bilayer graphene, which consists of two graphene layers on top each other, makes it possible to combine its novel properties with well established 2D phenomena. One of the most important physical discoveries in solid state physics in recent year is the quantum Hall effect (QHE) [8] in 2D systems. Graphene is the only material up to date, in which the QHE was observed even at room temperature [9].

In this thesis, results on the electronic transport at cryogenic temperatures for both single layer graphene and bilayer graphene will be presented. We combine universal conductance fluctuations and superconducting electrodes to study disordered graphene. Further, the quantum Hall effect in ultraclean single layer and bilayer graphene is investigated.

In **chapter 2**, the basic theory of single layer graphene and bilayer graphene is explained. The special properties of the electronic band structure and its implications for the electronic transport are explored. We then give an introduction to the universal conductance fluctuations in **chapter 3** and superconductivity in **chapter 4**. We finish the theoretical aspects in **chapter 5** with a treatment of the quantum Hall effect and its manifestation in graphene.

Chapter 6 details how our graphene devices are fabricated. It starts with the flake deposition and localisation. Raman spectroscopy is used to identify the number of graphene layers before the microfabrication of the metallic contacts. In addition, we show the fabrication of suspended graphene devices and the current annealing to obtain high quality samples.

Subsequently, we present our measurements on conductance fluctuations in single layer graphene and their interplay with superconductivity in diffusive graphene in **chapter 7**.

From there on, we remove the substrate in order to investigate ultraclean graphene. **Chapter 8** shows the QHE in two-terminal devices of free-standing single layer graphene. Two-terminal bilayer graphene is explored in **chapter 9**, where we find interaction induced effects like a spontaneously gapped state at zero magnetic field. Finally, we study the QHE in bilayer graphene in a four-terminal geometry in **chapter 10**.

THE PROPERTIES OF GRAPHENE

In this chapter an introduction to several aspects of the theoretical properties of single and bilayer graphene is given. The linear low-energy electronic band structure is treated and it is shown that single layer graphene houses relativistic charge carriers without rest-mass. Further, we touch the pseudospins and the chirality in graphene. The massive carriers and parabolic band structure of bilayer graphene are explained. In addition, we give a short overview of the electron-electron interaction in single layer and bilayer graphene.

2.1. Band Structure of Graphene

The electronic properties of graphene can be ascribed to the carbon-carbon double bonds which make up the hexagonal lattice. A free carbon atom has six electrons in a $1s^2 2s^2 2p^2$ configuration. The $1s^2$ electrons are inert and the $2s^2$ should be as well. However, the energy gain of bond formation leads to hybridisation of the $2s$ and $2p$ orbitals. In the case of a $C - C$ double bond one of the $2s$ electrons is lifted into a $2p$ orbital and two of the $2p$ orbitals hybridise with the remaining $2s$ electron into three sp^2 orbitals. The double bond is formed by overlapping one sp^2 and the $2p$ orbital of a carbon atom with the same orbitals of its neighbouring C . The sp^2 orbitals form a covalent σ -bond, whereas the $2p$ electrons form a π -bond.

In combination with the remaining two sp^2 orbitals, the carbon can form a total of three bonds. With all its neighbours being carbon as well, a hexagonal lattice of carbon atoms is formed, as shown in fig. 2.1 a). In this ring-structure, the π -orbitals are no longer firmly assigned to one double-bond, but can be considered to be de-localised and thus shared by all $C - C$ bonds in the ring.

2.1.1. Single Layer Graphene

Here, we treat a single layer of graphene and introduce its electronic properties.

2. The Properties of Graphene

In terms of crystallography, the honeycomb-arrangement of the atoms leads to a triangular Bravais lattice with a two atom basis. Fig. 2.1 a) shows the lattice and the primitive unit cell, shaded in grey, with the A and B carbon atoms. A and B can be considered to be sublattices of their own. The lattice vectors are given by:

$$\mathbf{a}_1 = \frac{a}{2} \left(3\mathbf{e}_x, \sqrt{3}\mathbf{e}_y \right), \quad \mathbf{a}_2 = \frac{a}{2} \left(3\mathbf{e}_x, -\sqrt{3}\mathbf{e}_y \right) \quad (2.1)$$

where $a \approx 1.42 \text{ \AA}$ is the $C - C$ bond length of graphite. In the reciprocal lattice, the first Brillouin zone is hexagonal, as shown in fig. 2.1 b). The reciprocal lattice vectors are

$$\mathbf{b}_1 = \frac{2\pi}{3a} \left(\mathbf{k}_x, \sqrt{3}\mathbf{k}_y \right), \quad \mathbf{b}_2 = \frac{2\pi}{3a} \left(\mathbf{k}_x, -\sqrt{3}\mathbf{k}_y \right) \quad (2.2)$$

The six corners of the Brillouin zone can be separated into two distinct, but energetically degenerate, points:

$$\mathbf{K} = \left(\frac{2\pi}{3a}, \frac{2\pi}{3\sqrt{3}a} \right) \text{ and } \mathbf{K}' = \left(\frac{2\pi}{3a}, \frac{2\pi}{-3\sqrt{3}a} \right). \quad (2.3)$$

By shifting these two points by \mathbf{b}_1 and \mathbf{b}_2 the other four corners can be constructed. It is worth noting, that \mathbf{K} and \mathbf{K}' originate from the Bravais lattice and are not a consequence of the two atoms A and B in the unit cell [10].

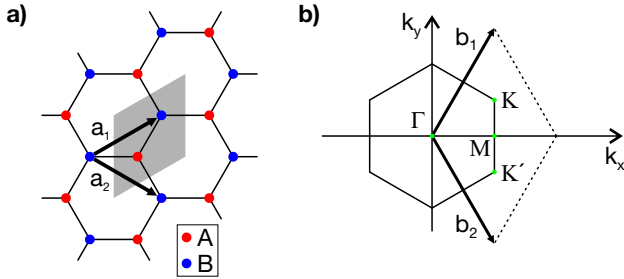


Figure 2.1.: **a)** The honeycomb lattice of graphene in real-space. A convenient primitive unit cell is shaded in grey and has the vector basis \mathbf{a}_1 and \mathbf{a}_2 . Two crystallographically distinct carbon atoms form sublattices, A and B . **b)** The first Brillouin zone of the reciprocal lattice with the base vectors \mathbf{b}_1 and \mathbf{b}_2 . The \mathbf{K} and \mathbf{K}' points are distinct.

An important energy scale is the nearest neighbour (NN) hopping energy, $t \approx 2.5 - 3 \text{ eV}$, which an electron requires to jump from A to an adjacent B .

The next nearest neighbour hopping term, where the electrons stay in the same sublattice ($A \rightarrow A$ or $B \rightarrow B$) is about one order of magnitude lower with $t' \approx 0.1$ eV [11].

The electronic band structure can be calculated in a tight-binding approximation [1]¹. We start by introducing the Wannier functions

$$\phi(\mathbf{x}) = c_1 \phi_A(\mathbf{x}) + c_2 \phi_B(\mathbf{x}), \quad (2.4)$$

where $\phi_{A,B}$ are the π orbital wavefunctions at the site of atom A or B . Given that the lattice is periodic, a Bloch wave is chosen as an Ansatz for the total wavefunction:

$$\Psi_{\mathbf{k}} = \sum_{\mathbf{R} \in G} e^{i\mathbf{k}\mathbf{R}} \phi(\mathbf{x} - \mathbf{R}), \quad (2.5)$$

where G is the lattice in real-space.

Calculating the overlap integrals and only including the nearest neighbours results in an energy dispersion of the form

$$E_{\pm}(\mathbf{k}) = \pm t \sqrt{1 + f(\mathbf{k})} \quad (2.6)$$

with

$$f(\mathbf{k}) = 4 \cos\left(\frac{3a}{2}k_x\right) \cos\left(\frac{\sqrt{3}a}{2}k_y\right) + 4 \cos^2\left(\frac{\sqrt{3}a}{2}k_y\right). \quad (2.7)$$

The $+$ ($-$) refers to the π^* (π) band, which is the conductance (valence) band.

Fig. 2.2 a) shows the dispersion relation of eq. 2.6. In un-doped graphene, the Fermi energy (E_F) lies where the two bands touch in the K and K' points and therefore the Fermi surface exists in six points. When going to larger \mathbf{k} and hence higher energy, a saddle point is reached where the six K points merge into one Fermi surface. The energy at which this occurs is the hopping term $t \approx 3$ eV and the consequence are van Hove singularities in the density of states [11].

For electron transport the states close to E_F are relevant. In order to investigate this low-energy band structure in the vicinity of the K points, a linear expansion is made around \mathbf{K} . Using $\mathbf{k} = \mathbf{K} + \kappa$ and performing a Taylor expansion around \mathbf{K} , the Eigenvalues reduce to

$$\epsilon_{\pm}(\kappa) = \pm \frac{3t}{2} a |\kappa| \quad (2.8)$$

After applying the Wannier theorem $\kappa = -i\nabla$, the energy dispersion close to the Dirac point is found to be

$$\epsilon_{\pm}(\mathbf{k}) = \hbar v_F \mathbf{k}, \quad \text{with } v_F = \frac{3ta}{2\hbar} \approx 10^6 \text{ m/s} \quad (2.9)$$

¹A more pedagogical derivation was made by Prof. Schönenberger and is available under <http://nanoelectronics.unibas.ch/education/Nanotubes/LCAO-NT.pdf>

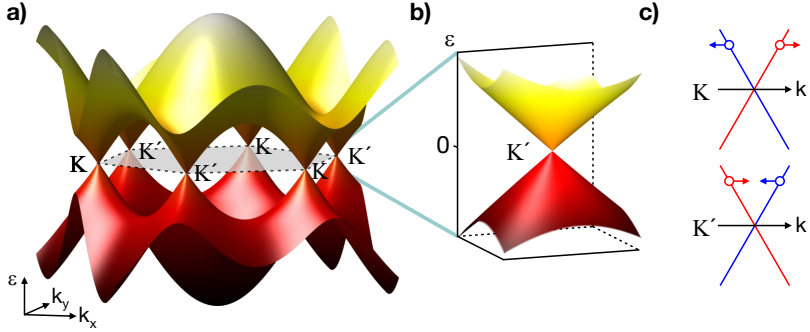


Figure 2.2.: The band structure of single layer graphene. **a)** The energy dispersion in the Brillouin zone. The conduction (upper) band touches the valence (lower) band in six points, the K points. At energies above $t \approx 0.4$ eV the six cones around the K points merge to one. **b)** The bands in the vicinity of \mathbf{K} are called Dirac cones due to their shape. They are linear and have no gap. **c)** The sublattice pseudospin at \mathbf{K} and \mathbf{K}' . The two linear branches (red and blue) have opposite sublattice spins, indicated by the arrows. Additionally, the sublattice pseudospin is inverted when going from \mathbf{K} to \mathbf{K}' .

This dispersion can also be reached by solving the massless 2D Dirac equation [11]. The implications of this are that the electrons have no rest-mass at the K-points and zero energy. Further, the band structure is linear for \mathbf{k} around \mathbf{K} . The points where the conduction and valence band touch are also called Dirac points and the band structure close to these points is called Dirac cone, fig. 2.2 b), due to its shape. In a real sample, the Fermi distribution is broadened by temperature, disorder, chemical doping, etc. It is therefore more appropriate to talk of a charge neutrality region, where the same, low, density of electrons and holes is present, typically leading to a minimum in the measured conductance of the graphene device. In accordance with the majority of publications, we will refer to this region as the charge neutrality point (CNP). The touching of the bands at the Dirac point denotes that graphene is a zero-gap semiconductor (or a half-metal) and can be seamlessly tuned from electrons to hole-like charge carriers by a gate voltage. A rough estimate of the gate induced charge carrier density, n , by the gate voltage V_{gate} can be calculated by considering the excess charge generated by the electrical field of the gate:

$$n = C_{gate}(V_{gate} - V_O)/e. \quad (2.10)$$

Here, C_{gate} is the capacitance per area of the gate and V_O is an offset voltage

which accounts for finding a chemical doping induced shift. Furthermore, the Fermi velocity, v_F , is independent of the energy which is not the case in an ordinary 2D semiconductor and it is very large with $v_F \approx c/300$, where c is the speed of light in vacuum.

Returning to eq. 2.8, the eigenvectors can be calculated

$$(c_1, c_2) = \frac{1}{\sqrt{2}} (e^{-i\theta/2}, \pm e^{i\theta/2}), \quad (2.11)$$

where $\theta = \arctan(k_y/k_x)$. This can be expressed using Pauli matrices and can be understood as a pseudospin. Since the coefficients c_1 and c_2 give the probability of finding the wavefunction in sublattice A or B , this spin is called sublattice pseudospin. A second set of Pauli matrices can be related to the K-points and is called the valley pseudospin.

The property of the sublattice pseudospin is that it decouples the two branches of the dispersion, as shown in fig. 2.2 c), and is therefore called chirality. For smooth disorder (not for lattice defects) it suppresses backscattering. When a charge carrier is backscattered e.g. its momentum changes from k to $-k$, it has to invert its sublattice pseudospin. But since the sublattice pseudospin is a conserved quantity the scattering process is forbidden.

When the next nearest neighbour hopping t' is included in the calculations, eq. 2.6 becomes

$$E_{\pm}(\mathbf{k}) = \pm t \sqrt{1 + f(\mathbf{k})} - t'(f(\mathbf{k}) - 2). \quad (2.12)$$

The second term is the so-called trigonal warping, which breaks the electron-hole symmetry and shifts the energy of the Dirac points [11].

The density of states, which gives the number of available electronic states per energy and space, in single layer graphene is unusual for a 2D system with an energy dependence of

$$D(E) = \frac{4E}{2\pi(\hbar v_F)^2}, \quad (2.13)$$

where the factor of four accounts for the spin and valley degeneracy [12].

Several intriguing new phenomena arise from the mass-less Dirac fermions that constitute the charge carriers in single layer graphene. An examples is Klein tunnelling [13, 14], where electrons can tunnel through a p-n junction under certain angles with transmissions of $T = 1$. This is possible because the charge carrier can change from electron-like in the p-region to hole-like in the n-region. A second example is the Zitterbewegung [15], a manifestation of the Heisenberg uncertainty principle.

2.1.2. Bilayer Graphene

Bilayer graphene is a system where two graphene sheets are stacked upon each other. Two different stacking are found: A-A and Bernal stacking A-B [16]. In A-A stacking the atoms of the upper layer are sitting directly above the atoms of the lower layer. It has been observed in epitaxial graphene [17] and can be considered as two parallel single layer graphene sheets [18]. In contrast, the A-B

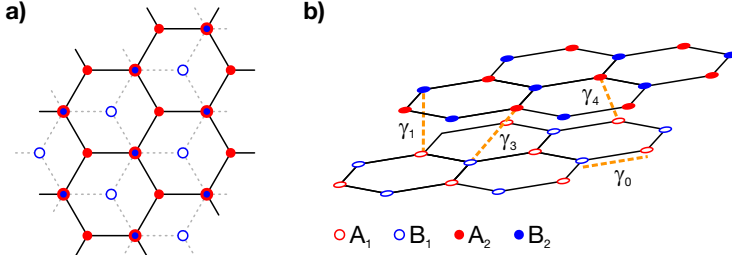


Figure 2.3.: The bilayer graphene lattice in Bernal stacking. **a)** Top view. Atoms B_1 of the lower layer and A_2 of the upper layer have no atom above or underneath them. In contrast, A_1 and B_2 sit directly on top of each other. **b)** Side view with the hopping parameters γ_0 ($A - B$), γ_1 ($A_1 - B_2$), γ_3 ($B_1 - A_2$) and γ_4 ($A_1 - A_2, B_1 - B_2$).

stacking which is shown in fig. 2.3 must be seen as a single 2D system [12] since interlayer hopping couples the two layers.

The most relevant hopping terms are shown in fig. 2.3 b). For intralayer hopping between A_1 (A_2) and B_1 (B_2) in the lower (upper) layer is $\gamma_0 = t$. Three coupling constants are used to describe the hopping between the layer: $\gamma_1 \approx 0.4$ eV connects A_1 and the B_2 directly on top of each other. B_1 and A_2 , which have no atom above or below, are linked via the skew scattering $\gamma_3 \approx 0.3$ eV². Hopping within the same valley spin is determined by the much smaller $\gamma_4 \approx 0.04$ eV [19].

The band structure of bilayer graphene can be calculated with the tight binding approximation [20–22].

When only γ_0 and γ_1 are included in the calculation, an energy dispersion for the valence (–) and conduction (+) is found:

$$E_{\pm}^{\alpha}(\mathbf{k}) = \pm \left[V^2 + \hbar^2 v_F^2 \mathbf{k}^2 + \frac{\gamma_1^2}{2} + (-1)^{\alpha} \sqrt{4V^2 \hbar^2 v_F^2 \mathbf{k}^2 + \gamma_0^2 \hbar^2 v_F^2 \mathbf{k}^2 + \frac{\gamma_1^4}{2}} \right]^{-1/2} \quad (2.14)$$

² γ_2 is not relevant for single or bilayer graphene, as it described next nearest layer hopping [19]

where v_F is the Fermi velocity of single layer graphene, $\alpha = 0(1)$ gives the high (low) energy band and V is an external potential perpendicular to the graphene sheet that opens a gap in the band structure. In a neutral bilayer graphene device, $V = 0$ can be expected.

Eq. 2.14 can be simplified [12] for $V = 0$:

$$E_{\pm}^{\alpha}(\mathbf{k}) = (-1)^{\alpha} \cdot \frac{\gamma_1}{2} \pm \frac{\gamma_1}{2} \sqrt{1 + \left(\mathbf{k} \cdot \frac{3\gamma_0 \mathbf{a}}{\gamma_1} \right)^2} \quad (2.15)$$

For $k \ll \gamma_1/(3\gamma_0 a)$, the bands are parabolic, whereas for $k \gg \gamma_1/(3\gamma_0 a)$ they are linear. Fig. 2.4 a) shows the band structure of bilayer graphene calculated in [23]. The band touch at the \mathbf{K} point at zero energy. A zoom close to \mathbf{K} is shown in fig. 2.4 b). As demonstrated above, the bands are indeed parabolic at small energies and become linear at higher energies. The cross-over between parabolic and linear was estimated to happen at carrier densities of $n \approx 5 \cdot 10^{12} \text{ cm}^{-2}$ [12].

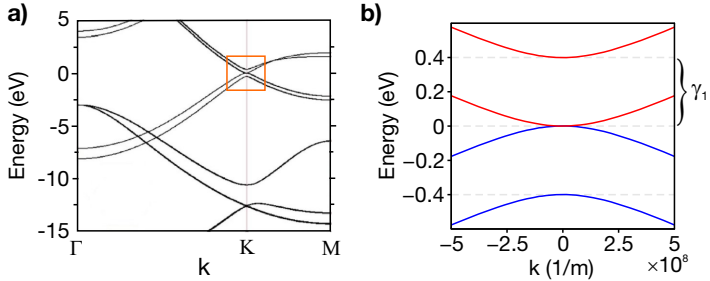


Figure 2.4.: The band structure of neutral bilayer graphene. **a)** Full band structure, adapted from [23]. The bands touch at zero energy in the K points. **b)** The bands close to the K points. Bilayer graphene is a zero-gap semiconductor with a parabolic dispersion a low energy. At higher energy, the bands become linear. The second bands are shifted in energy by $\gamma_1 = 0.4$ eV.

In contrast to single layer graphene, the electrons in bilayer graphene are massive with a small effective mass of $m^* = (0.03 - 0.05)m_e$ [12], where m_e is the electron mass, similar to the mass in GaAs systems ($m_{GaAs}^* \approx 0.067m_e$).

Despite of the non-Dirac-like dispersion the sublattice pseudospin is present in bilayer graphene and additionally the layer index can be considered a spin degree of freedom [12]. In theoretical literature, the valley spin is often mixed with the layer degree of freedom by placing the K valleys in the top layer and the K' valleys

in the bottom one [12, 20]. These additional symmetries will be important for the quantum Hall effect in bilayer graphene.

Similar to single layer graphene, the inclusion of more hopping terms, i.e. γ_3 , leads to trigonal warping. Whereas the single layer band structure lost its electron-hole symmetry, the effect in bilayer graphene is more intriguing. The trigonal warping deforms the parabolic bands at the K points and splits them into four mini-cones, one at **K** and three close by [20, 24]. Further more, the bands are no longer parabolic at these mini-cones, but they are linear [24].

Like in other semiconducting 2DEG systems, the density of states, is constant in bilayer graphene [12]:

$$D(E) = \frac{4m^*}{2\pi\hbar^2} = \text{const}, \quad (2.16)$$

where m^* is the aforementioned effective mass and the factor of four accounts for the spin and valley degeneracy. Another important differentiation to single layer graphene, which has a density $D(E) \propto E$.

2.2. Electron-Electron Interaction in Graphene

At very low densities of the charge carrier concentration the Coulomb interaction between the electrons (e-e interaction) can no longer be neglected. As the carrier densities are reduced, the distance between charge carriers, d , increases. Yet whereas the Coulomb potential drops as $1/d$, the kinetic energy of the electrons decreases as $1/d^2$, eventually leading to a dominance of the Coulomb energy. This interaction can lead to various effects, one is for example the exchange interaction, where the electrostatic force and the Pauli principle cause an alignment of the magnetic spins of the electrons [25].

A measure of the strength of the e-e interaction is the Wigner-Seitz radius, r_s . It gives the ratio of the average Coulomb interaction energy and the Fermi energy [12]. Since the density of states for single layer and bilayer graphene differs they have different r_s [12]:

$$\text{Single layer: } r_s = \frac{e^2}{\epsilon_r \hbar v_F}, \quad \text{Bilayer: } r_s = \frac{2m^* e^2}{\epsilon_r \hbar^2 \sqrt{\pi n}} \quad (2.17)$$

where ϵ_r is the relative permittivity of the environment of the graphene, e. g. silicon oxide, and n is the charge carrier density. Therefore, the smaller ϵ_r and n can become, the larger r_s and hence the e-e interaction becomes.

Entering the values for v_F and \hbar , r_s only depends on ϵ_r for single layer graphene and can thus vary between $0 \leq r_s \lesssim 2.2$ for $\infty \geq \epsilon_r \geq 1$.

For bilayer graphene, setting $\tilde{n} = n/10^{10} \text{ cm}^{-2}$ yields

$$r_s \approx 68.5 \frac{1}{\epsilon_r \sqrt{\tilde{n}}}. \quad (2.18)$$

Thus, suspending the sample in vacuum ($\epsilon_r = 1$) increases the interaction and additionally, suspended samples are usually cleaner and reach lower n_{min} [26]. Hence, e-e interaction can be very large in suspended bilayer graphene devices, possibly larger than in GaAs systems [12].

UNIVERSAL CONDUCTANCE FLUCTUATIONS

Universal conductance fluctuations (UCF) were first observed at low temperature in disordered metallic systems in which the mean free path l is smaller than the sample length L , whereas the phase coherence length is $L_\phi \gtrsim L$. These fluctuations are found to be universally $\sim e^2/h$, independent of the sample shape or its degree of disorder [27–30]. This phenomenon is surprising, as one would expect that the fluctuations self-average in non-microscopic samples. Furthermore, UCF might look random, yet they are in fact reproducible.

This chapter introduces the basic properties of universal conductance fluctuations (UCF) and discusses how these fluctuations are expected to behave in graphene. We start by giving a short summary of electron transport in the Drude picture to define some of the important length scales.

In the Drude picture, the electrons are assumed to be free and only interact with the nuclei of the conductor via scattering [25]. The time between scattering events is $\tau = m/(\rho n e^2)$, where m is the electron mass, ρ the resistivity and n the charge carrier density. The average distance that the electron travels between these scattering events is the mean free path $l = v_F \tau$. How often the electrons are scattered depends on the size of the conductor, L , compared to the mean free path. If the electrons scatter often when travelling through the system, the transport is diffusive and Ohm's law describes the conductivity. However, when the electrons scatter only a few times or not at all, the system is ballistic and can be understood in the Landauer-Büttiker formalism [31] with conductance channels.

Another important length scale is given by the phase coherence length L_ϕ , which stems from the wave-like nature of the electrons. By interacting with the conductor, the phase of the electronic wave function changes by e.g. inelastic scattering off impurities. The length, after which different trajectories have gathered a random phase relative to each other is called phase coherence length L_ϕ .

In a diffusive mesoscopic system, the electrons are scattered by impurities many times if $L \gg l$. Thus, if the conductance is larger than e^2/h , there are many

electron trajectories that can interfere with each other. Given that the electrons can travel through the whole system without losing their phase, $L_\phi \geq L$, these interferences will not average out or result in weak (anti-) localisation, but vary with e^2/h with the impurity configuration [27–29].

In theoretical studies, the conductance fluctuations δg are defined as

$$\delta g = \sqrt{\langle \delta g^2 \rangle} = \sqrt{\langle (g - \langle g \rangle)^2 \rangle} \quad (3.1)$$

where $\langle \rangle$ denotes the ensemble average, i.e. the average over all possible impurity configurations and g the conductance of the system.

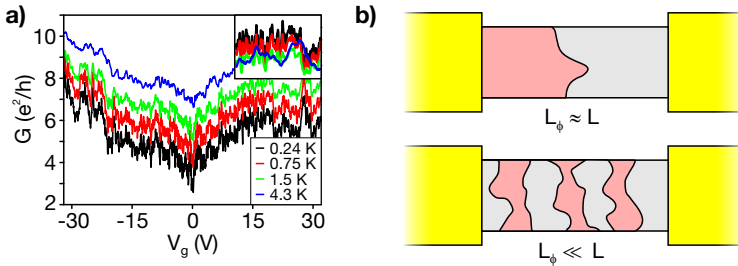


Figure 3.1.: **a)** Exemplary measurement in a short single layer graphene device. The conductance fluctuations are reproducible and are reduced at higher temperatures (G shifted for clarity). The inset shows a non-shifted zoom. **b)** Effect of the phase breaking length L_ϕ . In the upper graph, the conductor is contacted by two electrodes (yellow) and L_ϕ is of the order of the conductor's length L . The CF should reach $\sim e^2/h$. In the lower part, $L_\phi \ll L$ and the conductor decays into individually fluctuating regions, symbolised by the different shading. Now, the CF through the whole device average out and the CF will be suppressed.

This would mean that one has to measure a great many samples to extract δg . Luckily, however, the same fluctuations can be achieved in a single device by either applying a magnetic field B or tuning the Fermi energy via a back-gate [30]. The effect of the magnetic field is to change the phases that the electrons acquire on their trajectories and thus the change the interference patterns. Similarly, changing the back-gate voltage changes the potential landscape and can be viewed as a new disorder configuration.

The theoretical treatment is done in a Landauer-Büttiker picture, where the electrodes are assumed to be ideal channels and the disordered metal is described

as a scattering matrix [29]. Datta showed [32] in a simple argument that by only considering the reflection part of the scattering matrix a δg of order e^2/h can be found, independent of the microscopic details such as sample dimension or disorder strength. More rigorous methods were shown in [27–30].

When going to a finite temperature T , the fluctuations start to be reduced as T is increased. An exemplary measurement is shown in fig. 3.1 a). Increasing T from 0.24 K to 4.3 K reduces the fluctuations in the data visibly. A new length scale becomes important, the thermal length $L_T = \sqrt{\hbar D/k_B T}$ where D is the diffusion coefficient. However, no rapid change in δg is predicted, but a decay of $\delta g \propto T^{-1/2}$ in 2D [30].

When the phase coherence length is shorter than the sample length, the system falls into several independently fluctuating segments, as shown in fig. 3.1 b). The CF will be suppressed since the CF in each segment will average over the whole device [32]. Thus, for $L_\phi < L$, the device is a series of N fluctuators which have a conductance of g_0 and each one fluctuates with δg_0 . A single segment fluctuates with

$$\delta R_0 = \delta (g_0^{-1}) = \frac{\delta g_0}{g_0^2} \quad (3.2)$$

and for a sample of $R = N \cdot R_0$, the measured CF δg are

$$\delta g = \frac{\delta g_0}{N^{3/2}}. \quad (3.3)$$

Hence, the CF decrease quickly once that the phase coherence length is smaller than the sample size.

Disordered single layer graphene differs from a diffusive metal in its chiral charge carriers and the presence of the valley pseudospin. Numerical studies showed UCF of more than e^2/h [33–36] and a strong dependence on the actual impurity concentration [33, 34]. Tworzydło *et al.* predict that strong disorder produces UCF of $\sim e^2/h$ which increase when the disorder is reduced, and at very low disorder the graphene becomes a ballistic conductor and the UCF diminish to zero [34].

SUPERCONDUCTIVITY AND ANDREEV REFLECTION

In this chapter an introduction to superconductivity and the closely related Andreev reflection will be given.

Contacting graphene by superconducting electrodes offers the opportunity to study the transport of Cooper pairs and relativistic electrons and holes [14]. Due to the proximity effect, the graphene near the superconductor can become superconducting itself [37]. Furthermore, exotic phenomena such as specular Andreev reflection [14] could lead to new applications such as a Cooper pair splitter [38].

The processes at the interface between a superconductor and graphene can on the other hand give insight into the transport mechanisms in graphene devices.

4.1. Superconductivity

In 1911, Kammerlingh Onnes and his co-workers observed that the resistance of Mercury dropped to 0Ω below 4.3 K. The scattering of electrons with phonons limits the conductivity at higher temperatures. Yet in most metals the resistivity does not go to zero when reducing T , but saturates due to scattering at crystal defects at a finite value.

The vanishing of the electrical resistivity below a material-characteristic temperature, T_c , was successfully explained by Bardeen, Cooper and Schrieffer's (BCS) theory [39]. Based on previous works, they predicted a condensation of two electrons into a bosonic state, mediated by phonon coupling. In a more intuitive picture [40], an electron travels through the lattice of the superconductor and thereby attracts positively charged nuclei. Such dynamic distortions of the lattice are phonons. In turn, a following electron will still see this positive charge and

be attracted by it. This attractive force can be strong enough to overcompensate for the Coulomb repulsion and then the two electrons condense into a so-called Cooper pair. The electrons forming a Cooper pair must be of opposite momentum k and $-k$ so that the Cooper pair has zero momentum relative to the Fermi sea. Further, the Cooper pair state which has the lowest energy [40] is the singlet state where the electrons have opposite spin, \uparrow and \downarrow . Thus the Cooper pair has spin $s = 0$ and is a bosonic quasi-particle, meaning it does not obey Fermi statistics and can form a many-body ground state.

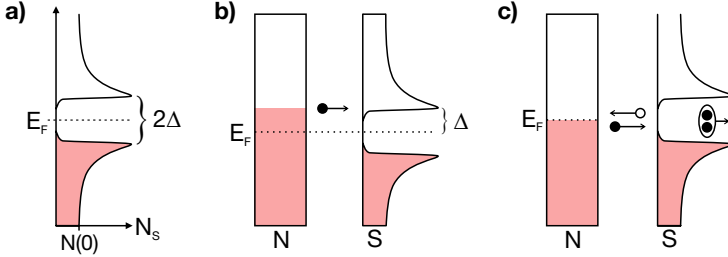


Figure 4.1.: **a)** Density of states for the quasi-particles, N_s , as a function of energy. Far away from the Fermi energy E_F , the density corresponds to density of quasi-particles in absence of a gap, $N(0)$. At Δ above or below E_F the density diverges and goes to zero around E_F . **b)** When a bias $V_{sd} > \Delta/e$ is applied, an electron from N can directly enter S via a quasi-particle state and relax into a Cooper pair. **c)** For $V_{sd} < \Delta/e$, no states are available and the only transport mechanism is Andreev reflection. An electron (filled circle) from N takes another electron with opposite spin and momentum from N to condensate into a Cooper pair. In turn, a hole (empty circle) is retro-reflected to conserve spin, charge and momentum.

In the density of states of the quasi-particles a prominent energy gap, Δ , opens around the Fermi energy. This energy Δ is needed to excite a hole-like (electron-like) quasi-particle and is material dependent. For smaller energies only Cooper pairs are allowed. Since the total number of states is conserved, all the quasi-particle states that would fall into the gap are lifted up by Δ [40]:

$$\frac{N_s(E)}{N(0)} = \begin{cases} \frac{E}{(E^2 - \Delta^2)^{1/2}} & (E > \Delta) \\ 0 & (E < \Delta) \end{cases} \quad (4.1)$$

Here, $N(0)$ is the density of states in the normal conducting state and E the energy relative to E_F . Thus, the density diverges around Δ . Broadening of the

states, e.g. by temperature or disorder, smooths the divergence and leads to a density of states as illustrated in fig. 4.1 a).

When the temperature is raised, a rapid transition from the superconducting state into the normal state occurs at a characteristic temperature T_c . Furthermore, the size of the superconducting gap Δ is reduced at finite temperatures. Close to the T_c , the gap goes as [40]

$$\Delta(T) \approx 1.74 \cdot \Delta_0 \left(1 - \frac{T}{T_c}\right)^{1/2}, \quad (4.2)$$

where $\Delta_0 = 1.764 \cdot k_B T_c$ denotes the gap at zero temperature.

In the presence of an external magnetic field, a superconductor acts as an ideal diamagnet. On one hand, a slowly applied magnetic field is completely expelled from the superconductor. On the other hand, even in the presence of a magnetic field, cooling the superconductor below T_c leads to displacement of the magnetic field, which is the Meissner effect [41].

The application of a magnetic field H_c large enough to overcome Δ leads to breaking of the Cooper pairs and hence normal conduction.

4.2. Andreev Reflection at the Superconductor-Graphene Interface

In this thesis, normal conducting graphene (G) is contacted with superconducting electrodes (S). Hence, the electrons travel through two GS interfaces and the measured conductance G will include the properties of these interfaces. Therefore, it is important to understand the physics taking place at the GS interface. In the following, the processes at an interface between a generic normal metal N and a superconductor will be explained.

In the simplest case, shown in fig. 4.1 b), a bias voltage V_{sd} greater than Δ/e is applied. In that case, an electron incident from N will have enough energy to enter a hole-like state in the superconductor. There it will eventually merge with the Cooper pair condensate [40] and contribute a charge of e to the measured current.

For $V_{sd} < \Delta/e$, there are no quasi-particle states available (eq. 4.1). A direct entrance of an electron from N into S is consequently not possible, as it lacks a second electron to form a Cooper pair. However, if for example an electron with \mathbf{k} and spin \uparrow tries to enter the superconductor, it can join with an electron from N with $-\mathbf{k}$ and spin \downarrow . In order to conserve spin, charge and momentum, a hole state with $-\mathbf{k}$ and spin \downarrow has to travel on the time-reversed trajectory of the missing electron. This process is named Andreev reflection [42], and transfers a charge of $2e$ per occurrence, increasing the conductance in the gap twice compared to

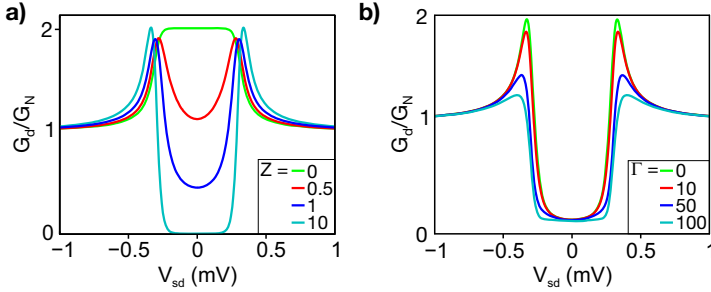


Figure 4.2.: Simulations of the differential conductance G_d in units of normal conductance G_N . The BTK-model was used with $T = 230$ mK and a gap of $\Delta = 300 \mu\text{eV}$. **a)** Varying the barrier strength Z . For small values of Z , Andreev reflection enhances G_d maximally, whereas with increasing Z , G_d decreases for $V_{sd} < \Delta/e$. Very large Z indicate a tunnelling barrier, which completely sub-gap transport. **b)** Varying the broadening Γ suppresses the peak in G_d near Δ/e .

outside of the superconducting gap. Andreev reflection is the only charge transfer possible at a NS interface for energies below the superconducting gap.

Whether the Andreev reflection can double G compared to the normal state, or if all transport in the gap is suppressed depends on the nature of the interface between N and S . The BTK-model, introduced by Blonder, Tinkham and Klapwijk, accounts for a barrier of arbitrary strength Z at the interface [43]. The model can be used to calculate the differential conductance $G_d = \frac{dI}{dV}$ through the NS interface from a metallic junction ($Z = 0$) up to a tunnelling junction ($Z \gg 1$). Above, a perfect transmission of the quasi-particles was assumed ($Z = 0$). Increasing the barrier strength leads to a finite reflection probability of the quasi-particle at the barrier, and reduces the transmission to $t = 1/(1 + Z^2)$. Consequently, the enhancement of the conductance below Δ can be turned into a complete suppression by increasing the barrier strength, as shown in fig. 4.2 a).

The BTK-model only considers the barrier strength and temperature as parameters. However, based on [44] an additional broadening in the density of states around Δ is introduced by a broadening energy Γ . The origin of this broadening can be attributed to inelastic scattering of the quasi-particles at the barrier. The BTK-model then takes the form [43, 45]:

$$I_{NS} = C \int_{-\infty}^{+\infty} [f(E - eV) - f(E)][1 + A(E, \Gamma) - B(E, \Gamma)] dE, \quad (4.3)$$

where f are the Fermi distribution functions which bring in the T -dependence,

and $A(E, \Gamma)$ is the probability of an Andreev reflection and $B(E, \Gamma)$ gives the probability of an ordinary reflection. The pre-factor C includes the resistance of the normal metal and the barrier strength [45]. Fig. 4.2 b) shows an example of the simulated G_d over a NS interface, when only Γ is changed. However, increasing the temperature can yield a similar effect as increasing Γ and therefore one should be careful to quantitatively compare Γ in different measurements.

To return to the conductance fluctuations treated in the previous chapter, the presence of Andreev reflection at the NS interface changes the expected UCF values compared to the normal state conductance fluctuations. Intuitively, one can expect that the transfer of $2e$ per reflection should also lead to a doubling of the fluctuations at the interface. And indeed, Beenakker finds $\langle G_{NS} \rangle \approx 4.3 \langle G_N \rangle$ for a wire geometry [46] and thus $\delta G_{NS} \approx 2 \cdot \delta G_N$. Numerical simulations [47] for a 2D geometry of several different widths and lengths found an enhancement by Andreev reflection of slightly less than two.

By studying the enhancement of the UCF by Andreev reflection in graphene one can gain insight into the transport processes, even in a non-ideal device (effects of finite temperature and barriers).

QUANTUM HALL EFFECT IN GRAPHENE

In this chapter, we give a brief introduction to the classical Hall effect, before we treat the quantum Hall effect. The conductance quantisation and the edge-state picture are presented as well as the impact of the device geometry on the measured quantities. Further, we summarise the expected conductance quantisation in single layer and bilayer graphene and possible mechanisms that can break the symmetry in these systems.

5.1. Hall Effect

The Hall effect was discovered in 1879 by E.H. Hall [48], when he investigated the current through a thin gold foil in a magnetic field. He found a voltage, V_H , which was perpendicular to both the magnetic field and the current direction.

An intuitive explanation for this observation is that the charge carriers in the gold foil are deflected by the Lorentz force, and therefore accumulate on the sample edges. Once the charge carrier accumulation creates an electric field strong enough to compensate the Lorentz force, a steady state is reached and the voltage V_H can be measured.

In a two-dimensional system, the current I flows along the X-axis and the magnetic flux density B is applied perpendicular to the sample plane. The charge carriers are hence deflected in Y-direction and $V_{xy} = V_{Hall}$ can be measured in Y as well. The schematics of such a measurement set-up, called Hall bar, are shown in fig. 5.1 a).

In order to calculate the conductivity tensor σ and the resistivity tensor ρ , the following equation of motion must be evaluated:

$$m\dot{\mathbf{v}} = -e\mathbf{v} \times \mathbf{B} - e\mathbf{E} - \frac{m}{\tau}\mathbf{v}, \quad (5.1)$$

where \mathbf{E} is the electric field, m the mass of the charge carrier and τ the inelastic scattering time in the Drude model [25]. In the steady state, $\dot{\mathbf{v}} = 0$, one finds the tensors

$$\rho = \frac{1}{\sigma_0} \begin{pmatrix} 1 & \omega_c \tau \\ -\omega_c \tau & 1 \end{pmatrix}, \quad \sigma = \sigma_0 \begin{pmatrix} \frac{1}{1+\omega_c^2 \tau^2} & -\frac{\omega_c \tau}{1+\omega_c^2 \tau^2} \\ \frac{\omega_c \tau}{1+\omega_c^2 \tau^2} & \frac{1}{1+\omega_c^2 \tau^2} \end{pmatrix} \quad (5.2)$$

where $\omega_c = eB/m$ is the cyclotron frequency and $\sigma_0 = n\tau e^2/m$ is the conductivity at $B = 0$. The diagonal elements in the above tensors correspond to the transport in the direction of the current (longitudinal), ρ_{xx} and σ_{xx} , and can be measured by V_{xx} . The off-diagonal elements are the (transversal) Hall resistivity ρ_{xy} and conductivity σ_{xy} and relate to V_{xy} . Hence, the longitudinal resistivity remains constant as B is increased, whereas the transversal ρ_{xy} linearly increases.

In the case of a 2D system, the Hall resistance of the macroscopic sample is equivalent to the resistivity, $R_{xy} = \rho_{xy}$. Thus, the measured Hall resistance or conductance is independent of the actual sample sizes which is one of the key properties that make the later on discussed integer quantum Hall effect a very precise measure.

The conversion between the resistivity and conductivity can be written as a tensor inversion and yields

$$\sigma_{xx} = \frac{\rho_{xx}}{\rho_{xx}^2 + \rho_{xy}^2}, \quad \sigma_{xy} = \frac{\rho_{xy}}{\rho_{xx}^2 + \rho_{xy}^2}. \quad (5.3)$$

These relations are valid in the classical Hall effect, but bear some special insight into σ_{xx} in the integer quantum Hall effect, as explained in the following.

5.2. Integer Quantum Hall Effect

In 1980 von Klitzing *et al.* observed in a high mobility silicon 2D electron gas (2DEG) that R_{xy} was not linear but had plateaus at resistance values of $\frac{h}{e^2} \frac{1}{\nu}$ with $\nu = 1, 2, 3, \dots$. At each plateau in R_{xy} , the longitudinal resistance dropped to $R_{xx} = 0$.

In order to understand this observation, it is helpful to look at the motion of the electrons in a semi-classical picture. The electrons are confined into a 2D system, i.e. they can move freely in XY but Z is forbidden. In the presence of a perpendicular magnetic flux density B , in the following simply called magnetic field, the electron trajectories are deflected. If the magnetic field is strong enough, the electrons will be forced on an orbital motion. Treating these orbits quantum mechanically gives an energy dispersion of $\epsilon_N = \hbar\omega_c(N + 1/2)$ with N being an integer. The energy levels for different N are called Landau levels (LL).

When examining the degeneracy of these LL, the ratio of electrons per flux quantum gives

$$\frac{\# \text{ charge carriers}}{\# \text{ flux quanta}} = \frac{n}{eB/h} = \nu \quad (5.4)$$

where ν is also called the filling factor and is, as indicated above, proportional to the quantised conductance.

An intuitive picture of the electrical transport is shown in fig. 5.1 b). In a LL, all electrons are moving along closed orbits and therefore the bulk material does not allow electrons to flow and is insulating. However, on the boundaries of the sample, the electrons cannot complete a revolution without bouncing off the edge. But scattering far away from the edge would require a large energy to overcome the Lorentz force. Consequently, the electrons bounce along the edge and transport charge along the X-axis. The potential difference V_{xy} is proportional to the number of edge states. Each edge state opens a conductance channel, which gives $\sigma_{xy} = \nu \cdot d e^2/h$, where d is the degeneracy of the channel (spin, valley, etc).

The suppression of scattering at the sample edges leads to the peculiar situation, that no voltage drops between contacts 2 and 3 in fig. 5.1 a), and thus, $\rho_{xx} = 0$. However, from eq. 5.3 it becomes clear that in the case of $\rho_{xx} \rightarrow 0$ the corresponding conductivity does not diverge, but also $\sigma_{xx} \rightarrow 0$. The edge states are very robust to elastic or inelastic scattering [31] which makes the transport properties independent of the sample shape or impurity and defect configurations.

An alternative view on the existence of edge states is sketched in fig. 5.1 c). The sample-vacuum boundaries can be modelled as a potential step which deforms the LL energies. If they are bent upwards, some levels can cross the Fermi energy and hence are available for transport. The number of the Landau levels crossing E_F gives the number of current carrying edge states.

Naively, it could be expected from eq. 5.4 that σ_{xy} only lies at a quantised value if the carrier density and the magnetic field are exactly fulfilling eq. 5.4. Experimentally, however, broad plateaus are found in σ_{xy} , which rather sharply transit from one to the next quantised conductance value. Given the situation that exactly N levels are fully occupied and the transport happens via the edge states which are extended over the whole sample. By either increasing the carrier density n or lowering B , the next Landau level $N + 1$ slowly gets populated. In a sample with impurities, the electrostatic potential landscape is deformed with valleys and peaks. Thus the electrons will first start to fill the valleys (and holes the peaks). The electrons will move along the edges of these valleys and as long as the valleys are only partially filled, these trajectories are closed loops in the bulk (localised states) and will not be measured by the contacts. Yet further filling the LL will extend the loops until some can bridge the upper and lower sample edges and electrons can scatter via these states from one edge to the other, where the

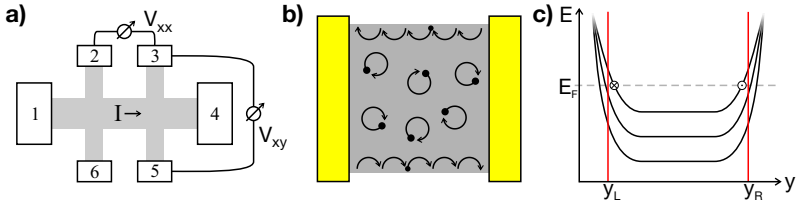


Figure 5.1.: **a)** A Hall bar measurement set-up. The current is driven from contact 1 to 4. The Hall voltage is measured between 3 and 5 or 2 and 6. The longitudinal voltage drop is either measured between 2 and 3 or 5 and 6. **b)** Electron trajectories in the semi-classical picture. The electrons (filled circles) in the bulk are moving on closed orbits and do not contribute to the charge transport. On the sample boundary, the electrons skip along the edges. **c)** Energy of the Landau levels along the Y-axis of the sample. At the sample boundaries (y_L and y_R) the branches are bent upwards due to the transition into the vacuum bands. Some bands can thereby cross the Fermi energy E_F and carry an edge state current.

electron will travel in the opposite direction. This back-scattering to the injecting contact gives rise to a finite ρ_{xx} and σ_{xx} .

Measurement Configurations

The scattering-free transport along the sample edges has important implications for how the injecting and detecting contacts influence the measurements. Three common geometries with different numbers of contacts are shown in fig. 5.2 and will be discussed in the following.

The configuration which allows measuring almost the ideal longitudinal and transversal voltages is shown in fig. 5.2 a). Given the case that the current is injected in contact 1 with the chemical potential μ_L and flows to 4. The contacts 2 and 3 will then sense V_{xx} . Since the edge states are scatter-free, there is no voltage drop from 2 to 3 ($\rho_{xx} = 0$ and $\sigma_{xx} = 0$) and no dissipation in the contacts. When the electrons enter contact 4, the chemical potential has to change from μ_L to μ_R . The difference $\Delta\mu$ dissipates at contact 4 and can locally heat the sample (hot spot) [49]. Simultaneously, the Hall voltage V_{xy} can be measured, e.g. from 3 to 4. Again, the contacts act as pure voltage probes and the lead resistance or interface from the electrodes to the sample does not enter the measured voltage (four-terminal set-up). All high precision measurements of the Hall resistance are performed in Hall bar configuration.

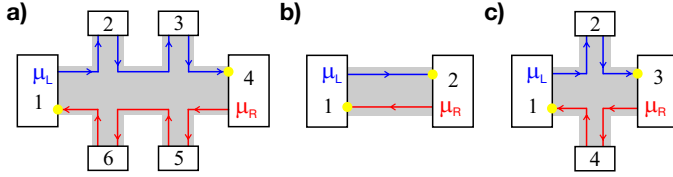


Figure 5.2.: The different geometries for measurement of the Hall effect: **a)** Hall bar for four-terminal measurements. **b)** Two-terminal set-up. **c)** Hall cross. The yellow spot marks where the dissipation of the chemical potential difference $\Delta\mu$ between source and drain contacts occurs.

The other extreme is the two-terminal configuration of fig. 5.2 b). Here, the electrons are driven from contact 1 to 2 and either the voltage drop over the sample or the current through the whole sample is measured. In contrast to the situation above, the measurement inadvertently includes the resistance of the wires and the interfaces. Furthermore, a mix of ρ_{xx} and ρ_{xy} is measured. The exact ratio of ρ_{xx} and ρ_{xy} can be calculated [50, 51] and depends on the ratio of the sample width and length W/L . In the case of $W = L$, one actually measures the Hall conductivity through the sample (all current flows in the edge states). Therefore the two-terminal conductance will be quantised, but can be shifted to higher R due to the series resistances of the leads and the interface. If $W \neq L$, the ρ_{xx} will be picked up as well, giving either dips or peaks between the plateaus [50, 51].

The energy dissipation $\Delta\mu$ from the ballistic edge states to the contacts will influence the measured data.

A third set-up is shown in fig. 5.2 b), the Hall cross geometry [49]. Here, the electrons are injected in contact 1 and extracted in 3. Consequently, the dissipation occurs at these two contacts. The Hall voltage can be measured in a four-terminal set-up across contacts 2 and 4. However, if one wants to measure ρ_{xx} , the situation is as in the two-terminal case. Otherwise, the current could be injected from 1 to 4 and V_{xx} measured from 2 to 3 (not shown). Yet, is it not possible to measure both ρ_{xx} and ρ_{xy} simultaneously.

5.3. Quantum Hall Effect in Graphene

Single Layer Graphene

The quantum Hall effect discussed above consisted of Landau levels whose parabolic energy dispersion relies on a mass term. Therefore it is easy to see that the relativistic zero rest-mass electrons in graphene require a different treatment.

5. Quantum Hall Effect in Graphene

Solving the relativistic Dirac equation in the presence of a magnetic field yields the Landau level energies [52] of

$$\epsilon_N = \pm v_F \sqrt{2ehBN}. \quad (5.5)$$

The square root dependence of the LL energy has the outcome that the first levels have a very large spacing compared to the higher levels, as sketched in fig. 5.3 a). This large spacing enables the measurement of the QHE (at least the first plateau) at room temperature [9]. Although magnetic fields of 45 T were needed, single layer graphene is up to date the only system where such a measurement could be successfully conducted.

The Hall conductivity is quantised as

$$\sigma_{xy} = 4\nu \frac{e^2}{h} = 4 \left(N + \frac{1}{2} \right) \frac{e^2}{h} = \pm 2, \pm 6, \pm 10, \dots \frac{e^2}{h} \quad (5.6)$$

The first values ± 2 actually belong to the zero energy LL, which is made up of electrons and holes. Their existence can be motivated by the chiral nature of the charge carriers in single layer graphene (the sublattice pseudospin). When an electron performs a closed orbit, it acquires an additional phase of π , the Berry phase [53], which causes the $+1/2$ term in the equation above.

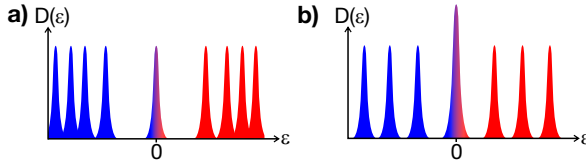


Figure 5.3.: Density of states as a function of the Landau level energy ϵ . **a)** For single layer graphene, the spacing of the LL follows \sqrt{N} . **b)** In bilayer graphene, the spacing is nearly linear. However, the zero energy LL consists of two levels, namely $N = 0$ and $N = 1$.

Another explanation for the unusual sequence of Landau levels involves consideration of the Zeeman effect, which gives the energy shifts of spins parallel or anti-parallel to the applied B . Surprisingly, the pseudospin Zeeman energy is exactly the LL spacing: $g\mu_B B = \hbar\omega_c$ [54, 55], where $g = 2$ is the g-factor and μ_B the Bohr magneton. The Zeeman effect therefore mixes the valley pseudospin states of the N th LL with the pseudospins of the $N + 1$ th LL. The zero energy LL thereby splits-up and loses its valley pseudospin degeneracy, giving $\sigma_{xy} = \pm 2 e^2/h$ [54]. In higher LL the full degeneracy is re-established (spin and valley) and thus steps of $4 e^2/h$ can be observed.

Furthermore, the evolution of the LL with magnetic field is not linear, as in the integer quantum Hall effect, but goes with \sqrt{B} [10].

Bilayer Graphene

Like in a semiconductor 2DEG, the electrons in bilayer graphene are massive and the Landau level spacing is regular, as shown in fig. 5.1. However, the actual energy of the LL is [20]

$$\epsilon_N = \pm \hbar \omega_c \sqrt{N(N-1)} \quad (5.7)$$

As a result, the LL of $N = 0$ and $N = 1$ both lie at zero energy. In addition to the spin and valley degeneracy this signifies an eightfold degeneracy of the zero energy state and thus a large density of states, as shown in fig. 5.1. As in single layer graphene, this state is made up of electrons and holes alike. Away from the zero energy LL, the degeneracy returns to fourfold and the steps in the conductivity are thus $4 e^2/h$ in all LL except for the step from $-4 e^2/h$ to $+4 e^2/h$ which is caused by the zero energy LL. The sequence of conductance plateaus is

$$\sigma_{xy} = \pm 4, \pm 8, \pm 12, \dots \frac{e^2}{h} \quad (5.8)$$

The Berry phase due to the sublattice pseudospin is 2π , twice the phase of single layer graphene.

Similar to semiconductor 2DEGs, the dispersion of the LL in magnetic field is proportional to B for $N \gg 1$.

Symmetry Breaking

The rich number of symmetries in bilayer graphene (and to some extent in single layer graphene as well), allows for many broken-symmetry states. These states are characterised by the appearance of additional conductance steps.

The Zeeman energy is an obvious candidate to lift the spin degeneracy. However, as shown above, it does not give new states but mixes LL in single layer graphene. In bilayer graphene, the Zeeman effect can cause the appearance of steps of $2 e^2/h$ [56].

Further lifting can be induced or at least mediated by electron-electron interactions. More specifically, the exchange interaction of the electrons can generate a quantum Hall ferromagnet (QHF) [10, 12, 56, 57] and magnetic catalysis (MC) [10, 55, 56]. In MC, the electron-electron interaction is supposed to induce a spontaneous mass in the charge carriers at the $N = 0$ LL. It therefore lifts the degeneracy only between $\nu = -2$ and $\nu = +2$ in single layer graphene or $\nu = -4$ and $\nu = +4$ in bilayers.

The QHF in contrast, lifts the degeneracies in all states. In the highly degenerate LL, the interaction energy can become large enough to align all spins [10].

In bilayer graphene, the eightfold degeneracy of the lowest Landau level and the large interaction parameter favours spontaneous interaction effects. A wealth of possible spontaneous states at zero magnetic field has been predicted. Some

examples being excitonic condensation [58, 59], where the layers are charge polarised, or the quantum anomalous Hall effect [60–62], quantum valley Hall, quantum spin Hall [62] or the layer anti-ferromagnet [62, 63] which all show energy gaps. Furthermore, non-gapped states such as a nematic phase [64] were predicted.

Mechanical strain was suggested [24] as a non-interaction driven mechanism to break the symmetries. Such strain could be introduced if the substrate and the electrodes have much larger thermal contraction than the thermal expansion of the graphene flake when cooling the system to cryogenic temperatures.

DEVICE FABRICATION, CHARACTERISATION AND MEASUREMENT SET-UP

In this chapter the fabrication of the graphene devices will be explained. We start by depositing the graphene onto a silicon substrate. Then the found graphene flakes are characterised by means of atomic force microscopy (AFM) and Raman scattering of laser light. Subsequently, the devices are patterned with electron beam lithography into a resist to shape the flakes in the desired geometry by reactive ion etching. After a second lithography step, metal electrodes are evaporated on the samples. Additionally, the etching of the substrate in hydrofluoric acid (HF) is shown and finally the devices are current annealed in a cryostat. A short description of the cryogenic measurement set-ups used for this thesis is given in the final section.

6.1. Graphene Flake Deposition

This section will treat the necessary steps to achieve a transfer of few-layer graphene flakes onto a silicon substrate with a good yield. The micromechanical cleavage method [53] is used to obtain micrometer-sized flakes of high crystalline quality. Step-by-step instructions and information about the used equipment can be found in appendix A.

We use highly doped silicon wafers with 290-310 nm silicon oxide on top. Since the silicon remains conductive even at cryogenic temperatures, we can use it as a back-gate to apply an electric field to the graphene devices. In a first step, the wafer is cut into pieces of about $1.5 \times 1.5 \text{ cm}^2$. Afterwards, the wafer pieces are cleaned and a coordinate grid is evaporated on them.

The graphene flakes are typically prepared as follows. The starting point is a piece of natural graphite (NGS Naturgraphit GmbH, Germany) which is cleaved

with sticky tape (SPV 224P, Nitto Europe NV). Usually, the graphite piece with the largest flat areas (i.e. shiny) is selected and the flat side is pressed on the sticky tape. When the graphite is peeled off the tape, a large but thin piece remains on the tape. These steps are repeated until an area approximately equal to the wafer piece is mostly covered with graphite flakes. Then the tape is covered with a second, fresh piece of tape.

The wafer pieces are cleaned by reactive ion etching (RIE) and immediately after the wafer pieces are taken out of the etcher, the two tapes are separated and the sticky side with the graphite is pressed on the wafer. If the tape is not applied within a minute of opening the etcher the yield of flakes is reduced, presumably due to formation of a water film on the silicon oxide. Furthermore, gently rubbing the tape with the thumb increases the coverage. The tape is dissolved in acetone, leaving graphene and graphite on the substrate.

Subsequently, the samples are baked on a hotplate to improve the sticking of the graphene to the wafer. After that, a fresh piece of tape is used to peel off the graphite. This step removes the very thick graphite pieces and should only leave freshly cleaved graphene flakes on the substrate, which probably were never in contact with the tape's glue.

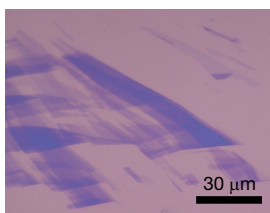


Figure 6.1.: Optical image of graphene flake deposited without solvent-use. Typically, the flakes are narrow and long with thicker graphite near them. The scale bar is 30 μm long.

Alternatively, a piece of adhesive tape is completely covered with a continuous film of low-grade highly ordered pyrolytic graphite (HOPG). The small grain sizes in low-grade HOPG facilitate the tearing of the graphite and thus more graphene will come off the graphite film and stay on the substrate. The cleaning procedure of the wafer remains the same, but after the RIE step the HOPG-covered side of the tape is pressed onto the wafer and gently rubbed. Then it is slowly peeled off, leaving graphene and graphite on the wafer. As no solvents are used and the deposited graphene was not in contact with the tape, the flakes are extremely clean. However, they tend to be rather narrow and tattered (fig. 6.1). Frequently the flakes are close to large pieces of graphite, which makes further processing more difficult.

We store the samples in a desiccator under vacuum to avoid contamination of the graphene. If kept in air, the flakes cannot be electrically contacted after some weeks.

6.2. Optical Characterisation

As our typical graphene flakes are of the order of tens of μm , we need a very fast method to locate suitable flakes on our cm^2 sized silicon wafers.

On a silicon substrate with 290-310 nm SiO_2 on top, the optical contrast in white light is still high enough to distinguish single layer graphene flakes [65].

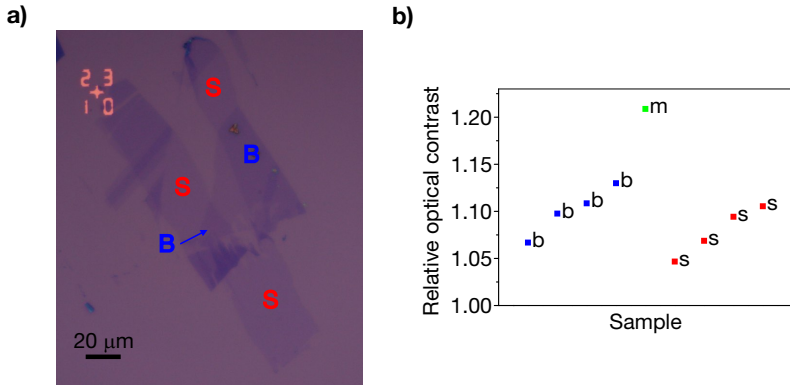


Figure 6.2: a) Optical image of single layer graphene (S) and bilayer graphene (B) on a silicon oxide substrate. A marker of the coordinate grid can be seen in the top left corner. The magnification was $500\times$ and scale bar corresponds to $20\ \mu\text{m}$. b) The relative optical contrast in the red-channel of the digital image for different graphene flakes on the same wafer piece. The difference between single (s) and bilayer (b) graphene is small, whereas a multilayer flake (m) can be easily distinguished.

With an optical microscope we can scan a wafer piece in less than an hour, while locating thin flakes of less than $2\ \mu\text{m}$ dimension is still possible. When a suitable flake is found, pictures of the flake are taken in different magnifications ($1000\times$, $500\times$ and $100\times$) with a microscope-mounted Canon EOS 500D camera for further processing. The optical contrast between the graphene flake and the substrate serves as a first rough selection criterion. Since the SiO_2 thickness

of our wafers varies, we assign the flake with the lowest contrast to single layer graphene.

An image of single and bilayer graphene flakes is shown in fig. 6.2 a). Generally, the small contrast of non-adjacent single and bilayer graphene is hard to distinguish due to inhomogeneities in the SiO₂ thickness and the post-processing of the camera. Fig. 6.2 b) illustrates these problems, where the optical contrast is given as the ratio of the substrate over the graphene in the red channel of the digital image. Thick multilayers (> 3 layers) can be easily identified, whereas single and bilayer graphene exhibit a very similar contrast.

6.3. Raman Spectroscopy

Raman spectroscopy offers a fast, reliable and non-destructive method to identify the number of layers in 1-3 layer graphene [66, 67]. We use an alpha300 R confocal Raman imaging system (WITec GmbH, Germany) with a Nd:YAG laser.

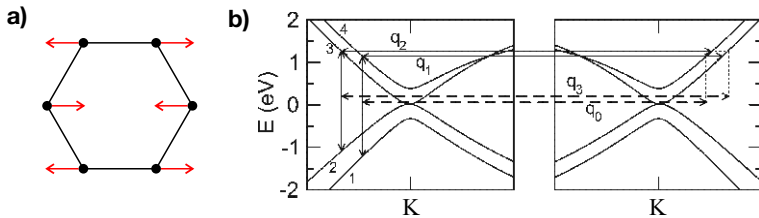


Figure 6.3.: a) The in-plane vibrations of the sp^2 bonds, which are responsible for the G-peak. b) The possible transitions for the 2D-peak. The photon excites the transition of electrons from the valence to the conduction band near the K points. Via coupling to phonons they relax and emit a photon. Adapted from [67].

At the heart of Raman spectroscopy lies Stokes scattering of monochromatic light [68]. A laser emits the light (in our set-up 523 nm wavelength) which is focused on the sample surface, and the back-scattered light is collected and analysed in a spectrometer. The light can lead to three different types of scattered light: Elastic scattering (Rayleigh scattering), where no energy is exchanged, Stokes scattering, where a molecule is excited and a red-shifted photon gets emitted, and anti-Stokes scattering, where an excited state absorbs a photon and relaxes into the ground state and thus the emitted photon is blue-shifted.

In the case of graphene, there are two dominant peaks in the Raman spectrum, the G- and the 2D-peak. An exemplary Raman spectrum of single, bi- and

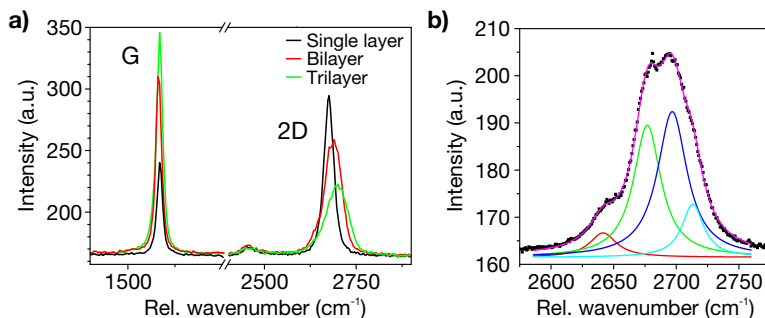


Figure 6.4.: Raman spectra of graphene on SiO₂, taken with a green laser (532 nm). **a)** Comparison of single layer (black), bilayer (red) and trilayer (green) graphene. The intensity of the *G*-peak increases from single to trilayer graphene. On the other hand, the *2D*-peak is reduced in intensity. Furthermore, its shape changes from one Lorentz peak for single layer to four peaks in bilayer and two in trilayer. **b)** The *2D*-peak of a bilayer graphene flake. It can be well fitted by four Lorentzians.

trilayer graphene on the same wafer piece is shown in figure 6.4 a). The peak at $\sim 1580 \text{ cm}^{-1}$ is the so-called *G*-peak. It originates from the in-plane vibrations of the sp^2 bonds [66, 69], as schematically shown in fig. 6.3 a). Since the number of sp^2 bonds in the laser spot is proportional to the number of layers, a rough proportionality of the integrated *G*-peak to the graphene layers can be found [67]. Different focussing and wafer-to-wafer variations make this method rather unreliable.

However, a more trustworthy feature to distinguish the number of layers is the shape of the *2D*-peak at around 2700 cm^{-1} . It is formed by processes in which a photon is absorbed to excite an electron from the valence to the conduction band. From there, the electron relaxes via coupling to phonons and eventually recombines with a hole in the valence band, which emits a photon of less energy than the incident one [66, 67]. In single layer graphene only one relaxation process is possible, which leads to a single Lorentzian shape of the *2D*-peak, as can be seen in fig. 6.4 a). In contrast, bilayer graphene supports four different excitations due to the splitting of the low-energy bands, as shown in fig. 6.3 b), and thus the *2D*-peak is composed of four Lorentzians [66, 67]. A fit of these four components in the bilayer *2D*-peak is displayed in fig. 6.4 b). For more layers, two Lorentzians can be fitted. The position of the *G* and *2D* peaks can be shifted due to doping of the graphene [70] and may generally change in intensity.

The crystal quality of the graphene can be related to the *D*-peak at around 1350 cm^{-1} , which is caused by elastic backscattering [67]. It is prominent on the flake edges, where many dangling bonds can be found [67]. In agreement with [71], our graphene flakes show often a very small *D*-peak even away from the edges, which is attributed to lattice vacancies or bound adatoms. If a more prominent *D*-peak is found, the flake gets rejected.

6.4. Atomic Force Microscopy on Graphene

Atomic force microscopy (AFM) is a non-destructive method to investigate the topography of graphene on silicon. We use the intermittent contact mode (tapping mode) where a cantilever is oscillating above the surface and is only for a very short time in contact with the sample surface. A Dimension 3100 AFM (Veeco, USA) is used in combination with PPP-NCHR cantilevers (Nanosensors, Switzerland).

Although it has been demonstrated that the number of graphene layers can be estimated with AFM [72], we found this method to be prone to errors and very time consuming. For example, a water film on the substrate can add to the apparent thickness of a single layer graphene flake and thus a range of 0.3 nm to 0.9 nm step height from the substrate to the first layer can be observed. There is a considerable overlap with the bilayer case, where steps of 0.5 - 1.1 nm are seen [72]. Instead we focus on quality control of the graphene flakes and processing steps.

Fig. 6.5 a) shows the topography of a clean flake shortly after deposition. Some residue is visible on the SiO_2 substrate (dots) and extend under the flake, as they appear to be smoothed by the overlying graphene. In contrast, the sample in fig. 6.5 b) a processed sample shows residue on the substrate and on the graphene. Hence we optimised our fabrication process to minimise the residue due to the adhesive tape and resists.

6.5. Lithography and Metallisation

In this section the electron beam (e-beam) lithography, flake etching and the metallisation of the sample are introduced. Two different approaches to avoid resist residues on the graphene flake are explained. Detailed recipes can be found in appendix B.

The complete lithography process is depicted in fig. 6.6. In a first step, the e-beam resist is spun on the wafer. A quick bake on a hotplate evaporates the solvent remaining in the resist. Subsequently, the resist is patterned by exposure with a current of electrons. These electrons scatter with the resist molecules and break chemical bonds such that the exposed polymer chains break into smaller pieces [73]. Due to the scattering of the electrons in the resist and substrate, the exposure

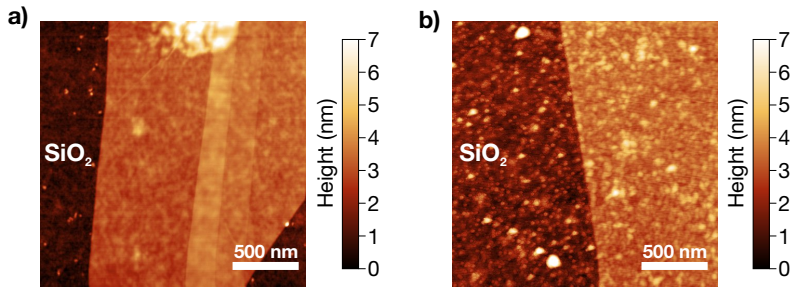


Figure 6.5.: Topographies of two different graphene flakes on SiO₂. Both were taken with an AFM in tapping-mode. **a)** A clean flake before any processing. The flake itself is smooth and shows very little residue. The dark regions are the substrate. **b)** A flake after processing. On both the substrate and the flake residue is conspicuous.

profile widens as the electrons travel further down the resist. Consequently, an undercut can be observed, as shown in fig. 6.6 c).

Since the unexposed and the shorter, exposed polymer chains have different solubility, the exposed resist can be dissolved without affecting the unexposed resist, which is called the development of the resist. A typical device requires two lithography steps: First, an etching mask is written to shape the flake with reactive ion etching. The exposure to a argon/oxygen plasma etches the graphene where it is not covered by the resist film. The specifics are listed in appendix B. In the second step, the mask for the metallic electrodes is written.

For the electrodes a thin metal film is evaporated on the whole surface. A electron gun is used to melt a metallic target and release a flux of metal vapour. The thickness of the resist and the undercut help preventing a continuous film and thus the superfluous metal can be removed by dissolving the remaining resist. In the end a thin metal film stays where the resist was exposed. Usually, the samples are cooled to 0 °C during the evaporation to avoid melting the resist with the heat deposited by the metal vapour.

As graphene is completely exposed to contaminants from either the substrate or solvents and resists, the cleaning steps and surface treatments are essential. Any plasma etching to remove the organic resist would inadvertently damage the graphene as well. On the other hand, any solvent that might be able to remove resist residue will also dissolve the resist mask.

In the following, this issue is addressed and three approaches to deal with it are explained.

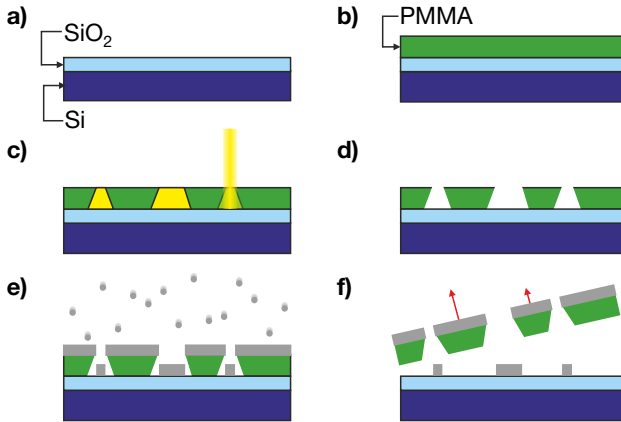


Figure 6.6.: The lithography process: **a)** The wafer with the graphene flakes on top. **b)** The e-beam resist (typically PMMA) is spin-coated. **c)** The resist is then patterned with an electron beam. **d)** Afterwards, the exposed resist is dissolved in a developer. **e)** A metal film is evaporated and sticks on the substrate where the resist was removed. **f)** The superfluous metal is removed by dissolving the remaining resist. The metal stays only on the patterned areas on the sample.

6.5.1. PMMA Mask

A standard resist for e-beam lithography is 950k poly(methyl methacrylate), usually abbreviated as PMMA. We found that after the lithography and the development with a solution of isopropanol and 4-Methylpentan-2-one (MIBK) there was still a considerable amount of residue left on the graphene. Therefore, the finished devices showed a high resistance originating from the PMMA left under the metal electrodes. Increasing the contact area mitigated the problem by increasing the probability of pinholes in the residue layer, but is not always possible due to the device geometry. Development in warm developer only slightly improved the contacts and in turn led to poor control of the development process (a very narrow time-window between over- and under-development).

Consequently, we turned to the following methods to minimise the residue layer under the electrodes.

6.5.2. PMMA/MA Mask

The use of a PMMA/MA layer underneath the 950k PMMA reduces the contact resistance significantly. PMMA/MA is a copolymer with a higher solubility than pure PMMA and a much higher sensitivity to e-beam. Hence the dose that passes through the PMMA layer is more than enough to expose the PMMA/MA. A large undercut is the result. AFM measurements show that there is less residue on the sample than with the PMMA layer. Furthermore, the large undercut facilitates the lift-off.

Conversely, the large undercut proves problematic when an etching mask is written, as the graphene is in some parts only protected by a free-standing PMMA layer which slows etching but does not prevent it. Thus damaged graphene fringes the etched strip. This can be avoided by using only a PMMA layer for the etching mask and the PMMA/MA for the electrodes. But then the graphene is again in contact with poorly soluble PMMA molecules and has to be cleaned thoroughly in acetone and isopropanol.

Additionally, the undercut of ~ 300 nm limits the resolution of the lithography and makes devices with features of $1\ \mu\text{m}$ spacing a challenge.

6.5.3. Aluminium Oxide Sacrificial Layer

A way to combine the high resolution and easy handling of a single PMMA layer with the low residue of a PMMA/MA-PMMA bilayer resist is the use of aluminium oxide, Al_2O_3 , as a sacrificial layer ¹.

After the flake localisation and characterisation in Raman spectroscopy, a thin film of 3 nm aluminium is evaporated on the wafer and left to oxidise in the air. For the lithography, a PMMA layer is spin-coated. Following the development of the resist, the whole wafer is dipped into a tetramethylammonium hydroxide (TMAH) solution to etch the Al_2O_3 layer. This etch does not affect the PMMA and shows no under-etching in optical microscopy. Any PMMA residue in the exposed area is removed with the Al_2O_3 and clean graphene is revealed. We can then plasma-etch the exposed graphene, whereas the rest of the flake is protected both by PMMA and Al_2O_3 , or evaporate metal on the graphene.

When the lift-off is done, a further dip in TMAH removes the Al_2O_3 on the rest of the wafer to avoid electrical short-circuits by unoxidised aluminium. Furthermore, neither an Al_2O_3 film or PMMA residue remains on the graphene flake and spoils the electrical properties. The contact resistance of our devices at least as good as with the PMMA/MA layer.

We further checked with Raman spectroscopy whether the TMAH treatment damages the graphene or if aluminium stays on the flakes. Fig. 6.7 summarises our findings. Optically, fig. 6.7 a) and b), the coverage of the graphene increases

¹T. Palacios, Talk at Graphene Week 2011, Obergurgl

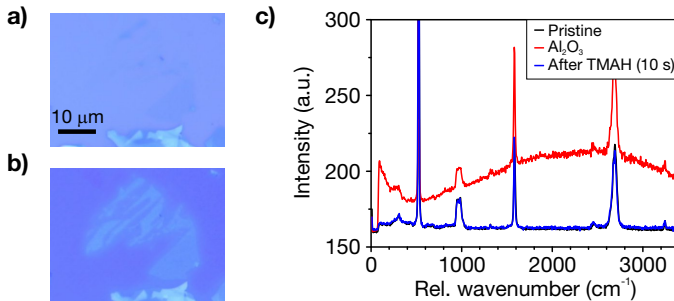


Figure 6.7.: Influence of the Al_2O_3 and TMAH on a bilayer graphene flake. a) Optical image of the graphene flake before aluminium deposition, the scale bar corresponds to $10\ \mu\text{m}$. b) The same flake covered by Al_2O_3 . The optical contrast is much increased. c) Raman spectra of the flake before processing (black), covered with Al_2O_3 (red) and after TMAH etching (blue). The Al_2O_3 gives a strong fluorescent back-ground, but no additional peaks. The spectra for the untreated graphene and after TMAH etching collapse. The intensities were normalised to compensate for focusing.

the visible contrast and changes the colour of the flake and the substrate. After TMAH etching, the optical image returns to the pristine situation.

In the Raman spectrum, fig. 6.7 c), the Al_2O_3 gives a broad fluorescent background without any additional peaks. The spectra of the bilayer graphene in pristine condition and after the TMAH treatment collapse and show identical peak positions and relative peak heights. The data was normalised, as the intensity strongly depends on the laser focus and thus is never exactly the same after moving of the sample.

TMAH is known to etch SiO_2 , but at such a slow rate compared to aluminium [74] that we did not observe the loss of graphene due to under-etching.

6.6. Suspending Graphene

The silicon oxide substrate that is commonly used for graphene devices introduces some draw-backs, such as trapped charges [75] that give rise to disorder in the graphene, or a dielectric constant of about 3.9, which reduces the e-e interaction. Therefore, it can be advantageous to remove the oxide and suspend the graphene. This section introduces etching with hydrofluoric acid (HF) which follows Bolotin *et al.* [26]. The specifics can be found in appendix B.

Owing to the aggressiveness of HF only very few metals are suitable to contact the graphene. A thin adhesive layer of 1.5 nm chromium is covered by 70 nm gold. Since gold is inert to HF, it can be used as a simple etching mask, protecting the SiO₂ underneath.

In order to ensure the cleanliness of our samples before the etch, they are annealed in a vacuum chamber at 200 °C and $<10^{-6}$ mbar for several hours.

The etching process itself is isotropic, meaning that it etches as far down as to the side. Thus the geometry of the electrodes is limited by the depth of SiO₂ that is etched. However, the silicon oxide under the graphene flake is etched like uncovered oxide [26]. If less than 100 nm SiO₂ is removed, the graphene is likely to collapse on the substrate, probably due to electrostatic and capillary forces. Contrarily, etching most of the SiO₂ away under-etches the contacts and make them mechanically unstable. Such a partially collapsed electrode is shown in

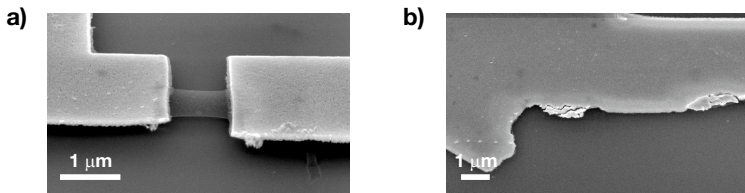


Figure 6.8.: **a)** SEM micrograph of a finished suspended graphene device. The dark graphene flake bridges the two bright electrodes. The scale bar corresponds to 1 μm . **b)** Example of a partially collapsed electrode. The gold electrode (upper half) collapsed at two points and comes close to the substrate (lower half).

fig. 6.8 b). Frequently, these devices have leaks between the electrodes and the back-gate. We see this behaviour if less than 100 nm of SiO₂ remains and attribute it to the low dielectric strength of the thin oxide and the collapsed contacts or some graphene flakes which touch the substrate.

Therefore, we conclude that etching about 160 nm of SiO₂ and leaving 140 nm on the wafer is the optimum for our devices.

After the HF-etch, the sample is transferred to ethanol which acts as a transfer fluid for critical point drying (CPD). In CPD, the transfer fluid is gradually replaced by liquid CO₂. Then the sample chamber is heated to the critical point where the phase boundary between liquid and gaseous ceases to exist. When pressure is released the CO₂ is in the gas phase and the graphene was not exposed to capillary forces.

In the last step, the wafer piece is glued into a chip carrier and an electrical connection between chip carriers and the electrodes on the wafer is made with a bonder (aluminium wire, ultrasonic bonding).

6.7. Current Annealing

After mounting the samples in a cryostat the SiO₂ supported devices are ready to be measured. In the case of suspended graphene devices however, current annealing is necessary to see any graphene-like behaviour. It is likely that this can be attributed to the inefficient back-gate. The removal of half of the oxide reduces the gate efficiency to about 40% of the 300 nm oxide gate and we are limiting the gate range to ± 5 V to avoid the collapse of the suspended graphene due to electrostatic forces. Hence, even a few impurities on the flake would shift the CNP out of the gate range.

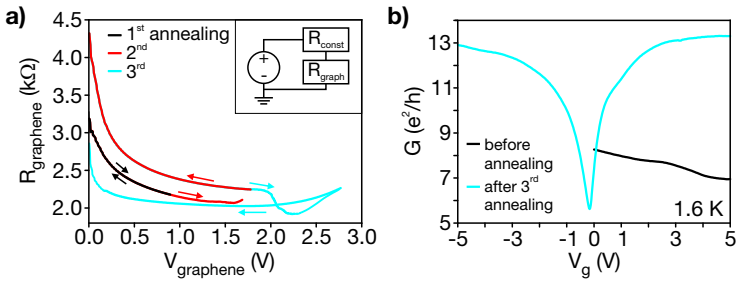


Figure 6.9.: The current annealing process for a suspended bilayer graphene device at 1.6 K in a helium atmosphere. **a)** The applied DC voltage, V_{graphene} , and the resistance of the graphene and the contacts, R_{graphene} , are plotted. In the first annealing step, no change in R_{graphene} occurred. In the second step, the resistance increased at 1.75 V. Yet no CNP could be observed. The third annealing yielded a drop in resistance, but a CNP was recovered. The inset shows the used electrical circuit. **b)** The conductance G of the device as a function of the gate voltage V_g . Before annealing, the gate response was weak and the slope suggested a CNP a larger positive V_g . After the third annealing, a CNP could be observed close to $V_g = 0$ V.

We use a simple electrical set-up to perform a controlled current annealing of the graphene flake between two contacts. A voltage source (Yokogawa 7651 DC Source, Yokogawa Electric Corporation, Japan) is connected to a constant resistor of 10 $k\Omega$ and one contact of the sample is connected in series, the other is set to ground (insert of fig. 6.9 a)). The additional series resistor ensures that the current through the flake is limited even if the graphene becomes very conductive. A Keithley 2000 voltmeter (Keithley Instruments Inc., USA) is used to measure the voltage drop over the series resistor and the resistance of the

graphene is calculated. The temperature is typically around 1.5 K, but rises during the annealing process. During the procedure, the sample is kept either in a cryogenic vacuum or in a helium atmosphere. We could not observe a particular dependence of the annealing process on the temperature, as it worked up to 20 K in Helium atmosphere.

After the initial cool-down, the graphene device is tested for gate response. Representative curves of the conductance G as function of the gate voltage V_g for suspended bilayer graphene are shown in fig. 6.9 b). No CNP can be observed and the conductance decrease suggests that it is shifted to $V_g > 5$ V (black curve). In the first annealing step, fig. 6.9 a) black curve, one volt bias dropped over the sample. The lack of a hysteresis when ramping down the bias is indicative of an unsuccessful annealing. Consequently, the voltage is increased further in the second step, until a change in resistance showed at 1.7 V (red curve). Ramping the voltage down led to a hysteresis, but no visible CNP in the gate response. Increasing the voltage further showed another kink in the resistance and a hysteresis (blue curve). Now, a pronounced CNP near zero V_g can be observed (fig. 6.9 b), blue curve).

Generally, we could not identify a signature of a successful current annealing in the $V_{graphene}$ vs $R_{graphene}$ plots. Quite often, a kink in the response did not lead to the appearance of a CNP. Sometimes, the resistance increases in a successful annealing, sometimes it decreases, depending on how close the CNP comes to zero gate voltage.

However, the necessary current density, given as current over width of the graphene, was found to be $0.4 \text{ mA}/\mu\text{m} - 0.5 \text{ mA}/\mu\text{m}$ for bilayer graphene and $0.5 \text{ mA}/\mu\text{m} - 0.9 \text{ mA}/\mu\text{m}$ for single layer graphene.

6.8. Measurement Set-up

Two cryostats were used to acquire the data shown in this thesis. One was a ^4He system, which is capable of cooling the samples down to 1.5 K and varying the temperature with a heater up to room temperature. A reservoir of liquid ^4He is connected through a capillary with the sample chamber. This chamber can be pumped to low pressure. The pressure difference between the sample chamber and the ^4He reservoir pushes the helium into the chamber where it evaporates. The helium flow can be adjusted by a needle valve. Further, the low pressure lowers the boiling point of the helium to about 1.4 K.

The second type of cryostat was a ^3He system, as shown in fig. 6.10 a). In such a system, a so-called 1K-pot is cooled by evaporating helium at low pressure, like in the ^4He system. However, the 1K-pot is used to cool a separate, closed ^3He reservoir. The ^3He isotope is very rare in nature and has an even lower boiling point than the ^4He isotope. The sample is thermally connected to the ^3He

circulation via a cold finger. After the ^3He has condensed, a charcoal piece, the sorb, acts as a pump by absorbing all gaseous ^3He . Thereby, the temperature can be lowered to about 230 mK in our system. After all ^3He has evaporated, the sorb can be heated to 35 K to release all ^3He , which then condenses in the 1K-pot again.

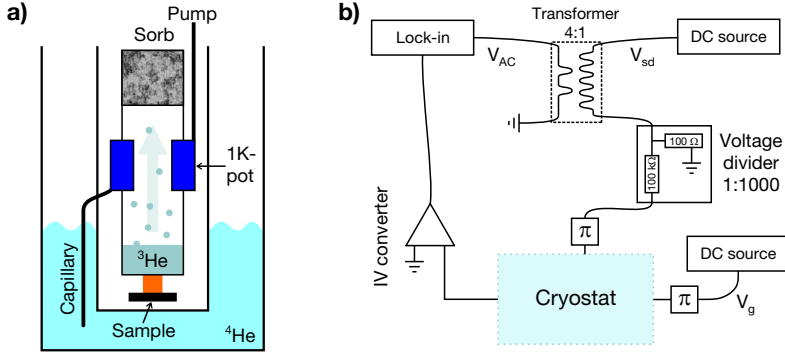


Figure 6.10.: **a)** Schematic of a ^3He refrigerator. The gaseous ^3He is cooled by the 1K-pot until it condenses. A sorb absorbs the evaporating ^3He and thereby the remaining liquid is cooled to about 230 mK. The sample is thermally coupled to the ^3He reservoir. **b)** A schematic of a typical electrical set-up.

All electrical measurements, as shown in fig. 6.10 b), were done with lock-in amplifiers of type SR830 (Stanford Research Systems, USA). The lock-in amplifier can apply a small AC voltage, V_{AC} , of an adjustable frequency (here typically 10-77.77 Hz). This V_{AC} is then superimposed onto a DC voltage, V_{sd} , via a transformer. A voltage divider of 1:1000 reduces the voltage, which is fed through π -filters (LC filters) into the electrical lines of the cryostat. The voltage drops over the sample and drives a current which is converted into a voltage and amplified by an IV-converter (in-house built) as close to the cryostat as possible. Typical amplifications are 10^5 - 10^6 V/A. The resulting voltage is then measured with the lock-in amplifier. The DC voltages are either applied with a Yokogawa 7651 or with the auxiliary output of the lock-in amplifier. We chose $eV_{AC} < k_B T$ whenever possible.

CONDUCTANCE FLUCTUATIONS IN GRAPHENE WITH SUPERCONDUCTING CONTACTS

In this chapter graphene devices that are contacted with superconducting electrodes and rest on SiO_2 substrate are investigated. More specifically, we look into the enhancement of the conductance fluctuations (CF) by Andreev reflection. We compare the extracted values for the CF at different gate voltages V_g and study the CF when the electrodes are in a superconducting state and in the case of suppression of the superconductivity by a small magnetic field.

Superconducting electrodes can provide additional information on the transport mechanisms in disordered systems [46]. The phase sensitive Andreev reflection can occur at the interface between the superconductor (S) and the normal conducting graphene (G). At energies below the superconducting gap Δ electrons from G can only enter S in the form of a Cooper pair, as explained in chapter 4.

Graphene has proven to be interesting for the study of conductance fluctuations in disordered systems [76–83]. In common supported graphene devices disorder is inevitably introduced by the substrate and CF have been shown to be major corrections to the transport at low temperature.

The CF have been studied by means of numerical calculations [33, 84] and were predicted to show a dependence on the gate voltage. At the charge neutrality point (CNP) or very close to it, the CF were found to be reduced compared to the values away from the CNP. Furthermore, the CF in graphene were calculated to be larger in graphene than in metallic systems, by a factor of up to four [33, 35]. The inclusion of intervalley scattering or trigonal warping can reduce this enhancement and limit the CF to the metallic values [34, 35].

From an experimental point of view, the CF in graphene are a controversial topic. In recent experiments, the CF were found to either vary with the charge

carrier density n [78, 82, 83] or to be constant over the investigated range of n [85].

The proximity-effect induced supercurrent through graphene devices was studied using various superconducting metals as electrodes [37, 79, 86–88]. For aluminium [37, 86, 87] the measured critical currents, the current where the induced supercurrent breaks down, were lower than expected. The origin of this lowering has not yet been established, but either disorder [14] or the (possibly reduced) superconducting gap Δ [88] were suspected. With view to applications such as a graphene-based SQUID [89] or a Cooper pair splitter [38], a better understanding of the physics of the interplay between graphene and superconductors is required.

7.1. Basic Transport Properties

In order to investigate the effect of the superconducting contacts on the CF in graphene, we studied the sample presented below.

An illustration of a two-terminal graphene device is shown in fig. 7.1 a). The

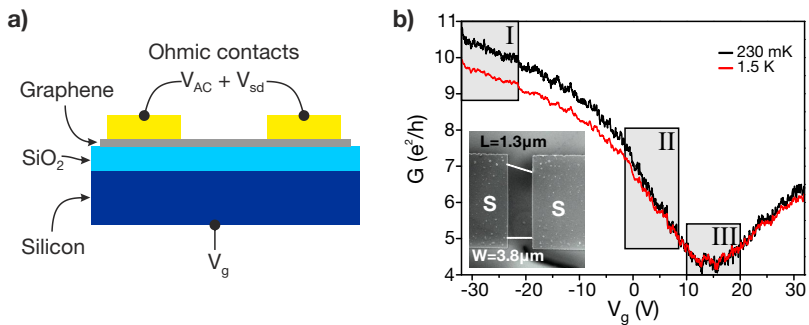


Figure 7.1.: **a)** A schematic of a two-terminal device. The graphene flake is contacted with metallic electrodes, the Ohmic contacts, to which an AC excitation V_{AC} and a DC bias V_{sd} can be applied. The silicon acts as a back-gate when V_g is applied. The SiO_2 isolates the graphene from the gate. **b)** The response of the conductance G through the single layer graphene device on the applied back-gate voltage V_g at 230 mK and 1.5 K (lower curve). The charge neutrality region lies at $V_g = 15$ V. The marked regions (I)-(III) are investigated later on in greater detail. The inset shows a micrograph of the device.

graphene flake lies on top of an insulating SiO_2 layer, and is contacted by metallic

electrodes, acting as Ohmic contacts. These electrodes are used to probe the charge carriers in the graphene by applying an AC excitation V_{AC} and optionally a DC bias voltage V_{sd} . The conductive silicon wafer acts as a back-gate to which the gate voltage V_g is applied.

The actual sample is shown in the inset of fig. 7.1 b) and consists of a single layer graphene (SLG) flake of length $L = 1.3 \mu\text{m}$ and width $W = 3.8 \mu\text{m}$, contacted with aluminium / titanium (50 nm / 5 nm) electrodes. The critical temperature T_c of the electrodes is about 0.9 K, which translates into a gap of $\Delta_{T=0} = 1.764 \cdot k_B T_c \approx 140 \mu\text{eV}$ [40].

The two-terminal conductance G through the whole device as a function of the applied gate voltage V_g is shown in fig. 7.1 b). The minimum in conductance of $G \approx 4 e^2/h$ lies around $V_g = 15 \text{ V}$ and marks the charge neutrality point. At $V_g > 15 \text{ V}$ the charge carriers are electrons, for $V_g < 15 \text{ V}$ the transport occurs via holes. The shift of the CNP in V_g suggests p-doping. Such can be caused by charged impurities, which also introduce disorder and thus scattering [90]. This manifests in the broad shape of the dip in G .

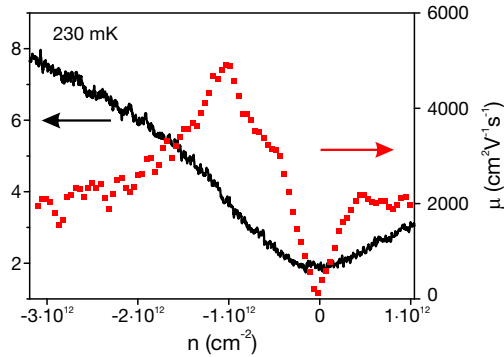


Figure 7.2.: The conductivity σ of the graphene flake as a function of the estimated carrier density n . The scale on the right gives the calculated field effect mobility μ , which is proportional to the slope of σ . At the inflection point at $n = 0$, μ is zero due to the virtually constant σ . The mobility reaches a maximum of $5000 \text{ cm}^2/\text{Vs}$ on the hole side. At higher n the mobility saturates around $2000 \text{ cm}^2/\text{Vs}$.

The conductivity $\sigma = G \cdot L/W$ against the calculated charge carrier density n is plotted in fig. 7.2. We used the capacitor model from eqn. 2.10 to estimate n . From these values the field effect charge carrier mobilities can be estimated,

which is proportional to the slope of σ :

$$\mu = \frac{1}{e} \frac{d\sigma}{dn}. \quad (7.1)$$

We extract an average hole mobility in the vicinity of the CNP of $3500 \text{ cm}^2 \text{ V}^{-1} \text{ s}^{-1}$ at 230 mK and a slightly lower electron mobility, as shown in fig. 7.2. These values are comparable to similar devices in literature. In order to calculate the corresponding diffusion coefficient D we use $D = \mu/e\beta$ [81], where $\beta = 8.3 \text{ eV}$ is a parameter dependent on v_F and the density of states in SLG. We find $D \approx 420 \text{ cm}^2/\text{s}$. From the equation of the diffusion coefficient in a Fermi gas the mean free path can be extracted: $l = 2D/v_F \approx 85 \text{ nm}$. Therefore, $l \ll L$ and the system is diffusive near the CNP. Another important length scale is the thermal length L_T , which evaluates for the presented sample to $L_T \approx 1.2 \text{ } \mu\text{m} \sim L$.

7.2. Enhancement of the CF by Andreev Reflection

First of all, we show that Andreev reflection enhances the conductance fluctuations in our graphene device. The superconductivity-induced features can be identified by suppressing the superconductivity either by applying a bias voltage V_{sd} or a small magnetic field B .

The measured two-terminal conductance G as a function of V_g is shown for temperatures of 230 mK and 1.5 K in fig. 7.1 b). At the lower temperature, the Al contacts are in the superconducting state, while for the higher temperature $T > T_c$ they are in the normal state.

At high doping, i.e. for large negative gate voltages, the conductance G is reduced in the normal state by $\sim 1 \text{ e}^2/h$, while G remains the same near the CNP. This can be explained by the series resistance of the Al leads adding to the device in the normal state. Figure 7.1 b) also shows that the CF are enhanced in the superconducting state. However, since the measurement in this figure was performed with an applied source-drain bias voltage $V_{sd} = 140 \text{ } \mu\text{V}$ which is similar to Δ , the CF are not fully enhanced by Andreev reflection.

We want to focus on three distinct regimes that are highlighted in fig. 7.1: (I) high doping with slow change in G , (II) intermediate doping with steeply changing G and (III) near the CNP. We expect diffusive transport as in disordered metals in regime (I). In contrast, in regime (III) near the CNP, the resistance of the graphene is high and graphene-properties should dominate the transport.

Figure 7.3 displays grey scale plots of G in region (III) near the CNP as a function of V_{sd} and V_g at 230 mK. In fig. 7.3 a), the electrodes are in a superconducting state. Due to the superconducting gap Δ transport is expected to be dominated by Andreev reflection at low bias voltage $V_{sd} < 2\Delta/e$, where the

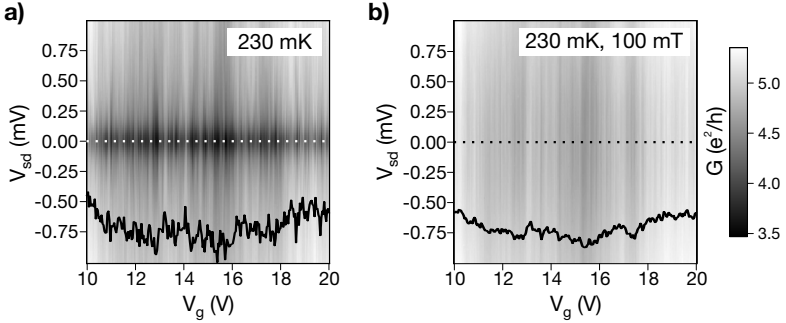


Figure 7.3.: **a)** Grey scale of the conductance G as a function of the gate voltage V_g and the applied source-drain bias V_{sd} at 230 mK in region (III). The system enters the superconducting gap for $|V_{sd}| < 0.3$ V. The conductance fluctuations in the gap region increase, while outside the fluctuations are decreasing with increased $|V_{sd}|$. A cut in the superconducting gap (indicated by the dotted line) is shown by the black curve. **b)** Measurement of G with a 100 mT perpendicular magnetic field applied. The conductance fluctuations are reduced, as can be seen from the cut (black solid curve) at $V_{sd} = 0$ V.

factor 2 accounts for the two superconductors defining source and drain contacts. In this gate window the device displays a suppression of G at small V_{sd} , as can be seen by the dark lower conducting region around $V_{sd} = 0$ in fig. 7.3. The lower G is indicative for weakly coupled contacts with barrier strength Z large enough to partly suppress transport for $V_{sd} \lesssim 2\Delta/e$. The fluctuations in G as a function of V_g are largest at zero bias and are reduced by an increased V_{sd} . When applying a small magnetic field, as shown in figure 7.3 b), the superconductivity is suppressed. Consequently, the fluctuations of G at zero bias are visibly reduced.

Whether the conductance at $V_{sd} = 0$ is enhanced or reduced is strongly dependent on the carrier density. In fig. 7.4 a), the averaged conductance as a function of V_{sd} for the three gate regimes is shown. In (II) and (III) a suppression of G around $V_{sd} = 0$ can be observed. When a magnetic field is applied (dotted lines), no reduction of G with $V_{sd} \rightarrow 0$ can be observed. At a bias of $|V_{sd}| > 0.5$ mV, the curves with and without magnetic field coincide. Unlike the other two regimes, region (I) shows an enhancement of G at low V_{sd} . Furthermore, the application of B lowers G compared to the superconducting case, as is expected when the enhancement is due to Andreev reflection. This indicates that the barrier strength in this sample is gate-dependent, and is lowest in the metallic regime (I) and increases as the CNP is approached in (II)-(III).

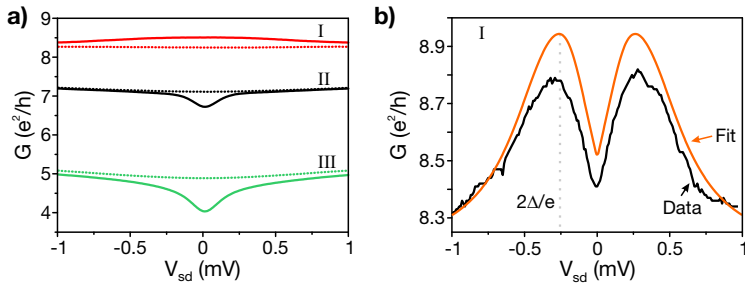


Figure 7.4.: The conductance G as a function of the applied bias V_{sd} at 230 mK. **a)** Averaged curves for the three gate regimes (I)-(III). With superconducting electrodes (solid), a suppression of G around $V_{sd} = 0$ occurs in (II) and (III), whereas (I) shows a small enhancement. With $B = 100$ mT applied (dotted), both the suppression and the enhancement vanish. **b)** Fit of the BTK-model (red) to data measured in regime (I). The features can be reproduced, yet the magnitude of the enhancement is slightly overestimated. A value of $Z \approx 0.48$ and $2\Delta \approx 240 \mu\text{eV}$ are found.

In fig. 7.4 b) an individual curve of region (I) is fitted by the BTK-model, eqn. 4.3. The fit is qualitatively agreeing with the data and can reproduce the features. The positions of the two maxima in G and of the dip in G at $V_{sd} = 0$, caused by the lowered density of states in the gap Δ , are well fitted. The absolute values of G are overestimated by the fitted parameters. However, the small remaining difference can be explained by recalling that the BTK-model implements a normal-superconductor interface, whereas in our data the graphene inevitably is included, although the impact is lowest in (I). We find that $Z \approx 0.48$ and $2\Delta \approx 240 \mu\text{eV}$, which seems reasonable in respect to the above findings.

Closer to the CNP, in regions (II)-(III), the resistance of the graphene dominates the transport and thus used the BTK-model does no longer apply as it neglects the density of states available in the graphene.

In order to quantify the change in the conductance fluctuations originating from enhancement due to Andreev reflections, we evaluate the standard deviation of the conductance,

$$\delta G = \sqrt{\frac{1}{n-1} \sum_{i=1}^n (G_i - \bar{G})^2}, \quad (7.2)$$

where G_i is a single value of the measured conductance and \bar{G} is the average conductance, as a function of the bias voltage V_{sd} , as shown in [81].

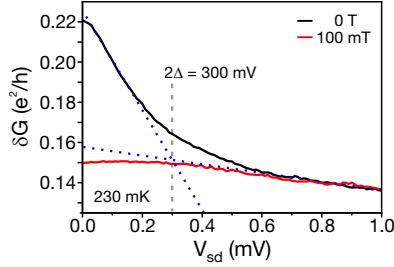


Figure 7.5.: Conductance fluctuations δG as a function of the applied bias voltage V_{sd} at 230 mK in region (III). Two regimes can be observed in the superconducting state (solid line): Outside of the superconducting gap ($V_{sd} > 0.3$ mV), the fluctuations are reduced in comparison to the values in the gap. In 100 mT perpendicular field superconductivity is suppressed (dotted line). At $V_{sd} > 0.6$ mV the normal and superconducting δG are identical. Below $V_{sd} = 0.3$ mV, the superconducting contacts enhance the fluctuations by a factor of up to 1.5 when compared to δG in the normal state at 100 mT.

Figure 7.5 shows a plot of δG against V_{sd} near the CNP in (III). When the electrodes are in a superconducting state, the CF are largest at zero V_{sd} with $\delta G = 0.22 e^2/h$. With increasing V_{sd} the CF decrease and reach at $V_{sd} = 1$ mV a value of $\delta G = 0.14 e^2/h$. By comparing the slopes of the steeply changing CF at small V_{sd} and the more slowly varying CF at larger V_{sd} , we can find a crossover which should correspond to a superconducting gap of $2\Delta \approx 300 \mu V$. In the normal conducting state at 100 mT, the CF are about $0.14 e^2/h$ at $V_{sd} = 1$ mV, which coincides with the value for the superconducting electrodes. However, for $V_{sd} < 0.3$ mV the CF in the normal state saturate at $\delta G = 0.15 e^2/h$. This demonstrates that the CF in the superconducting state are enhanced by a factor of up to 1.5 compared to the normal state.

When comparing the normal state fluctuations $\delta G \approx 0.15 e^2/h$ to the theoretical Altshuler-Lee-Stone (ALS) value of $\delta G = 0.69 \sqrt{W/L} e^2/h \approx 1.2 e^2/h$ [33], we find that the prediction is almost one order of magnitude larger than the measured value. One way to resolve this discrepancy is to assume that the phase coherence length L_ϕ is much shorter than the length L of the device. Assuming that each segment of length L_ϕ is fluctuating independently, yields an overall reduced CF [81]. Applying this approach to the values we found for this device yields a phase coherence length of ~ 300 nm. However, the fact that the measured CF is nearly doubled in the superconducting states suggests that almost all electrons are within the coherence length of one of the superconducting interface, hence $L_\phi \gtrsim L/2$.

This is strong contradicting to the value of L_ϕ estimated from the normal state fluctuations.

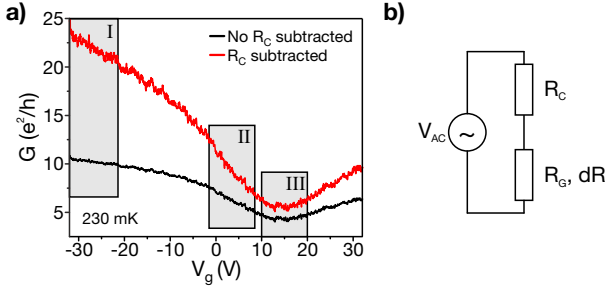


Figure 7.6.: **a)** The conductance G as a function of the gate voltage V_g at 230 mK with and without the subtraction of a constant series resistor R_C . When R_C is not subtracted (black curve) the CF are stronger in region (III) than in region (I). With $R_C = 1.35$ k Ω subtracted the CF are stronger in region (I) and decrease when approaching the CNP in region (III). **b)** Circuit diagram of the device. A constant resistor R_C is in series with the graphene resistor R_G . All fluctuations δR originate in the graphene part.

Another parameter which can reduce the apparent CF is a built-in series resistance R_C . This is schematically shown in 7.6 b). The graphene part has the resistance R_G which fluctuates with δR , whereas R_C is assumed to be constant. In practice R_C consists of the electrical lines in the measurement set-up, the input impedance of the IV converter and the resistance of the Al contact lines. In addition, it may also contain to some extent the contact resistance of the device [51]. All this is intrinsic to two-terminal measurements. We assume that R_C is independent of the carrier concentration in the graphene flake. The subtraction of R_C corrects the measured fluctuations, δG_m , by $\delta G = (1 + R_C/R_G)^2 \cdot \delta G_m$. By adding the known resistance of the measurement setup (measurement lines and IV converter) we arrive at a lower boundary of $R_C \approx 1.35$ k Ω . An upper boundary of $R_C \approx 1.5$ k Ω . can be extracted from the quantum Hall effect, which due to the magnetic field measures the device in the normal state. R_C has been deduced from the shifts of the Hall plateaus.

7.3. Gate-dependence of the UCF

Figure 7.6 a) compares G against V_g at 230 mK with and without $R_C = 1.35 \text{ k}\Omega$ subtracted. As expected the correction results in the largest change at large doping when G is large. The same is true for the CF, as we will show in the following.

In order to assess the sensitivity of the CF on the value of R_C , we have investigated the dependence of the CF measured at $V_{sd} = 0$ and 230 mK for different R_C values, ranging from 0 to 2 k Ω in regime (I) (high doping), (II) (intermediate doping), and (III) (CNP). Figure 7.7 shows the result. In order to calculate δG a B-spline was subtracted to account for the non-constant background of the graphene conductance $G(V_g)$. The absolute values of the CF are lower than the values found in figure 7.5, because there only a linear background was removed.

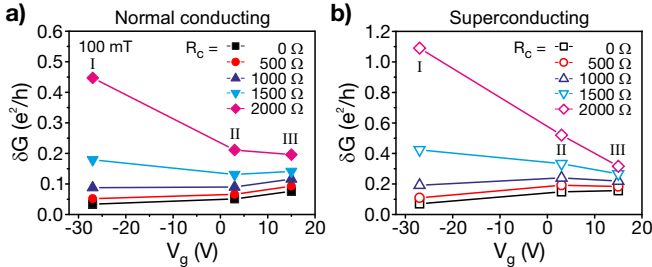


Figure 7.7.: Conductance fluctuations δG at 230 mK and $V_{sd} = 0$ in dependence on the gate V_g and for different values of R_C . A B-spline was subtracted from the original data to account for the changing conductivity of the graphene. **a)** Normal conducting electrodes at 100 mT. The effect of R_C is strongest in region (I). Without the subtraction of R_C , δG increases from (I) to (III). At the largest subtracted $R_C = 2000 \Omega$, δG decreases from (I) to (III). **b)** δG in the superconducting state. The CF are enhanced compared to the normal state. The dependence of the CF on V_g and R_C follows the same tendency as in the normal state.

In figure 7.7 a) the electrical contacts are in a normal conducting state due to the application of a 100 mT magnetic field. The as measured data (no R_C subtracted) shows the smallest CF which increase from $0.03 \text{ e}^2/h$ in (I) to $0.08 \text{ e}^2/h$ in (III). Around the series resistance that we estimated for our set-up ($1.35 \text{ k}\Omega - 1.5 \text{ k}\Omega$), the fluctuations are nearly independent of V_g , with values of $\sim 0.14 \text{ e}^2/h$ in regimes (I) and (III). If $R_C = 2 \text{ k}\Omega$ is subtracted the CF in (I) reach $0.45 \text{ e}^2/h$ and are reduced to $0.2 \text{ e}^2/h$ in (III).

Without the subtraction of R_C , the CF are minimal at large doping and increase near the CNP. When R_C is subtracted the CF increase. However, they increase the most in region (I), less strong in region (II) and the weakest increase is in region (III). This can lead to a reversal of the dependence of the CFs on the V_g .

The conductance fluctuations δG with superconducting contacts are plotted in figure 7.7 b). The measured data without any R_C subtracted shows an increase from $0.07 e^2/h$ in (I) to $0.16 e^2/h$ near the CNP in (III). Again, for values of R_C that lie within the estimates for our set-up, the CF vary only weakly with V_g from $0.32 e^2/h$ in (I) to $0.25 e^2/h$ in (III). At higher values of R_C the CF decrease significantly from (I) to (III).

Evidently, the superconductivity enhances the CF in all three regimes. In (I) and (III) the enhancement lies close to a factor of 2. Yet in regime (II) it appears to be consistently higher and reaches a factor of 3. In part this large enhancement factor originates from the resistance of the aluminium electrodes, which is approximately 100Ω in the normal state in our device. If we consider this difference, we find an enhancement factor of around 1.9 for (I) and (III), but still above 2 for regime (II).

In recent experiments contradicting observations were made. In [83] an increase of the CF near the CNP was seen, where the increase of the CF from high charge carrier concentration to near the CNP was attributed to the formation of electron-hole puddles. In contrast, a decrease of CF near the CNP was found in [78, 82]. The changes in the CF were reported to be of a factor of 3 or larger. Gate independent CF were observed in [85]. As in our device, [83] rely on two-terminal measurements, which include R_C , whereas [78, 82] use a four-terminal set-up, where R_C is irrelevant. As shown above, we can see all three gate dependences if we subtract R_C . Nevertheless, for the range of R_C that we estimate for our set-up, we find nearly no change in CF at high charge carrier density and near the CNP in our graphene device.

7.4. Summary

Using graphene devices with superconducting contacts, we have shown that CFs are enhanced in the superconducting relative to the normal state of the contacts. This enhancement amounts to a factor between 1.4 and 2 and thus suggests that all electrons in the device of length $L = 1.3 \mu\text{m}$ are within the coherence length of one of the two contacts where Andreev reflection occurs which is the origin of the doubling [46]. The phase coherence length at 230 mK is therefore large and amounts to $l_\phi \gtrsim L/2$. We established a constant series resistor R_C to account for our two-terminal measurement set-up and device and investigated its impact on the CF. For values of R_C that we estimated for our set-up and device the CF remain smaller than e^2/h . Furthermore, we investigated the dependence of the CF on the back-gate voltage V_{gate} . A strong dependence on R_C is found. Without

subtraction of R_C the CF increase around the CNP compared to the CF at high doping. In the range of appropriate R_C the CF are nearly independent of V_{gate} .

SUSPENDED TWO-TERMINAL SINGLE LAYER GRAPHENE

In the following chapters the experimental findings on suspended graphene devices will be presented.

The removal of the SiO_2 under the graphene flakes opens a route to investigate high mobility graphene devices. Furthermore, the suspended graphene resides in vacuum and thus in a medium of low relative permittivity ϵ_r which enhances electron-electron interaction. A schematic of a suspended graphene device is shown in the inset of fig. 8.2 a).

We start by presenting suspended two-terminal single layer graphene devices. Due to the high mobility of the devices, the Quantum Hall effect (QHE) can be observed at low magnetic fields. A lifting of the degeneracy in the lowest Landau level (LL) and a transition into an insulating state at $\nu = 0$ can be found in these samples. Further, the $\nu = \pm 2$ state persists down to very low magnetic fields

In the next chapter, our results on suspended bilayer graphene devices are shown. Bilayer graphene differs from single layer graphene in its massive charge carriers and parabolic bandstructure. Most importantly, the eightfold degeneracy of the lowest Landau level and the large interaction parameter r_s give rise to a wealth of possible spontaneous many-body states at zero magnetic field. We present two-terminal measurements of two distinct sample classes. In one type of sample, a Hall state of $\nu = \pm 4$ is found to prevail to very low fields whereas at higher fields, an insulating state forms at $\nu = 0$ and a state at $\nu = \pm 2$ appears.

A second type of bilayer graphene devices shows a full lifting of the lowest LL and thus a sequence of $\pm 3, \pm 2, \pm 1 e^2/h$ and a low conductive phase at the CNP, extending from zero magnetic field to high fields. We study this gapped phase by means of IV-spectroscopy as V_g or B are tuned.

Further, suspended bilayer graphene devices in a Hall-cross geometry are presented. We investigate the homogeneity of the current annealed devices and present the measured Hall signal.

8.1. Quantum Hall Effect and Lifted Degeneracy

Single layer graphene (SLG) on substrate has shown the anomalous integer quantum Hall effect [91] which gives rise to a prominent conductance plateau at $\pm 2 e^2/h$. The large energy gap corresponding to this Landau level has made the observation of the QHE at room temperature possible, albeit at high magnetic fields [9]. At cryogenic temperatures, the application of large fields has led to a lifting of the degeneracy in the lowest Landau levels, resulting in additional plateaus at filling factors of ± 4 and ± 1 [92]. Furthermore, an insulating phase at zero energy has been found and assigned as the $\nu = 0$ state [92–95].

By removing the SiO_2 substrate a major source of disorder can be avoided. Therefore, the charge carrier mobility will be higher than in supported devices [26] and the disorder potential is much reduced. As a consequence, the above features become observable at magnetic fields lower than 4 T. Furthermore, new phases of the quantum Hall effect were predicted to occur in high quality graphene devices [10, 54, 56, 57].

We fabricated the suspended single layer graphene device *S1* with the width $W = 0.7 \mu\text{m}$ and length $L = 1 \mu\text{m}$ as described in chapter 6. After metallisation with 1.5 nm Cr/ 80 nm Au, the samples were etched in hydrofluoric acid, as detailed in section 6.6, to suspend the graphene 160 nm above the substrate. The finished devices were mounted in a cryostat and then current annealed at $T < 4$ K to remove the residue introduced during the fabrication process (section 6.7). The response of the measured two-terminal conductance G to the applied gate voltage V_g is shown in the inset of fig. 8.1 a). The charge neutrality point lies at $V_g = 2$ V, with $G_{min} \approx 0.6 e^2/h$. Further, the CNP is narrow in V_g , as G is reduced and recovered within $\Delta V_g = 0.5$ V. Away from the CNP the conductance increases to about $4 e^2/h$. The temperature dependence of G_{min} is weak, with a change from $0.5 e^2/h$ at 230 mK to $0.8 e^2/h$ at 4.2 K (not shown).

With the application of a perpendicular magnetic field B , Landau levels form and the conductance becomes quantised. Since we measure the two-terminal Hall effect, we invariably include the contact resistance and electrical wires in the data. Therefore, we correct our data by subtracting a classical, constant series resistor R_c accounting for the above. Even in a two-terminal geometry, the conductance through the graphene ought to coincide with σ_{xy} on the plateaus. Hence, this resistor can be estimated by matching the measured conductance plateau to the next higher quantised conductance value. More specifically, we observe a prominent plateau near $2 e^2/h$ extending to low magnetic fields. Since the $\nu = \pm 2$ state has the largest energy gap and is observed first [92], we believe our choice to be reasonable.

A colour scale plot of G as a function of V_g and B is shown in fig. 8.1 a), with R_c already subtracted. The dominating feature is a plateau at $2 e^2/h$, originating from the $\nu = \pm 2$ filling factor. The second-best developed plateau emerges at

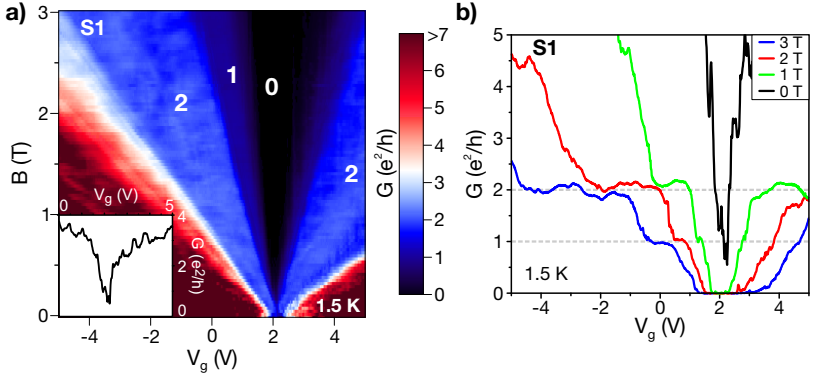


Figure 8.1.: Two-terminal conductance G of device S1 at 1.5 K: **a)** Evolution of the Hall plateaus with the perpendicular magnetic field B and the gate voltage V_g . The plateau at $2 e^2/h$ is the most prominent one. A further plateau at $1 e^2/h$ appears for $B > 0.6$ T. An insulating state, marked as 0, arises at a similar field. A contact resistance of $5 k\Omega$ was subtracted from the data. The inset shows G at zero magnetic field, without the subtraction of R_c . **b)** G as a function of V_g for the indicated magnetic fields. The plateau at $2 e^2/h$ is well developed for holes and electrons, whereas the plateau at $1 e^2/h$ can only be observed for holes. The appropriate R_c was subtracted.

about 0.6 T and deviates from the usually observed sequence of $\nu = \pm 2, \pm 6, \dots$. From the line cuts in fig. 8.1 b), it can be seen that the plateau only occurs at a conductance of $1 e^2/h$ on the hole side. Thus, its filling factor is $\nu = -1$. Such a lifting of a degeneracy of the zero energy Landau level could also be observed in supported samples [92, 96] at fields above 25 T and in other suspended sample [97, 98]. It was attributed to the lifting of the spin and sublattice pseudospin [96].

At the lowest charge carrier densities, the system transits into an insulating phase, marked as 0 in fig. 8.1 a). Whether this phase is the $\nu = 0$ plateau cannot be told from our data, as we cannot measure σ_{xx} independently to check if it goes to zero (as it should for a quantised plateau). Hence we address this phase simply as the $\nu = 0$ state, in compliance with the literature [94, 95].

8.2. Insulating State and Fractional Conductance Plateaus

In the following, we will investigate the $\nu = 0$ state more closely. From fig. 8.1 a) it can be seen that the onset of the insulating phase is close to the CNP at $V_g = 2$ V.

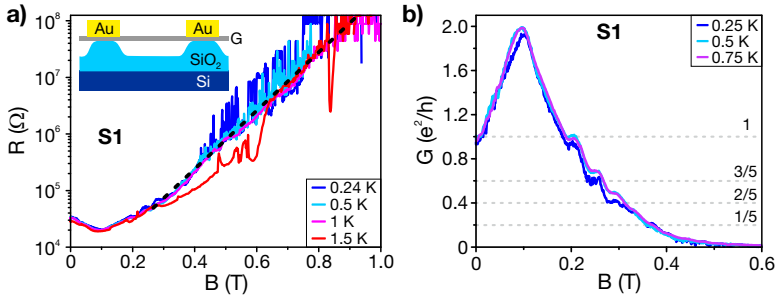


Figure 8.2.: Resistance R and conductance G of S1 in dependence on the magnetic field B for different temperatures T at a fixed gate voltage $V_g = 2$ V at the CNP. **a)** The transition into the $\nu = 0$ state. The measured resistance increases exponentially with B up to the measurable limit of the set-up at 100 M Ω . The slope of the transition is almost unchanged by increasing T from 0.24 K to 1.5 K. The dotted line is a guide to the eye. The inset shows a schematic of the device. The SiO_2 under the graphene (G) was etched where it was not protected by the gold (Au) electrodes. **b)** Before the transition into the $\nu = 0$ state, several Hall plateaus are passed. Values of 1 e^2/h , $3/5$ e^2/h , $2/5$ e^2/h and $1/5$ e^2/h can be observed. The fractional plateaus are weakly developed and strongly temperature dependent. The appropriate R_c was subtracted.

At 1 T the state is fully developed, as indicated by the gate range with $G = 0$ in the line cuts of fig. 8.1 b). Therefore, the transition at $V_g = 2$ V is studied in fig. 8.2 a) as a function of the magnetic field and for different temperatures from 0.24 K up to 1.5 K. The two-terminal resistance R is only weakly temperature dependent at $B = 0$, and thus the curves fall onto each other. With increasing B to 0.1 T, the resistance is first reduced. From there on, R starts to increase exponentially, until the maximal R that our set-up can measure is reached at 0.8 T to 1 T. The increase of R is linear in the log-lin plot, as indicated by the linear guide to the eye (dotted line) in fig. 8.2 a). Consequently, $R \propto e^B$ over a wide range in B . When the temperature is raised from 0.24 K to 1.5 K, the slope of the transitions remains unchanged. However, at 1.5 K R shows instabilities for intermediate B , where R is reduced compared to lower T . For $B > 0.6$ T, the resistance returns to the values of the lower temperature curves. Consequently, we do not observe activated transport in the $\nu = 0$ state. Such a temperature independence was also observed in supported SLG devices [93]. In contrast, for suspended graphene

a temperature activated behaviour was found in [98], yet the fields necessary to reach $R = 100 \text{ M}\Omega$ were with $\sim 5 \text{ T}$ higher than in our device.

The physical origin of the $\nu = 0$ state is under debate, with magnetic catalysis [10, 54, 56], quantum Hall ferromagnets [10, 54, 56, 57, 99] and antiferromagnets [99] being discussed.

Furthermore, we observe conductance plateaus at fractional values of ν . In fig. 8.2 b) the conductance G is shown when the gate is fixed at $V_g = 2 \text{ V}$ and the magnetic field is ramped at different temperatures. Starting from $B = 0 \text{ T}$, the conductance increases from $1 \text{ e}^2/h$ to $2 \text{ e}^2/h$. Most likely, this higher G stems from passing close to the $\nu = 2$ plateau. As the $\nu = 1$ state is crossed at 0.2 T , which was only visible for positive ν in fig. 8.1 b), we are on the hole side of the CNP. At fields higher than 0.2 T , additional plateaus appear near $\frac{3}{5} \text{ e}^2/h$, $\frac{2}{5} \text{ e}^2/h$ and $\frac{1}{5} \text{ e}^2/h$. An increase of the temperature increases G at $\frac{3}{5} \text{ e}^2/h$ and $\frac{2}{5} \text{ e}^2/h$ noticeably stronger than on the other plateaus. However, up to date only fractions of $\frac{1}{3}$, $\frac{1}{2}$ and $\frac{2}{3}$ have been reported for suspended SLG [97, 98, 100]. On the other hand, graphene on a boron nitride substrate showed fractions at different filling factors [101] than its suspended counterparts. And a series of fifths was measured in semiconductor 2DES [102].

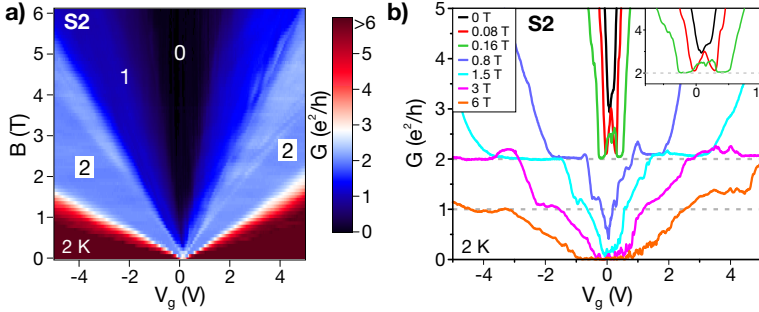


Figure 8.3.: Two-terminal conductance G in device S2 as a function of the gate V_g and the magnetic field B at 2 K . **a)** Colour scale of G . The $\nu = \pm 2$ state extends to very low fields. A plateau at $1 \text{ e}^2/h$ appears on the hole side and the insulating state at $\nu = 0$ forms above 1.5 T . **b)** G as function of V_g for different B . The plateaus at 2 , 1 and $0 \text{ e}^2/h$ are well developed. Further, the $\nu = \pm 2$ state extends to very low fields. The inset in the upper right corner shows a zoom of the low field conductance near the CNP. The plateau at $2 \text{ e}^2/h$ appears at 80 mT and is fully developed at 160 mT . The R_c was subtracted.

Generally, there is a competition between the fractional Hall plateaus and the

insulating state at $\nu = 0$ [97, 98]. In principle, the plateaus should become more accentuated at larger magnetic fields. Yet, at the filling factors where the fractional plateaus would be expected, we find the insulating phase.

8.3. The $\nu = \pm 2$ State at Vanishing Magnetic Field

One further striking feature of the data in fig. 8.1 is that the $\nu = \pm 2$ state extends to very low magnetic fields in S1. To ensure that this is not a coincidence, we investigated a second device, S2, with a different aspect ratio due to $L = 1 \mu\text{m}$ and $W = 2 \mu\text{m}$.

In fig. 8.3, the conductance G of S2 is shown in dependence on the gate voltage V_g and the perpendicular magnetic field B at 2 K. A series resistance of $4.3 \text{ k}\Omega$ was subtracted to account for R_c . Similar features than in the previous device can be seen in fig. 8.3 a), with plateaus at $2 e^2/h$ and $1 e^2/h$ and an insulating phase above a critical magnetic field. The CNP lies very close to $V_g = 0 \text{ V}$, which indicates that very little charged impurities are on the flake.

Figure 8.3 b) shows that the minimum conductance at the CNP lies around $3 e^2/h$ at zero magnetic field. When a field of 80 mT is applied, the single CNP splits into two minima of $2 e^2/h$. At 160 mT , a plateau at $2 e^2/h$ is already well-developed.

In reference [103], a quantised conductance of $2 e^2/h$ could be observed to zero magnetic field. However, this phenomenon was attributed to the formation of a nano-constriction in the graphene flake during the current annealing. It is worth noting, that we did not observe such etching events in any of our samples and therefore, the low-field $\nu = \pm 2$ state must originate from a different physical process. In theoretical studies, two major classes of physical effects were suggested, that could explain a quantised conductance at very low or zero B : mechanical strain [104] or electron-electron interaction [105]. The mechanical strain can arise from the clamping of the graphene flake by the metallic contacts. Whereas the graphene is thought to expand when cooled, i.e. has a negative expansion coefficient [106–108], the contraction of the electrodes might still induce mechanical strain along the flake. Notwithstanding, after cooling the samples to cryogenic temperature, current annealing them and warming up again, we do not observe any Raman-signatures that could be attributed to strain [109]. Furthermore, such strain should also appear in high quality supported devices, which was not reported up to date. The situation at cryogenic temperatures is however not controllable with our equipment.

In favour of the e-e interaction speaks that the removal of the substrate lowers the effective ϵ_r , which increases the interaction parameter r_s .

8.4. Summary

To summarise, we have presented two-terminal measurements of the quantum Hall effect in suspended single layer graphene devices. The devices exhibit a sharp dip in G around the CNP, indicating a high electronic mobility, and the position close to $V_g = 0$ V hints at a low impurity concentration on the flakes. A prominent conductance plateau at $2 e^2/h$, belonging to the zero energy Landau level, can be observed even in a magnetic field of ~ 80 mT. At higher fields, a plateau at $1 e^2/h$ appears together with an insulating phase at $\nu = 0$. Further inspection of the transition into the state at $\nu = 0$ reveals that the resistance increases exponentially with the applied B . No significant temperature dependence can be found between 240 mK and 1.5 K. In addition, traces of fractional conductance plateaus were measured.

SUSPENDED TWO-TERMINAL BILAYER GRAPHENE

This chapter presents our results on two-terminal suspended bilayer graphene (BLG) devices. Two different types of BLG devices can be observed. In one sample type, the $\nu = \pm 4$ state extends to very low fields, similar to $\nu = \pm 2$ state in the single layer graphene in the previous chapter. In a second type of sample, the conductance at the CNP is almost suppressed. In dI/dV spectroscopy, a gapped state at zero magnetic field is found, suggesting an insulating spontaneously broken symmetry state.

Bilayer graphene provides a further class of interacting 2DES [12]. In contrast to single layer graphene, the chiral charge carriers are massive due to the coupling between the two layers [110, 111]. Like single layer graphene, BLG is a 2DES which can host a large variety of ground states. Celebrated examples of such states in 2DES are the fractional quantum-Hall effect [97, 98, 112] and the Wigner crystal [113], both being driven by Coulomb interaction. In BLG a wealth of ground states has been predicted [58, 59, 61, 62, 114, 115], owing to the large number of symmetries such as spin, pseudospin, layer, valley pseudospin or the zero-energy Landau level degeneracy. These predicted states include states in which a gap forms spontaneously in zero magnetic and electric field, as opposed to the induced gap caused by the application of an external field [116–118] or mechanical strain [24, 119]. Unlike in single layer graphene, the interaction parameter r_s is not constant but increases for low carrier concentrations n in BLG (eq. 2.17). To reach a low minimal n at the charge neutrality point (CNP), the effective disorder potential has to be sufficiently small. This can be achieved by suspending the graphene sheet [26] and current annealing [120] the device. In addition, as for single layer graphene, the lower effective ϵ_r after removing the SiO_2 increases r_s in BLG even further.

Bilayer graphene has an eightfold degenerate Landau level (LL) at zero energy. As the Hall conductivity is quantized at values of $\sigma_{xy} = \nu \cdot e^2/h$, where the filling

factor ν is given by $\nu = \pm 4(N + 1)$, a step of $8 e^2/h$ is observed from $\nu = -4$ to $\nu = 4$ around the CNP [111]. A lifting of the spin symmetry, for example, manifests itself in the appearance of new Hall plateaus, of which the $\nu = 0$ is the most prominent one [121]. If all symmetries are lifted, quantum Hall plateaus appear at filling factors $\nu = 0, \pm 1, \pm 2, \pm 3, \dots$. Magnetic fields of 30–45 T were required to see this lifting in SiO₂ supported devices, for both single [92] and bilayer graphene [122], until Feldman *et al.* succeeded in observing the effect at low magnetic fields in suspended bilayer graphene [121].

The most striking state is the $\nu = 0$ state, whose nature is under debate for both single layer [94, 95, 123], as mentioned in the previous chapter, and bilayer graphene [118, 121, 122]. For bilayer graphene, several possibilities are being discussed, such as the quantum Hall ferromagnet (QHF) [57, 63, 115], the quantum anomalous Hall insulator (AHI) [61, 124], or a ferroelectric phase [114].

We report on suspended and current annealed bilayer samples. We find two kind of samples, B1 and B2, where B2 represents a new class. Differential conductance spectroscopy reveals that B2 samples are evidently gapped at the CNP in zero magnetic and electric field. Since B2 samples were annealed for an extended period we think that they are cleaner than B1 samples. Furthermore, exposure to air and thus contamination of the flake with charged impurities, transforms B2 into type B1. Subsequent current annealing restores the B2-type properties.

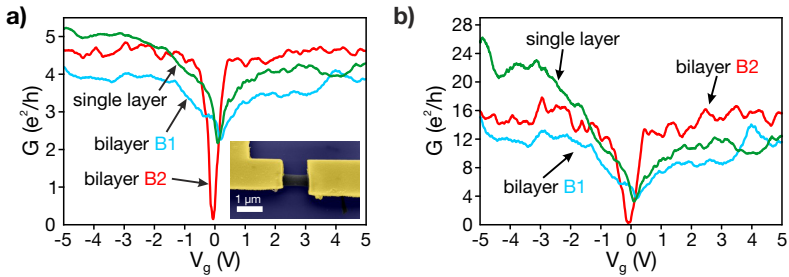


Figure 9.1.: Gate response of suspended graphene devices. **a)** Comparison of the measured dependence of the conductance G on the applied gate voltage V_g for three suspended devices: single layer graphene (length \times width $1 \times 2 \mu\text{m}^2$, $T = 2$ K), bilayer type B1 ($2 \times 0.8 \mu\text{m}^2$, $T = 230$ mK), and bilayer type B2 ($1 \times 1.5 \mu\text{m}^2$, $T = 230$ mK). In **b)** the contact resistance was subtracted.

The suspended BLG devices were fabricated as described in chapter 6. Sample B1 has the dimensions length $L = 2 \mu\text{m}$ and width $W = 0.8 \mu\text{m}$. The samples of

type B2 are approximately $L = 1 \mu\text{m}$ long and $W = 1.5 \mu\text{m}$ wide. The graphene is contacted with 1 nm Cr and 70 nm Au. Then the devices were annealed for several hours in vacuum (10^{-7} mbar) at 200°C and in order to suspend the devices about 160 nm of SiO_2 were removed in a HF etch. The number of graphene layers was determined by Raman spectroscopy. After mounting a device into a ^3He cryostat, the devices were current annealed at 1.5 K. Conductance measurements were carried out with a lock-in amplifier applying a $20 \mu\text{V}$ AC voltage. For the dI/dV spectroscopy the AC signal was superimposed onto a DC bias voltage.

9.1. Gate Response of B1 and B2

Figure 9.1 shows representative measurements of the two-terminal conductance G of suspended graphene devices when n is altered by the back-gate voltage V_g . The CNP is close to $V_g = 0$ V for all samples, indicating that only few charged impurities reside on the graphene. Both single layer and bilayers of type B1 display a smooth transition from low G at the CNP to higher G values at larger n , as expected from the V-shaped conductances found in recent literature [121, 125, 126]. In contrast, bilayer samples of type B2 are very low conducting at the CNP with $G_{\min} < 0.2 e^2/h$ at 230 mK, which is considerably lower than in previous reports [118]. Furthermore, as the gate voltage is tuned away from the CNP, G increases sharply and then quickly saturates for $|V_g| > 0.5$ V. Note, that this is even the case when the contact resistance is subtracted as shown in fig. 9.1 b).

9.2. QHE in Suspended Bilayer Graphene Devices

When placed in a perpendicular magnetic field B , samples B1 and B2 reveal substantially different quantum Hall features, as shown in fig. 9.2. As the measurements were performed in a two-terminal configuration, they include a contact resistance [51]. We extract the contact resistance R_c in the following way: The conductance G is plotted as measured and each identifiable Hall plateau in the conductance is assigned to the next higher allowed filling factor ν . For example, a plateau at $G = 0.9 e^2/h$ would be set to $\nu = 1$. Then G is converted into resistance and plotted against $1/\nu$, as shown in fig. 9.3 a) for sample B2 at 1.5 K. A linear fit is made and the intercept at $\nu \rightarrow \infty$, or $1/\nu \rightarrow 0$, is R_c . This contact resistance is assumed to be purely classical and largely independent of the charge carrier density in the system or the applied perpendicular magnetic field.

First, we will discuss sample B1 and then move to sample B2.

In sample B1 we observe a partial lifting of the eightfold zero energy LL degeneracy, leading to the $\nu = \pm 2$ and $\nu = 0$ states above a critical magnetic field of $B_{\text{crit}} \approx 0.75$ T (fig. 9.2 a)). In the magnetic field range $0 \leq B \leq 0.75$ T we observe

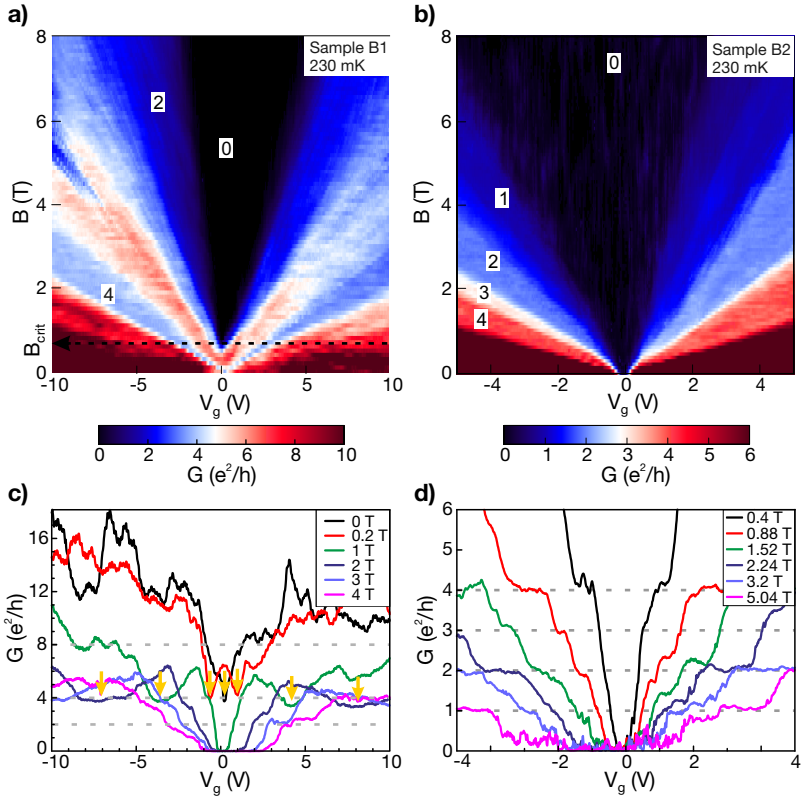


Figure 9.2.: The dependence of the linear conductance G on the gate voltage V_g and perpendicular magnetic field B reveals two types of samples. In sample B1, shown in **a)** and **c)** the plateaus at filling factors $\nu = 0, \pm 2$ and ± 4 are well developed. The $\nu = \pm 4$ plateau (minima in **c)**, see arrows) extends to very low magnetic fields. For sample B2, a full lifting of the eightfold Landau level degeneracy is observed, as plateaus at odd fillings appear as well. The curves in **c)** and **d)** show G as function of V_g at constant B . Appropriate contact resistances were subtracted.

the same Hall sequence as in conventional devices where the conductance has a step of $8 e^2/h$ from $\nu = -4$ to $+4$. When applying $B > B_{crit}$ an insulating state

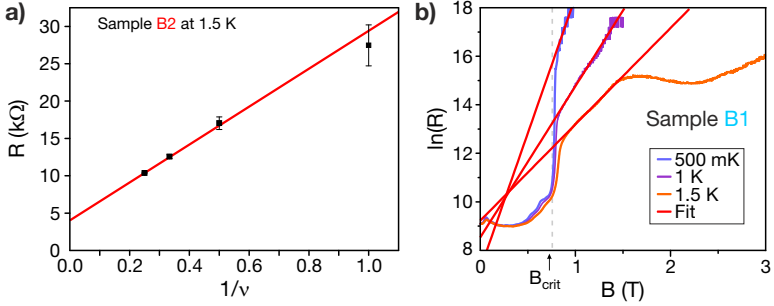


Figure 9.3.: **a)** Plot of the resistance of the Hall plateaus against the inverse of the filling factor ν . The line is a linear fit of the data and its offset at $1/\nu \rightarrow 0$ yields the two-terminal contact resistance of $R_c \approx 4$ k Ω . The error bars mark the read-out error. **b)** The Log-lin plot of the resistance R of B1 near the CNP as a function of the magnetic field B for different temperatures. Above B_{crit} , bilayer graphene enters the insulating $\nu = 0$ state, which exhibits a thermally activated behaviour. In the activated regime, $\ln(R)$ is inversely proportional to temperature and proportional to B

emerges around the CNP, followed by the $\nu = \pm 2$ state with a two-fold degeneracy remaining. We also note that the $\nu = \pm 4$ state appears to extend all the way down to the CNP at zero magnetic field [61, 127]. The corresponding line cuts from the color scale are shown in fig. 9.2 c) to illustrate the evolution of the CNP into the $\nu = \pm 4$ state at low fields and the appearance of the broken symmetry states $\nu = 0$ and ± 2 at higher fields [121]. Unlike sample B1, B2 shows a fully lifted zero-energy LL, manifesting in the appearance of Hall plateaus for odd filling factors ν . In analogy to sample B1, we label the low conducting region around the CNP in sample B2 with $\nu = 0$, although this state maintains a finite conductance as we will discuss below.

In the following fig. 9.4 we investigate the properties of the low conducting state at $\nu = 0$ at low charge carrier density as a function of B and T for both samples. For device B1, shown in fig. 9.4 a), we find that at low B the resistance R at the CNP remains around $R = 6$ k Ω , but when a critical perpendicular magnetic field of $B_{crit} \approx 0.75$ T is reached, it increases sharply to $10^8 \Omega$, the maximum resistance that our measurement set-up can resolve. This behavior can be attributed to the formation of a quantum Hall state at $\nu = 0$ [94].

Such a state can occur because of the lifting of the zero energy Landau level (LL). After the lifting the Fermi energy E_F , corresponding to the charge neutral

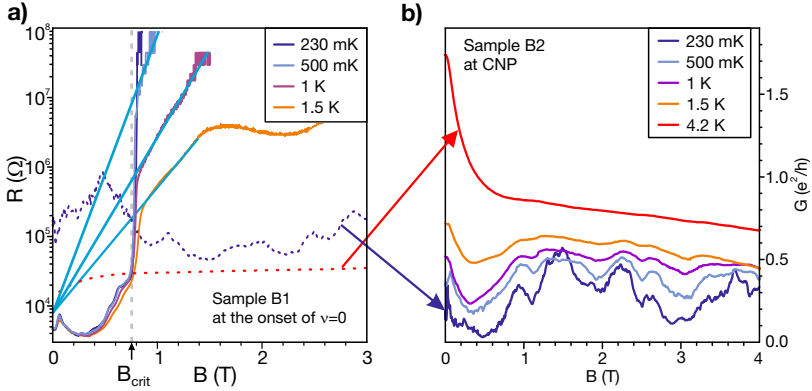


Figure 9.4.: Difference in **a)** resistance R of sample B1 and **b)** conductance G of sample B2 as a function of magnetic field B at the CNP. A sharp transition to an insulating $\nu = 0$ state appears at $B_{crit} = 0.75$ T (arrow) in B1. In this state, R is thermally activated with an activation energy ΔE proportional to B . The lines are guides to the eyes for this dependence. For comparison we show the resistance data for sample type B2 (dotted) within the same graph. In contrast to sample B1, sample B2 does not show a field-induced transition to an insulating state. At low temperatures, G is remarkably insensitive to B , but displays a relatively low conductance value $< e^2/h$. Appropriate contact resistances are subtracted.

case, will be positioned in between the two LLs at energy E^+ and $E^- = -E^+$. This leads to the quantization of the Hall conductance $\sigma_{xy} = \nu e^2/h$ with filling factor $\nu = 0$ in this case, hence, $\sigma_{xy} = 0$. At the same time the dissipative conductance σ_{xx} tends to zero, displaying a thermally activated dependence according to $\sigma_{xx} \propto \exp(-\Delta E/2k_B T)$, where $\Delta E = E^+ - E^-$ is the activation energy. For the measured electrical resistance R we then expect the following dependence:

$$R = R_0 e^{\Delta E/2k_B T}. \quad (9.1)$$

In an electron system with massive electrons (effective mass m^*), as is the case for bilayer graphene, adjacent Landau levels are expected to be spaced by the energy $\Delta E = \hbar\omega_c$, where $\omega_c = eB/m^*$ is the cyclotron frequency. The dependence of $\ln(R)$ on B should therefore display a linear dependence on the magnetic field B , which is indeed seen in fig. 9.3 b) for magnetic fields above the critical field B_{crit} . In addition, and in agreement with thermal activation, the

slope increases with decreasing temperature T . Assuming $\Delta E = \hbar\omega_c$ and fitting the measurements to the prediction, yields $m^* = 0.1 \pm 0.01 m_e$, which is roughly three times the theoretical value of $m^* \approx 0.033 m_e$ [12]. Although the result of a slightly increased mass maybe plausible, we stress that the analysis in this form is incorrect. Assuming $\Delta E = \hbar\omega_c$ means accepting the result from the non-interacting Fermi gas. The non-interacting model provides, however, no mechanism for the lifting of the zero-energy Landau level. Hence, it is better to talk of an apparent energy gap ΔE which is proportional to B and amounts to ≈ 13 K/T (Kelvin per Tesla) or 1.1 meV/T. Note, that this number is much larger than the Zeeman splitting, only amounting to ~ 0.7 K/T. Feldman *et al.* [121] deduce in their experiment $\Delta E = 3.5\text{--}10.5$ K/T, which is somewhat lower than our number. In a recent theory, taking interactions into account, the energy gap of the $\nu = 0$ state has been calculated to be 14.3 K/T [115].

The dotted curves in fig. 9.4 a) show the resistance R of B2 in direct comparison to that of B1 at 230 mK and 4 K. We find that at $B = 0$ T, B2 has an order of magnitude higher R than B1, whereas at higher magnetic fields, B1 is several orders more resistive. fig. 9.4 b) elaborates on the conductance of B2 at the CNP as a function of B and temperature. Most notably, G at $B \gtrsim 1$ T is nearly independent of B with the exception of fluctuations most likely caused by interference due to remaining localized states [97].

The marked differences in the magnetic field dependence clearly demonstrate that sample B1 and B2 differ. In sample B1, the LL degeneracy is partially lifted for $B > B_{crit} \approx 0.75$ T, revealing plateaus at $\nu = \pm 4$, $\nu = \pm 2$, and $\nu = 0$. On the other hand, sample B2 reveals a fully lifted LL, where all plateaus appear already at a small $B \sim 1$ T. Furthermore, sample B2 stays conductive at the CNP even at higher B of up to 8 T. We note, that sample B1 is similar in characteristics to the one reported by Feldman *et al.* [121], whereas B2 shows new features.

9.3. *dI/dV Spectroscopy of a Spontaneously Gapped State at Zero Magnetic Field*

We further investigate the nature of sample B2 by measuring the differential conductance G_d as a function of the applied DC bias V_{sd} between source and drain contacts at $B = 0$ T at the CNP ($V_g = -0.1$ V), where G_d is suppressed. fig. 9.5 a) summarizes the findings for different temperatures from 226 mK to 4 K (no contact resistance subtracted). Two gaps can clearly be identified: When going from large source-drain bias $V_{sd} > 4$ mV towards small voltages, the larger gap Δ sets in at $V_{sd} = \pm 2.5$ mV, where G_d is decreased from around $4 e^2/h$ to $0.9 e^2/h$ in the data measured at 226 mK. The smaller gap δ appears at voltages $|V_{sd}| \lesssim 0.35$ mV and it reduces G_d from $0.9 e^2/h$ to less than $0.2 e^2/h$.

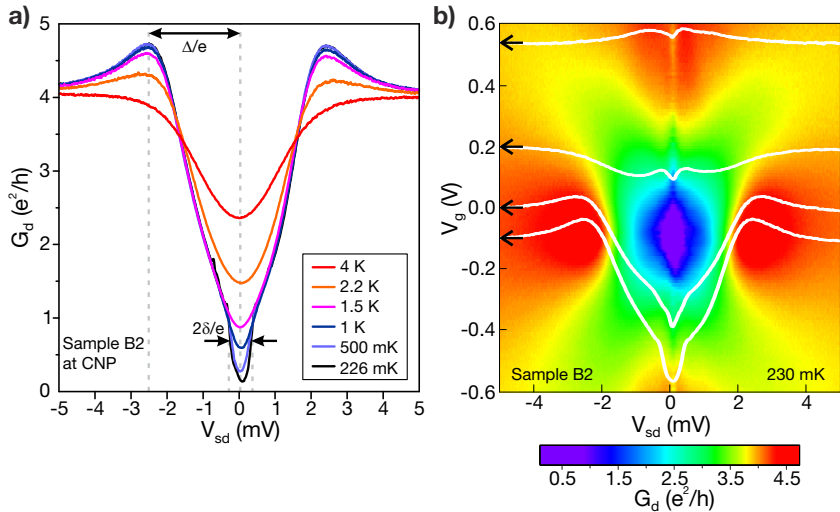


Figure 9.5: **a)** Temperature dependence of the differential conductance G_d around the CNP of sample B2 as a function of the source-drain bias voltage V_{sd} . Two gaps with size $\Delta = 2.5$ meV and $\delta = 0.35$ meV appear that both display a distinct temperature dependence. **b)** Colour-scale of G_d as a function of V_{sd} and gate voltage V_g at 230 mK. Line cuts are taken at the values of V_g marked by the arrows.

By increasing the temperature from 226 mK on, the smaller gap δ is first reduced and then vanishes at 1 K.

In order to identify the origin of these two gaps, a color scale plot of the differential conductance G_d against V_{sd} and the gate voltage V_g at 230 mK is shown in fig. 9.5 b). The line cut at the CNP ($V_g = -0.1$ V) shows again the two gaps in electron transport. As V_g and thus the charge carrier concentration is increased, the two gaps exhibit distinct changes. The larger gap Δ disappears, while the smaller gap δ still exists in the metallic graphene regime at $V_g > 0.5$ V, but with a less pronounced dip. This behaviour is qualitatively consistent with Coulomb charging of the whole flake [128]. We estimate a single-electron charging energy of 1 meV for a flake of width 1.5 μm . Because the contact conductances of $\sim 4\text{--}8$ e^2/h are substantially larger than e^2/h , charge quantization is only weak and no strong Coulomb blockade gap is expected. One rather expects the conductance to display a ‘weak’ conductance suppression by something like 25–50 % around zero bias, in agreement with the observation. In contrast to the small gap, the

larger gap Δ is strongly dependent on the charge carrier density. At the CNP, it has its maximum magnitude, but only slightly away it starts to close. The line cut at $V_g = 0.2$ V already bears little sign of the gap Δ . We therefore conclude that it must be a feature intrinsic to the low-energy band structure of bilayer graphene and that this gap is formed spontaneously at zero magnetic and at zero electric field. We emphasize that the electric field due to the back-gate voltage in the vicinity of the gap feature is negligible.

In the tight-binding band structure calculation of McCann [116], opening a gap equivalent to our observed gap of $\Delta = 2.5$ mV would require a back-gate voltage of at least 10 V.

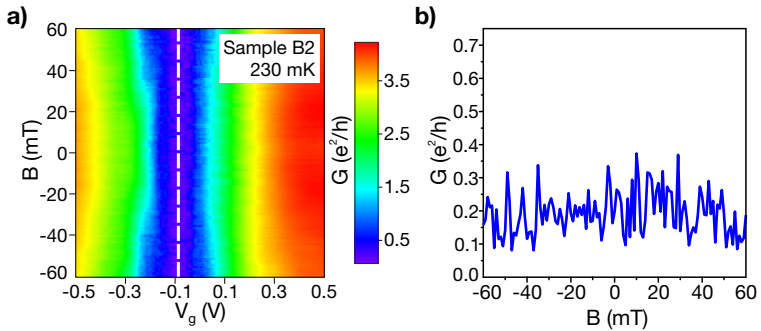


Figure 9.6.: Absence of a phase transition close to the CNP in B2. **a)** Colour scale of the conductance G of sample B2 as a function of gate voltage V_g and magnetic field B . There is no transition into another phase with magnetic field, which would manifest as a notable change in conductance. **b)** Line profile taken at the CNP, as indicated by the dashed line in a).

The Δ gap can be associated with the $\nu = 0$ state, as the low-conductance region in the color scale plot of fig. 9.2 b) extends from large magnetic fields all the way down to zero magnetic field with no apparent phase boundary. In fig. 9.6 a), a colour scale plot of the conductance G of sample B2 is shown as a function of gate voltage V_g and magnetic field B . We have looked carefully into the region of low magnetic field close to the CNP to rule out any additional phase transitions. Based on a peak that occurred in G at around 40 mT, Weitz *et al.* suggested the appearance of yet another phase [118]. For sample B2, G is constant with the exception of fluctuations as shown in fig. 9.6 b).

Although sample B1 and B2 have a $\nu = 0$ state around the CNP in our argument, these states are electrically different. In sample B1, the resistance evidently

increases to infinity, whereas it stays finite in B2. This difference can be explained by insulating phases, which differ in their edge-state structure [61, 62, 124].

Sample B1 has two phases, a low-magnetic field phase and a broken symmetry state induced by a small magnetic field of $B > B_{crit}$. The latter most likely is a quantum Hall ferromagnet [57, 61, 115]. The phase at low magnetic field has been assigned to a gapped anomalous Hall insulator (AHI) in which topologically protected edge states should provide a conductance of up to $4 e^2/h$ [61, 62, 127]. This scenario is somewhat supported by the quantum Hall states at $\nu = \pm 4$ that persist all the way down to $B = 0$ (see arrows in fig. 9.2 c)). A similar observation has been made in compressibility measurements by Martin *et al.* [127].

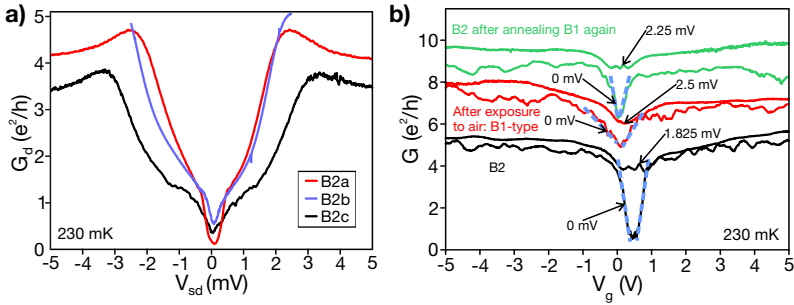


Figure 9.7.: **a)** The differential conductance G_d as a function of V_{sd} at 230 mK for three samples of type B2. In all three, a larger gap of size $\Delta = 2\text{--}3$ meV and a smaller one of size $\delta \approx 0.2\text{--}0.5$ meV are clearly visible. **b)** G at 230 mK as a function of V_{gate} and V_{sd} in sample B2 before and after exposure to air. Initially, the sample showed a pronounced CNP and applying V_{sd} changed the conductance strongly (black pair of curves). After exposure to air, the CNP is higher conducting and applying a bias has only a small effect (red curve pair, shifted by $3 e^2/h$). Re-annealing the sample yields a steeper CNP and recovers the gap feature (green pair of curves, shifted by $6 e^2/h$).

As an indication of the disorder strength in the two sample types we refer to the following observations. Sample B2 was warmed up to room temperature and exposed to air, which exposed the device to charged and uncharged molecules such as water. After cooling the sample down again, the gap feature disappeared and like sample B1 a transition from conductive to insulating could be observed in perpendicular magnetic field. Subsequently, we current annealed the sample

again and were able to recover a very similar gap-feature as before the exposure to air. Figure 9.7 b) shows G as a function of V_{gate} for the three cases. Before the warm-up, B2 showed a pronounced dip in G at the CNP (black curve). Applying a bias of 1.8 mV almost closes the gap and increases G at the CNP significantly. After exposure to air, the gate response is shallow at the CNP and the minimum conductance above $2 e^2/h$ (green curve), similar to B1. Furthermore, applying a bias had less effect than in the pristine B2 device. Finally, current annealing of the sample at 1.5 K recovers a steep dip in G near the CNP and a $G_{\min} \approx 0.4 e^2/h$ (red curve). As before exposure to air, the sample shows a strong response to the bias voltage. Therefore, we deduce that samples of type B2 are cleaner than the type B1 ones.

Because B2 is the cleaner sample of the two, we rather think that the low-field phase of B1 is a normal state, not a broken symmetry state. In contrast, the low-density phase of B2 is a broken symmetry state. To explain the finite conductance we propose edge states in the B2 phase. If we subtract the small gap δ in sample B2, the measured conductance G is $\approx 0.8 e^2/h$, which is smaller than the ballistic channel conductance of any gapped phase with edge states. This suggests that the gapped phase is either not single domain or that the edge states are not topologically protected, allowing for partial back-scattering. On the other hand, due to the two-terminal measurement set-up the contact resistance can still influence G . Since R_c is likely to change with the application of V_{sd} we refrained from subtracting it from the shown data. Further work is needed to determine the nature of the edge states and assign it to broken electron-hole, valley or spin-symmetry [61, 62, 129, 130].

Furthermore, we would like to stress that these spontaneous gaps were found in more than one device. In fig. 9.7 a) the dI/dV spectroscopy of three two-terminal devices is presented. Whereas sample B2a and B2b are different devices, B2c is B2b after thermal cycling, exposure to air and subsequent current annealing, as also explained in fig. 9.7 b). Although the gap-sizes are not identical in all three devices, they exhibit the same features with one large gap Δ and a smaller one, δ . In an independent work, Velasco *et al.* applied dI/dV spectroscopy to clean suspended bilayer graphene samples, and observed a similar gap-feature [131].

9.4. dI/dV Spectroscopy of Samples with $G_{\min} \approx 4 e^2/h$

Moreover, the same dI/dV spectroscopy as applied to samples of type B2 can be used to explore the properties of type B1. We investigate a BLG device of $L = 2 \mu\text{m}$ and $W = 2.3 \mu\text{m}$, which shows a $\nu = \pm 4$ state extending to very low magnetic fields, as in fig. 9.2 a). The measurements were carried out in a ^4He cryostat with a base temperature of 1.5 K. The conductance at the CNP in zero

magnetic field lies very close to $G_{min} = 4 e^2/h$. Figure 9.8 summarises our findings when V_{sd} is applied to this sample of type B1.

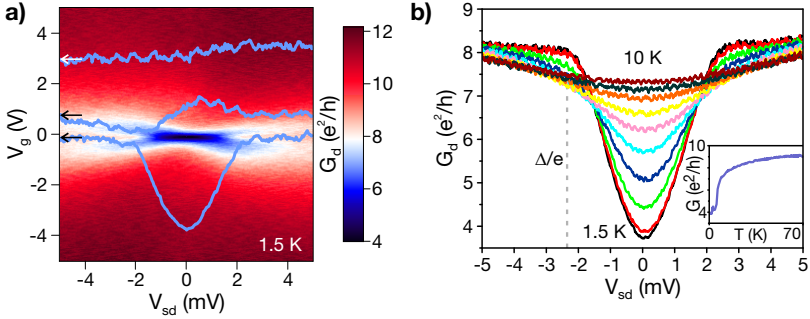


Figure 9.8.: dl/dV spectroscopy on a device of type B1. **a)** The differential conductance G_d as a function of the gate V_g and the applied DC bias V_{sd} at 1.5 K. At the CNP, close to $V_g = 0$, G_{min} lies at $4 e^2/h$. When $V_{sd} \approx 2.4$ meV is applied, a $G_d \approx 8 e^2/h$ is recovered, as shown by the overlaid line cuts at the V_g indicated by the arrows. Away from the CNP, the gap vanishes quickly. In the metallic regime at $V_g = 3$ V no gap-like feature remains. **b)** Temperature dependence of the gap Δ at the CNP. At 1.5 K, the gap feature is well-developed. Increasing T raises G_d for $V_{sd} < \Delta/e$, until at 10 K the gap is suppressed. The inset shows G at the CNP for a larger temperature range.

In fig. 9.8 a) the differential conductance G_d is shown as a function of V_g and V_{sd} . Close to the CNP at $V_g \approx 0$ V, the response to the bias voltage is the strongest. When a DC bias is applied, G_d increases from $4 e^2/h$ at $V_{sd} = 0$ to about $8 e^2/h$ at $V_{sd} = 2.4$ mV and saturates there. When the charge carrier density is tuned away from the CNP, a peak-like structure develops around $V_{sd} = 0$. At higher V_g , the gap-like feature vanishes completely, as can be seen from the cuts overlaid in fig. 9.8 a). The maximum span of the apparent gap is $\Delta/e \approx 2.4$ mV. There are some notable differences compared to the data from B2. First, the conductance at the CNP is with $4 e^2/h$ in B1 considerably higher than for the B2 samples, where $G_{min} < 1 e^2/h$ at 1.5 K. With respect to the gap features revealed by the dl/dV spectroscopy, we find only one gap in B1, corresponding in size to Δ in B2. The smaller gap δ is absent in B1. However, at the minimal T of 1.5 K, the smaller gap was also suppressed in B2. A further difference is the lack of the BCS-like shoulders found in B2. In B1, the conductance outside the gapped region is virtually constant.

Figure 9.8 b) shows the temperature dependence of the gap Δ at the CNP. At the lowest temperature $T = 1.5$ K, the gap reduces the conductance from $8 e^2/h$ to $4 e^2/h$. With increasing T , the gap is diminishing and vanishes at about 10 K. At $T = 10$ K, no gap structure remains and G_d increases smoothly with the applied V_{sd} . However, similar to B2 in fig. 9.5 a), the conductance at $V_{sd} = \Delta/e$ is reduced at higher T , despite the absence of the shoulders in B1.

Moreover, the inset of fig. 9.8 b) shows the temperature dependence of the conductance at the CNP for a range from 1.5 K to 70 K. A steep increase in G occurs from 1.5 K up to 10 K, which agrees with the observation that the gap closes around 10 K. The further increase in G is rather $\propto \sqrt{T}$ from 10 K to 70 K. Mayorov *et al.* found a deviating temperature dependence [132] in suspended BLG devices when studying the low B QHE. In their measurements, G increases strictly linear with T .

9.5. Summary

In conclusion, using differential conductance spectroscopy we found a new type of bilayer whose spectral density is gapped at zero magnetic and zero electric field. Though this state is due to an insulating phase, the non-vanishing conductance $\approx 0.8 e^2/h$, which is surprisingly robust in magnetic field, suggests that edge states are present.

We further investigated with dI/dV spectroscopy samples in which the $\nu = \pm 4$ state extends to very low magnetic fields. We found a gapped phase at zero magnetic field with a remnant conductance of $4 e^2/h$.

SUSPENDED BILAYER GRAPHENE HALL CROSSES

In this chapter, we present results on suspended bilayer graphene (BLG) Hall crosses. In contrast to the two-terminal measurement set-up of the previous chapter, the Hall cross geometry allows for the simultaneous measurement of the Hall voltage. Thus we can record σ_{xy} independently from the mix of σ_{xx} and σ_{xy} in the two-terminal data.

Further, with the additional terminals we were able to investigate the homogeneity of our current annealed samples to a greater extend. We find that the flakes separate into regions of low disorder and parts that do not benefit from the annealing.

In a next step, the two-terminal data and the quantum Hall conductance are presented and discussed. A complete lifting of the lowest Landau level is found. We investigate the Hall effect at the low conducting phase at zero magnetic field B . However, in our devices, we cannot observe any quantised charge transport at zero magnetic field.

Additionally, we study the magnetic field dependence of the spontaneously gapped state at the CNP by means of dI/dV spectroscopy and present a low conducting state and a fully insulating one.

10.1. Homogeneity of Current Annealed Bilayer Graphene Devices

In difference to the two-terminal suspended bilayer graphene devices presented in the previous chapter, the suspended Hall crosses were fabricated with an aluminium sacrificial layer on top (see chapter 6). This layer protects the graphene from contamination during the processing, resulting in a higher yield of cleaner devices. On the other hand, the Hall cross geometry is fragile due to the longer

distances over which the graphene has to be suspended to accommodate the additional contacts. The samples presented below are asymmetric, with a contact pair about $3 \mu\text{m}$ apart, and a pair separated by $2 \mu\text{m}$, as shown in fig. 10.1 a). Choosing a shorter spacing of the electrodes resulted in unusable measurements, likely caused by hot spots near the contacts (see supplementary information of [121]).

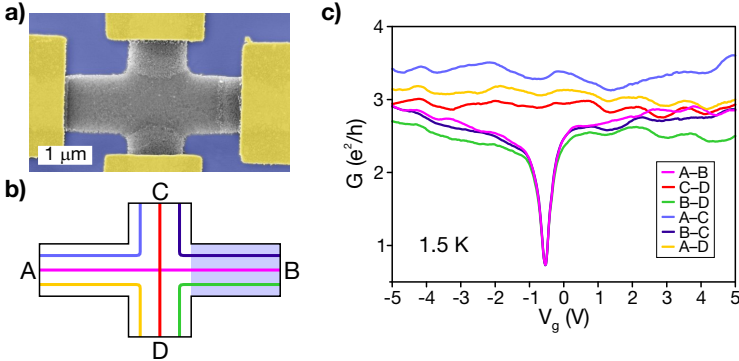


Figure 10.1: **a)** False colour SEM micrograph of a bilayer graphene Hall cross (grey), contacted by four electrodes (yellow) and suspended 160 nm above the substrate (blue). The scale bar corresponds to $1 \mu\text{m}$. **b)** Schematic of the Hall cross HC1. The possible two-terminal configurations of contacts A,B,C,D are colour-coded. **c)** Two-terminal conductance G of device HC1 as function of the back-gate V_g for all contacts pairs from b). The colours correspond to b). A CNP is only visible when the current flows through contact B.

The additional contact pair allows us to investigate the spacial homogeneity of the bilayer graphene devices after current annealing at 1.5 K . We used the current annealing process described in chapter 6. One contact is electrically grounded while a DC voltage is applied to one of the remaining contacts. In the following, we will discuss an inhomogeneous bilayer graphene device named HC1. In this device, contacts A and B are $3.3 \mu\text{m}$ apart, C and D $2.1 \mu\text{m}$ and the width of the flake is about $1 \mu\text{m}$. After successful annealing of HC1, a CNP appeared in the graphene between the two annealed contacts (pink curve in fig. 10.1 c)). However, all segments of the flake can be investigated separately by measuring all possible two-terminal combinations, as shown in fig. 10.1 b). In fig. 10.1 c) the measured two-terminal conductances G are plotted as a function of the back-gate voltage V_g . We find that the graphene between contacts A and B

used for the annealing exhibits a pronounced dip in G at $V_g \approx -0.5$ V, stemming from the CNP. All combinations which involve contact B show this feature, with a minimum of $G \approx 0.7 e^2/h$ at the CNP, independent of the aspect ratio of the investigated segment. On the other hand, the remaining three combinations show a virtually flat gate-response and lack a CNP. Therefore, the device must consist of a region of clean graphene adjacent to contact B, whereas the other contacts are connected by disordered and doped graphene.

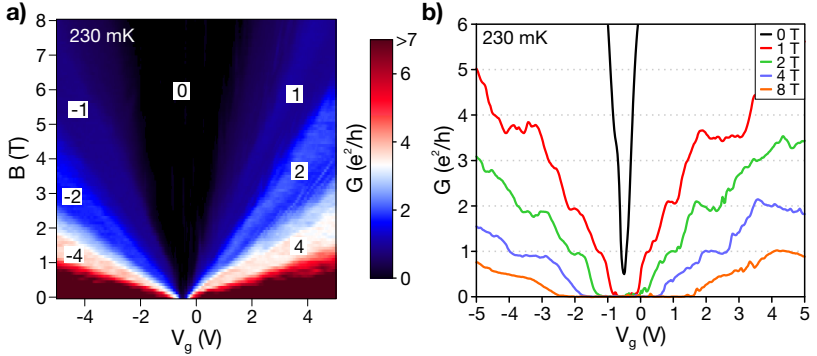


Figure 10.2.: Two-terminal quantum Hall effect at 230 mK measured between contacts A and B of device HC1. **a)** Colour scale of the conductance G as a function of the gate V_g and the perpendicular magnetic field B . Hall plateaus can be identified at filling factors $\nu = \pm 4, \pm 2, \pm 1$. At $\nu = 0$, an insulating phase evolves with increasing B . **b)** G as a function of V_g at the given values of B . The Hall plateaus are flat and do not show a peak or dip in G in between the quantised values. The appropriate contact resistance was subtracted.

Although the device seems to be inhomogeneous, when a perpendicular magnetic field B was applied, a quantised Hall effect could be observed between contacts A and B of device HC1. Figure 10.2 a) shows a colour scale plot of the two-terminal conductance G between contacts A and B as a function of B and the gate V_g . The first conductance plateau to be observed lies at $4 e^2/h$, belonging to the $\nu = \pm 4$ state characteristic for bilayer graphene [111]. At higher fields, the broken symmetry states at $\nu = \pm 2$ and ± 1 appear [121]. The $\nu = \pm 3$ state is only very weakly developed and not readily visible in the colour scale plot. Furthermore, an insulating phase develops at the CNP above a field of ~ 1 T, which we assign to the $\nu = 0$ state. This is in contrast to the observations made in the two-terminal devices presented in the previous chapter, which retained a

low but finite conductance in the $\nu = 0$ state.

Figure 10.2 b) shows G in dependence on V_g for different magnetic fields. For each given B , the conductance increases steadily until a plateau is reached. After remaining constant on the plateau, the conductance increases again steadily. From the mixing of σ_{xx} and σ_{xy} a different behaviour for a longer ($3 \mu\text{m}$) than wide ($1 \mu\text{m}$) two-terminal device is expected [50, 51]: the conductance plateaus should be located on peaks in the magneto-conductance. In contrast, the observed behaviour is indicative for a square geometry. This interpretation is further supported by the absence of a measurable quantised Hall voltage between contacts C and D, indicating that the edge states do not pass between C and D. We would like to add that such a deviation from the expected and the measured shape of the two-terminal magneto-conductance occurred in many of the investigated devices. Moreover, the regions of disordered graphene might contribute to the observed series resistance R_c .

A slight asymmetry in the evolution of the Hall plateaus is found in most of our devices for hole-like and electron-like charge carriers. Such is also visible in fig. 10.2 a), where the conductance plateaus appear at higher magnetic fields on the electron side ($V_g > 0$) compared to the hole side. To some extent, this is due to the asymmetric broadening of the plateaus originating most likely from different localised states available to the charge carriers. However, even after accounting for the broadening and compensating for a CNP not at zero V_g , a difference of 5–10% in B can be observed. Moreover, we often observe a curvature of the Hall plateaus, as can be seen in fig. 10.2 a) for the $\nu = +4$ state near $V_g = 0$ V and $B < 1$ T. Since the strength of the magnetic field can be regarded as very well established, and the filling factor should also be fairly precise, the only open parameter from eq. 5.4 is the carrier density n . Originally, we assumed that $n \propto V_g$ (eq. 2.10). To receive a non-linear conversion from V_g to n , the capacitances of the gate and the bilayer graphene would have to change. This could occur, if the capacitance of the BLG is reduced to the same order of magnitude as the gate capacitance and hence could not be neglected any more. Yet, estimating the graphene's capacitance with $C_{BLG}^{\square} = 2m^*e^2/(\pi\hbar^2)$ yields a several orders of magnitude larger value than the gate capacitance. An alternative explanation is an effect originating from the band structure itself. For example, trigonal warping could introduce low-energy distortions [20], which might be responsible for the curvatures at low magnetic fields.

10.2. Measurement of Quantised σ_{xy}

With view to the measurement of σ_{xy} , the homogeneity of the devices had to be improved. In contrast to the sample HC1, it was possible to receive a better result in a second suspended bilayer graphene sample, named HC2 in the following. For

the device HC1, it was not possible to widen the region of high quality by further current annealing. Trying to anneal different contact pairs led to a CNP between the last annealed contact pair, but removed any previously existing CNP between the other contacts. We therefore speculate, that there is still some residue left on the graphene, which becomes mobile when heated and condenses near the contacts which were not involved in the annealing.

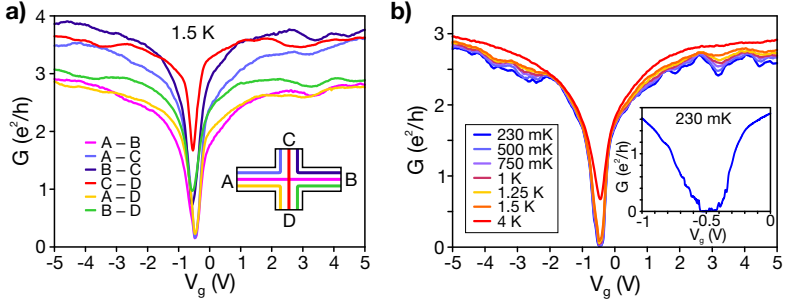


Figure 10.3.: Measured two-terminal conductance G as a function of the gate V_g in device HC2. **a)** The conductance between all possible terminals at 1.5 K. A charge neutrality point can be observed for all contacts at $V_g \approx -0.5$ V. The inset shows a schematic of the device and the labelling of the contacts. **b)** G between contacts A and B as a function of V_g for temperatures ranging from 230 mK to 4 K. For temperatures up to 1.5 K, the minimal conductance G_{min} at the CNP is negligible. At 4 K, G_{min} raises to $0.7 e^2/h$. The inset shows that the bilayer graphene becomes insulating at the CNP at 230 mK.

However, in device HC2 it was possible to receive a fairly homogeneous device after current annealing. In fig. 10.3 a), the measured conductance G is shown for all contact pairs. A CNP can be found for all configurations (inset of fig. 10.3 a)) at $V_g \approx -0.5$ V. Hence, the region of the cleaned graphene must span all contacts. The lowest conductance at the CNP can be found for combinations involving contact A, implying that the clean graphene originates near there. It is worth noting, that the minimum conductance at the CNP is lower than in sample HC1.

Subsequently, we study the temperature dependence of G between contacts A and B, which are connected through a bilayer graphene flake of length $L = 3 \mu\text{m}$ and width $W = 1 \mu\text{m}$. Figure 10.3 b) summarises our findings. At the highest investigated temperature of $T = 4$ K, a minimum of $G_{min} = 0.7 e^2/h$ is observed at the CNP. With decreasing T , the conductance at higher V_g is slightly reduced.

However, near the CNP, G_{min} approaches zero. The inset in fig. 10.3 b) shows that for $T = 230$ mK, the graphene becomes insulating at the CNP at $V_g \approx -0.5$ V. Such an insulating phase at low charge carrier density at zero magnetic field could also be observed in [131]. On the other hand, the part graphene from contact C to D ($L = 1.6 \mu\text{m}$, $W = 1 \mu\text{m}$) retained a finite G_{min} of about $1.3 e^2/h$ at 230 mK. We will study the properties of this insulating state later on in greater detail, and focus first on the quantum Hall effect (QHE).

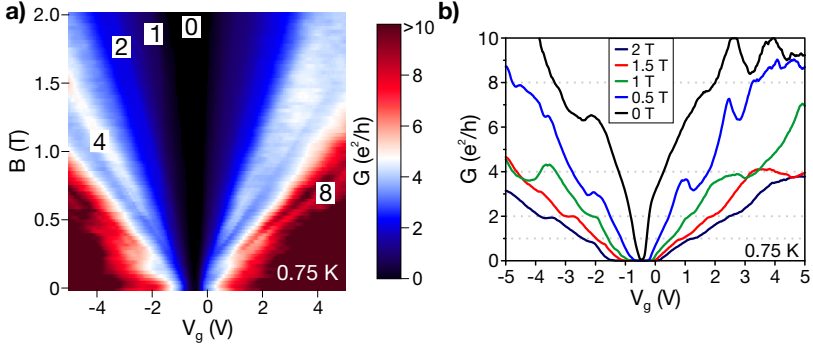


Figure 10.4.: Two-terminal quantum Hall effect at 0.75 K between contacts A and B of device HC2. **a)** Colour scale plot of the conductance G as a function of the magnetic field B and the gate voltage V_g . Several quantised conductance plateaus are visible. Values of 8 , 4 , 2 and $1 e^2/h$ can be observed for holes and electrons. An insulating state extends down to $B = 0$ T at the CNP, labelled as 0 . **b)** G in dependence on V_g for several magnetic fields. The plateaus at $8 e^2/h$ and $4 e^2/h$ reside on peaks, whereas the lower conducting plateaus integrate into the slope. The appropriate R_c was subtracted.

The measurement set-up is as follows for the QHE investigations. An AC voltage of $50 \mu\text{V}$ is applied over contacts A and B. The current between A and B is measured simultaneously to the voltage over contacts C and D.

In a perpendicular magnetic field B , the bilayer graphene between contacts A and B shows a QHE which is distinct from the one observed in sample HC1. In fig. 10.4 a) a colour scale plot of G as a function of B and V_g at 0.75 K is shown. Whereas several features evolve fan-like with B and V_g , the step-like evolution as seen in fig. 10.2 a) is absent. Nonetheless, conductance plateaus at $8 e^2/h$, $4 e^2/h$, $2 e^2/h$ and $1 e^2/h$ are identifiable, for both holes and electrons. The insulating state at $\nu = 0$ extends to zero magnetic field. A closer inspection of the shape of

the Hall plateau is shown in fig. 10.4 b). The plateaus at $8 e^2/h$ and $4 e^2/h$ lie at local maxima, as expected for a geometry with $L > W$ [50] and consistent with the size of the flake of $L = 3 \mu\text{m}$ and $W = 1 \mu\text{m}$. This confirms our observation that sample HC2 is more homogeneous than HC1. On the other hand, the plateaus below $4 e^2/h$ return to being integrated into a continuous slope. One possible explanation for this behaviour is that the plateaus are not fully developed at a temperature of 0.75 K and a higher magnetic field would be required to see their true shape. However, they move too quickly out of the gate range to be measured at high fields.

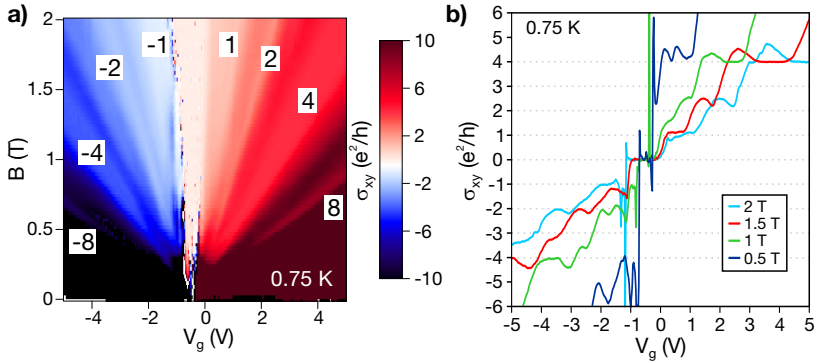


Figure 10.5.: The measured Hall conductivity σ_{xy} between contacts C and D of device HC2 at 0.75 K. **a)** Colour scale plot of σ_{xy} as a function of the magnetic field B and the gate voltage V_g . Plateaus can be identified at ± 8 , ± 4 , ± 2 and $\pm 1 e^2/h$. The onset of the quantisation occurs at a field of $B \approx 0.3$ T. A plateau at $\pm 3 e^2/h$ is only weakly developed. **b)** σ_{xy} as function of V_g for the indicated magnetic fields at 0.75 K.

In addition to the two-terminal G between contacts A and B, the Hall cross geometry allows for the simultaneous measurement of the Hall conductivity σ_{xy} via the contacts C and D (inset of fig. 10.3 a)). A colour scale plot of σ_{xy} in device HC2 is shown in fig. 10.5 a) in dependence on B and V_g . Plateaus can be identified at the same filling factors as for the two-terminal QHE. However, the plateaus are better developed and since it is a four-terminal measurement, no contact resistance R_c has to be estimated and subtracted. Ideally, σ_{xy} should increase steadily until an integer filling factor ν is reached, form a conductance plateau at $\nu \cdot e^2/h$ and then resume its steady increase with V_g . In the presented measurement, σ_{xy} deviates frequently from the ideal behaviour. We attribute this to

a finite ρ_{xx} component in the Hall signal, due to the small size of the device. Further, one can calculate the charge carrier mobility from the Hall conductance, since the field effect mobility is meaningless in the presence of a transport-gap. The extraction of the charge carrier concentration is straight forward with $n = \nu Be/h$, where ν is the filling factor of a conductance plateau measured at the field B . A mobility of $\sim 40\,000\text{ m}^2/\text{Vs}$ is found for the bilayer graphene between contacts A and B, and $\sim 10\,000\text{ m}^2/\text{Vs}$ for the part between C and D. Whereas this is lower than some of the reported field effect mobilities for suspended BLG [121, 131–133], we would like to stress that ours are to the best of our knowledge the first mobilities gained from the Hall signal of suspended BLG.

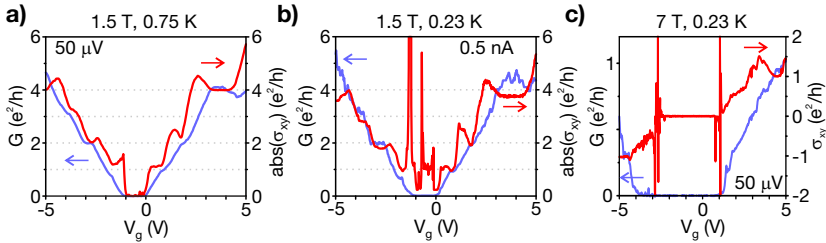


Figure 10.6.: The measured Hall conductance σ_{xy} between contacts C and D of device HC2 and the two-terminal conductance G between A and B as function of the gate voltage V_g . **a)** Voltage bias of $50\ \mu\text{V}$ at $1.5\ \text{T}$ and $0.75\ \text{K}$. For convenience, the absolute value of σ_{xy} is shown. The Hall plateaus are developed and coincide for σ_{xy} and G reasonably well. At $\nu = 0$ around V_g , both σ_{xy} and G appear to go to zero. **b)** Current bias. The plateaus are less well developed than in a). G goes to zero, whereas σ_{xy} fluctuates strongly. **c)** G and σ_{xy} at $7\ \text{T}$ and $230\ \text{mK}$. No plateaus at fractional filling factors are observable. Contact resistances were subtracted.

Of great interest is the insulating state at $\nu = 0$, which extends to zero magnetic field in HC2. In recent literature, a wealth of possible spontaneous ground states was predicted. One suggestion was the Quantum Anomalous Hall (QAH) state, which was predicted to support charge edge states [60–62]. However, most other spontaneous states do not support charge edge states [56].

The measured Hall conductance did not show non-zero quantised values at $B = 0\ \text{T}$, nor up to small fields of $100\ \text{mT}$. A minute voltage was detectable between the Hall probes C and D, but it likely originates from a non-perfect arrangement of the electrodes and the same mixing of ρ_{xx} into the signal as observed above in the quantum Hall regime.

A further complication of the investigation of the insulating state originates in the measurement set-up. Since we apply a small AC voltage of $50 \mu\text{V}$ to drive and measure a current, the large resistance at $\nu = 0$ leads to a suppression of the current in XX -direction. Consequently, $G \rightarrow 0$, as shown in fig. 10.6 a). At the same time, $\sigma_{xy} \rightarrow 0$, which suggests that there is a Hall plateau at $\nu = 0$ and thus a Hall state. However, since the current along XX becomes zero, and we calculate $\sigma_{xy} = I_{xx}/V_{xy}$, we can only state that I_{xx} is faster reduced than V_{xy} . Moreover, the signal-phases measured at the lock-in amplifiers approaches 180° , symptomatic of purely capacitive coupling between the contacts and indicating that the measured data in the insulating state should be treated carefully.

Another attempt to measure the insulating state was performed with a small AC current bias of 0.5 nA , shown in fig. 10.6 b). To do so, an AC voltage is applied with the lock-in amplifier, and defines the current via a large resistor in series with the sample. Then the voltage drop over the terminals, V_{xx} and V_{xy} , can be detected. For similar conditions as in the voltage biased measurement, very similar features can be found with current bias, as shown in fig. 10.6 b). The small discrepancy in σ_{xy} between the expected and measured values at the conductance plateaus is an artefact from the detection of the diminutive signals in the device. However, at $\nu = 0$ the resistance increases and thus the voltage signal grows and should be more easily measurable. Yet the transition into the insulating state occurs very rapid at $V_g \approx -1 \text{ V}$ and $V_g \approx 0 \text{ V}$. The resistance of the device becomes of the order of the series resistor and hence it ceases to be current biased and experiences an ill-defined voltage bias. As a consequence, σ_{xy} oscillates in the insulating state between $V_g = -1 \text{ V}$ and $V_g = 0 \text{ V}$.

Finally, fig. 10.6 c) shows σ_{xy} and G as a function of V_g at 7 T . The conductance plateaus at $\nu = \pm 1$ are visible, but fractional values [133] cannot be found. Analogous to the suspended single layer graphene, the insulating state appears to be covering any fractional plateaus.

10.3. **dI/dV Spectroscopy and Evolution of the Gap in Magnetic Field**

An important difference between samples HC1 and HC2 is the conductance at the CNP, G_{min} . For sample HC1, a $G_{min} \approx 0.5 e^2/h$ is found at 230 mK between contacts A and B, comparable to G_{min} in the type B2 devices of the previous chapter. In contrast, the bilayer graphene between contacts A and B in device HC2 is insulating at the CNP, as demonstrated in fig. 10.3 b). In the following, dI/dV spectroscopy is used to investigate the properties of the state at low charge carrier densities and zero magnetic field in devices HC1 and HC2. The magnetic field dependence of the found features is then explored.

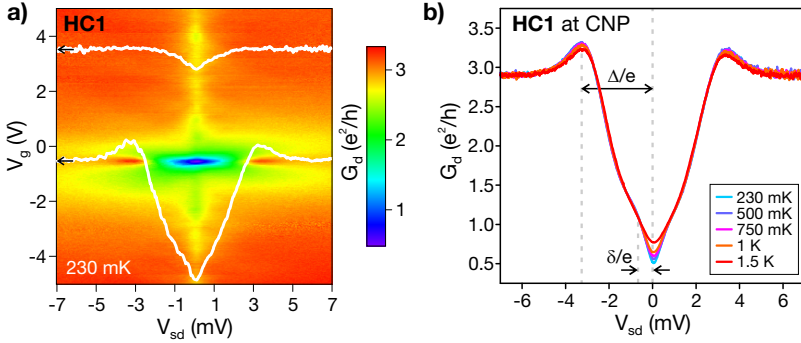


Figure 10.7.: Device HC1 at $B = 0$ T: **a)** Colour scale plot of the differential conductance G_d as function of the gate voltage V_g and source-drain bias voltage V_{sd} at 230 mK. At the CNP, $V_g = -0.5$ V, two gaps are visible. The larger gap, Δ , closes quickly as V_g is changed. The smaller gap, δ persists at higher charge carrier density. The overlaid line cuts, taken at V_g as indicated by the arrows, illustrate the gaps at the CNP and in the metallic regime. **b)** G_d as function of V_{sd} at the CNP for temperatures T from 230 mK to 1.5 K. The smaller gap, $\delta/e \approx 0.6$ mV, disappears as T is increased to 1.5 K. The larger gap, $\Delta/e \approx 3.3$ mV, remains unchanged in the investigated range of T .

First, we present the spectroscopy of the inhomogeneous bilayer graphene device HC1. Figure 10.7 a) shows a colour scale plot of the differential conductance G_d as a function of the gate voltage V_g and the applied source-drain bias voltage V_{sd} at zero magnetic field. At the CNP around $V_g = -0.5$ V, the effect of V_{sd} is the strongest. As $|V_{sd}|$ is increased, G_d increases from $0.5 e^2/h$ to about $3 e^2/h$ at $|V_{sd}| = 7$ mV. At $|V_{sd}| \approx 3.3$ mV a BCS-like peak feature appears in G_d . A larger gap, Δ , and a faint smaller gap, δ , can be identified. When accessing higher charge carrier concentrations n by tuning V_g away from the CNP, Δ closes whereas δ persists in the metallic regime. The temperature dependence, shown in fig. 10.7 b), provides further distinction between the two gaps. At 230 mK, we find that $\delta/e \approx 0.6$ mV and decreases the measured conductance from $0.9 e^2/h$ to $0.5 e^2/h$. On the other hand, the larger gap is $\Delta/e \approx 3.3$ mV and decreases G_d from $3 e^2/h$ to $0.9 e^2/h$. When the temperature is raised from 230 mK to 1.5 K, Δ remains unaffected. In contrast, δ is successively diminished and vanishes around 1.5 K.

Consequently, the dI/dV spectroscopy reveals features almost identical to the

gaps found in the two-terminal samples of type B2, shown in fig. 9.5. Interestingly, the conductance at which Δ saturates when the temperature is lowered, seems to be almost the same with $\sim 1 e^2/h$ for both HC1 and B2. But again, whereas HC1 transits into an insulating phase at $\nu = 0$, the B2 samples retained a finite G .

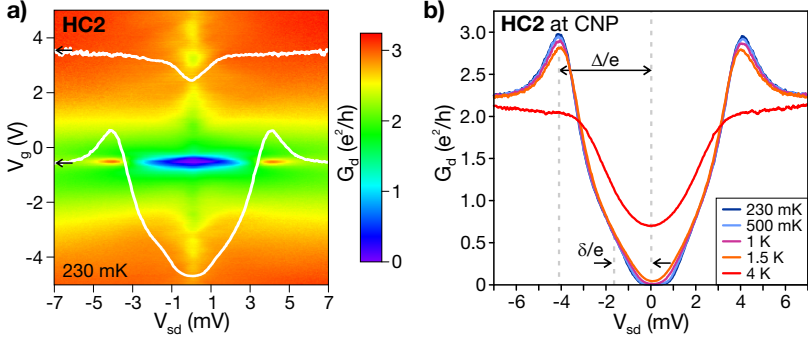


Figure 10.8.: Device HC2 at $B = 0$ T: **a)** Colour scale plot of the differential conductance G_d as function of the gate voltage V_g and source-drain bias voltage V_{sd} at 230 mK. At the CNP, $V_g = -0.5$ V, the device is fully insulating. With the application of V_{sd} a finite conductance is recovered. G_d increases with $|V_{sd}|$ and saturates around $2 e^2/h$ after increasing to $3 e^2/h$. Away from the CNP, only a small gap remains. The overlaid graphs show G_d as function of V_{sd} at the gate indicated by the arrows. **b)** G_d as function of V_{sd} at the CNP for temperatures T from 230 mK to 4 K. We identify two gaps by their temperature dependence. The smaller gap, $\delta/e \approx 1.6$ mV, is reduced as T is increased to 1.5 K and vanishes at 4 K. The larger gap, $\Delta/e \approx 4.1$ mV, remains unaffected up to 1.5 K. At 4 K, the BCS-like peaks in G_d are suppressed and Δ is reduced.

Conversely, the more homogeneous graphene in device HC2 differs from HC1 and the B2-type samples in the dI/dV spectroscopy. A colour scale plot of G_d as function of V_g and V_{sd} at 230 mK is shown in fig. 10.8 a). At the CNP around $V_g = -0.5$ V, a large gap suppresses the conductance at $V_{sd} = 0$ mV. For finite V_{sd} the conductance is recovered and reaches a BCS-like peak at $|V_{sd}| \approx 4.1$ mV before it saturates at $2.3 e^2/h$, as can be seen from the overlaid line cut. In contrast to HC1, the cross-over from the larger to the smaller gap is not obvious. Away from the CNP at large n , only a small gap remains in V_{sd} . The temperature dependence of G_d as a function of V_{sd} at the CNP is shown in fig. 10.8 b) for a range from 230 mK to 4 K. We can identify two gaps by their differently strong

dependence on T . The conductance at $|V_{sd}| \lesssim 1.6$ mV, increases slightly when T is raised from 230 mK to 1.5 K. In contrast, the curves at $|V_{sd}| > 1.6$ mV lie on top of each other. Hence, it is reasonable to assume, that this feature corresponds to the smaller gap δ , which exhibits a similar dependence in HC1. The larger gap, $\Delta/e \approx 4.1$ mV, only starts closing at 4 K, where δ is not visible any more. A similar, fully gapped state in suspended bilayer graphene at zero external magnetic field was also reported in [131].

The presence of both gaps in a low conducting and an insulating BLG device implies that the phenomena in both devices are identical, only differing in the size of Δ and δ .

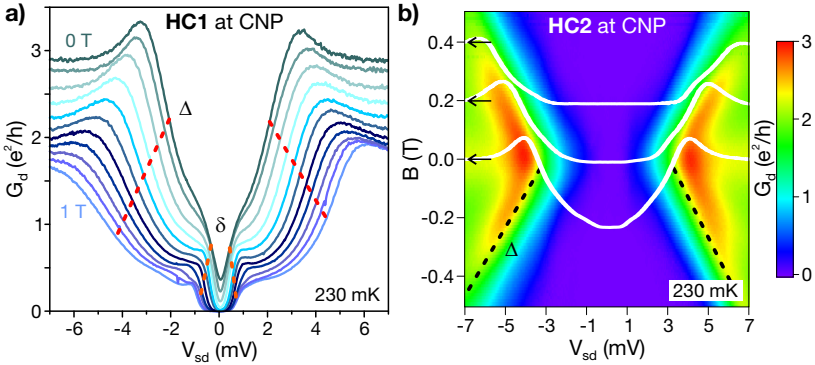


Figure 10.9.: Evolution of the differential conductance G_d with the applied source-drain bias V_{sd} and the magnetic field B at 230 mK. **a)** Device HC1 at the CNP. At $B = 0$ T, the gaps $\Delta/e \approx 3$ mV and $\delta/e \approx 0.6$ mV can be found. Increasing B to 1 T yields a widening of both gaps. Whereas Δ grows with 2.8 meV/T, the smaller gaps δ only grows with ~ 0.6 meV/T. G_d at 1 T is reduced by Δ from $1.6 e^2/h$ to $0.4 e^2/h$. The small gap δ decreases G_d further to zero. The dotted lines are guides to the eye to illustrate the evolution of the gaps in B . **b)** In HC2, the insulating region widens in V_{sd} as $B \rightarrow \pm 0.5$ T. Only Δ can be observed to grow with ~ 5.5 meV/T, as indicated by the dotted lines. The evolution of δ is not reliably traceable, as δ is very faint. The overlaid curves show G_d as function of V_{sd} at the fields indicated by the arrows.

Moreover, we investigated the magnetic field dependence of the gapped states at low n in HC1 and HC2. Several of the predicted spontaneous ground states are of magnetic origin [56, 61] or pseudospin magnets [58, 59, 62, 63] and the

evolution with B could provide further insights into the nature of the actually observed state.

Figure 10.9 compares the evolution of the gaps at the CNP in perpendicular B for HC1 and HC2.

In device HC1, both gaps Δ and δ grow when B is increased, as shown in fig. 10.9 a). We determine the magnetic field dependence of both gaps by tracing the inflection points in $G_d(V_{sd})$. For δ , a linear increase with 0.6 ± 0.07 meV/T can be extracted. Comparison to the Zeeman energy, $E_Z = g\mu_B B$, yields a dependence of the same order of magnitude with ~ 0.12 meV/T. In contrast, we find that Δ increases faster but also linearly with 2.8 ± 0.1 meV/T. Further, the graphene becomes fully gapped for $B > 0.5$ T. At $B = 1$ T, Δ reduces G_d from $1.6 e^2/h$ at large V_{sd} to about $0.4 e^2/h$ at $|V_{sd}| \approx 1$ mV. From there on, δ suppresses the conductance.

For HC2, we present our findings in fig. 10.9 b). At the CNP and 230 mK, HC2 is already in a fully gapped state at zero magnetic field. As B is tuned away from zero, the insulating region in V_{sd} grows. Analogue to HC1, we find a linear increase of Δ with $|B|$, and a growth of the gap of 6.1 ± 0.7 meV/T. This is twice as fast as Δ in HC1 and implies that not only the size of Δ , but also its evolution in B depends on the cleanliness of the graphene, as HC2 is the cleaner and more homogeneous BLG device. In difference to HC1, the smaller gap δ is not readily observable in HC2. The overlaid curves in fig. 10.9 b) show a small change in the slope of G_d at $V_{sd} = 5$ mV for 0.4 T. However, the feature is too faint to trace it reliably in magnetic field. Furthermore, G_d does not exhibit hysteresis as B changes sign.

In both devices, we find gaps that evolve linearly with B , but retain a (device dependent) finite size at $B = 0$ T. Therefore, a possible explanation for these observations is a ferromagnetic quantum Hall state, which would spin polarise the bilayer graphene [58]. However, a state in which the real electron spin is polarised should be de-polarisable when the direction of the magnetic field is inverted and hence the gaps should close. Yet no such reduction of Δ is visible in fig. 10.9 b). Consequently, we speculate that the observed ferromagnet is in one of the pseudospins [56, 59, 62], or that the phase is a layer anti-ferromagnet [63].

10.4. Summary

We presented two different suspended bilayer graphene devices of a Hall cross geometry. One in which the graphene is only clean in the vicinity of one of the four contacts, named HC1. The other sample is more homogeneous and displays a CNP between all contact pairs, HC2.

Further, we reported measurements of σ_{xy} in HC2. Quantised conduction plateaus corresponding to $\nu = \pm 8, \pm 4, \pm 3, \pm 2$ and ± 1 could be found. We

explained the non-triviality of experimental proof of a conductance plateau at $\nu = 0$ in the Hall cross geometry.

Moreover, the magnetic field dependence of the spontaneous gaps found in dI/dV spectroscopy was explored. We compared the partially gapped HC1 and the fully gapped HC2 and observed a linear increase of the magnitude of the gaps with B . The larger gap in HC1, Δ , grows with 2.8 meV/T, whereas the smaller one, $\delta/B = 0.6$ meV/T, increases nearly with the Zeeman energy. The only clearly visible gap in HC2, Δ , is larger than the one found in HC1. It further grows faster with 6 meV/T. We speculate, that the gapped ground state at zero external magnetic field is of pseudospin origin.

SUMMARY AND OUTLOOK

In the course of this thesis, we have presented experimental results on diffusive single layer graphene contacted by superconducting electrodes, and showed data on ultraclean interacting suspended single layer and bilayer graphene.

In a first step, we measured the universal conductance fluctuations in single layer graphene on a SiO_2 substrate, with electrodes in the superconducting and the normal conducting state. The graphene of length $L = 1.3 \mu\text{m}$ put the device in a diffusive transport regime. Nonetheless, we found that the phase coherence length $l_\phi \gtrsim L/2$ because of an observed enhancement of the UCF by a factor 1.4–2 when the electrodes were in a superconducting state. The absolute magnitude of the UCF were considerably lower than e^2/h . We could show that the constant series resistance of the two-terminal measurement set-up masked the true magnitude of the UCF. Furthermore, the UCF were found to be nearly constant when changing the charge carrier density, after the appropriate series resistance had been subtracted.

Since the phase coherence length is not the limiting scale in our devices, a next step would be to improve the mobility of the graphene. The most promising approach is to either remove the SiO_2 substrate or replace it by one with less charged impurities, such as boron nitride [101] or similar materials.

The second field that was covered in this thesis was suspended, ultraclean and interacting graphene contacted with normal conducting electrodes. A hydrofluoric acid etch was used to remove the SiO_2 . First, we investigated suspended single layer graphene in a two-terminal geometry. The quantum Hall effect (QHE) expressed at very low magnetic fields B . The $\nu = \pm 2$ state extended to vanishing magnetic fields. We further observed an insulating phase at low charge carrier densities for B larger than a critical field. The sample's resistance increased exponentially with B and showed no temperature dependence for the investigated range of 230 mK to 1.5 K.

Next, our results on suspended two-terminal bilayer graphene were introduced. Two distinct types of samples were found: B1 showed a $\nu = \pm 4$ state that extended to very low B and further exhibited a gap-like feature, Δ , at $B = 0$ T that reduced

the conductance from $\sim 8 e^2/h$ to $4 e^2/h$ at low carrier densities. The QHE revealed a partial lifting of the zero-energy Landau level with an additional plateau of $2 e^2/h$ and an insulating state at $\nu = 0$, which was found to be temperature activated. On the other hand, samples of type B2 were fully lifted in the zero-energy Landau level, with a plateau sequence of $3 e^2/h$, $2 e^2/h$ and $1 e^2/h$. They remained conductive even in fields of up to 8 T, but showed a low conductance at the charge neutrality point when no B was applied. Moreover, we identified two gap features in dI/dV spectroscopy, which occurred spontaneously at $B = 0$ T. A larger gap, Δ , only showed near the CNP, whereas the smaller one, δ , persisted in the metallic regime.

In the last part, our findings on suspended bilayer graphene Hall crosses were presented. We could investigate the homogeneity of the current annealed graphene and found varying success. The cleanest sample supported a full lifting of the zero-energy Landau level and allowed for a measurement of the Hall conductance. We could not observe a quantised conductance at zero B , nor in the $\nu = 0$ state. Furthermore, we presented a fully developed transport gap in dI/dV spectroscopy and compared its evolution in magnetic field to the partially gapped state of type B2.

As we speculate that the spontaneous ground state is of a magnetic origin, an experiment with a tilted magnetic field could help to identify the exact nature of the state. The independent control over Zeeman splitting and Landau level quantisation should distinguish a ferromagnetic state from an anti-ferromagnetic or a pseudospin magnet.

Bibliography

- [1] P. R. Wallace, *Phys. Rev.* **71**, 622 (1947).
- [2] D. P. DiVincenzo and E. J. Mele, *Phys. Rev. B* **29**, 1685 (1984).
- [3] L. Radushkevich and V. Lukyanovich, *Zurn Fistic Chim* **26**, 88 (1952).
- [4] S. Iijima, *Nature* **354**, 56 (1991).
- [5] H. W. Kroto, J. R. Heath, S. C. O'Brien, R. F. Curl, and R. E. Smalley, *Nature* **318**, 162 (1985).
- [6] K. S. Novoselov, A. K. Geim, S. V. Morozov, D. Jiang, Y. Zhang, S. V. Dubonos, I. V. Grigorieva, and A. A. Firsov, *Science* **306**, 666 (2004).
- [7] S. Bae, H. Kim, Y. Lee, X. Xu, J.-S. Park, Y. Zheng, J. Balakrishnan, T. Lei, H. Ri Kim, Y. I. Song, Y.-J. Kim, K. S. Kim, B. Ozyilmaz, J.-H. Ahn, B. H. Hong, and S. Iijima, *Nat Nano* **5**, 574 (2010).
- [8] K. v. Klitzing, G. Dorda, and M. Pepper, *Phys. Rev. Lett.* **45**, 494 (1980).
- [9] K. S. Novoselov, Z. Jiang, Y. Zhang, S. V. Morozov, H. L. Stormer, U. Zeitler, J. C. Maan, G. S. Boebinger, P. Kim, and A. K. Geim, *Science* **315**, 1379 (2007).
- [10] M. O. Goerbig, *Rev. Mod. Phys.* **83**, 1193 (2011).
- [11] A. H. Castro Neto, F. Guinea, N. M. R. Peres, K. S. Novoselov, and A. K. Geim, *Rev. Mod. Phys.* **81**, 109 (2009).
- [12] S. Das Sarma, S. Adam, E. H. Hwang, and E. Rossi, *Rev. Mod. Phys.* **83**, 407 (2011).
- [13] M. I. Katsnelson, K. S. Novoselov, and A. K. Geim, *Nature Phys.* **2**, 620 (2006).
- [14] C. W. J. Beenakker, *Rev. Mod. Phys.* **80**, 1337 (2008).
- [15] M. I. Katsnelson, *EPJ B* **51**, 157 (2006).

- [16] J.-C. Charlier, J.-P. Michenaud, and X. Gonze, *Phys. Rev. B* **46**, 4531 (1992).
- [17] P. Lauffer, K. V. Emtsev, R. Graupner, T. Seyller, L. Ley, S. A. Reshanov, and H. B. Weber, *Phys. Rev. B* **77**, 155426 (2008).
- [18] P. Poncharal, A. Ayari, T. Michel, and J.-L. Sauvajol, *Phys. Rev. B* **78**, 113407 (2008).
- [19] M. Dresselhaus and G. Dresselhaus, *ADV. PHYS.* **51**, 1 (2002).
- [20] E. McCann and V. I. Fal'ko, *Phys. Rev. Lett.* **96**, 086805 (2006).
- [21] E. McCann, D. S. Abergel, and V. I. Fal'ko, *EPJ - Special Topics* **148**, 91 (2007).
- [22] E. McCann, D. S. Abergel, and V. I. Fal'ko, *Solid State Commun.* **143**, 110 (2007).
- [23] H. Min, B. Sahu, S. K. Banerjee, and A. H. MacDonald, *Phys. Rev. B* **75**, 155115 (2007).
- [24] M. Mucha-Kruczyński, I. L. Aleiner, and V. I. Fal'ko, *Phys. Rev. B* **84**, 041404 (2011).
- [25] N. W. Ashcroft and N. D. Mermin, *Solid State Physics* (Thomson Learning, London, 1976).
- [26] K. Bolotin, K. Sikes, Z. Jiang, M. Klima, G. Fudenberg, J. Hone, P. Kim, and H. Stormer, *Solid State Commun.* **146**, 351 (2008).
- [27] B. L. Altshuler, *JETP Lett.* **41**, 648 (1985).
- [28] P. A. Lee and A. D. Stone, *Phys. Rev. Lett.* **55**, 1622 (1985).
- [29] Y. Imry, *EPL* **1**, 249 (1986).
- [30] P. A. Lee, A. D. Stone, and H. Fukuyama, *Phys. Rev. B* **35**, 1039 (1987).
- [31] M. Büttiker, *Phys. Rev. B* **38**, 9375 (1988).
- [32] S. Datta, *Electronic transport in mesoscopic systems* (Cambridge University Press, Cambridge UK, 1995).
- [33] A. Rycerz, J. Tworzydło, and C. W. J. Beenakker, *EPL* **79**, 57003 (2007).

- [34] J. Tworzydło, C. W. Groth, and C. W. J. Beenakker, Phys. Rev. B **78**, 235438 (2008).
- [35] M. Y. Kharitonov and K. B. Efetov, Phys. Rev. B **78**, 033404 (2008).
- [36] V. V. Cheianov, V. I. Fal'ko, B. L. Altshuler, and I. L. Aleiner, Phys. Rev. Lett. **99**, 176801 (2007).
- [37] H. B. Heersche, P. Jarillo-Herrero, J. B. Oostinga, L. M. K. Vandersypen, and A. F. Morpurgo, Nature **446**, 56 (2007).
- [38] L. Hofstetter, S. Csonka, J. Nygard, and C. Schonenberger, Nature **461**, 960 (2009).
- [39] J. Bardeen, L. N. Cooper, and J. R. Schrieffer, Phys. Rev. **108**, 1175 (1957).
- [40] M. Tinkham, *Introduction to superconductivity* (Dover Publications, Mineola, New York, 2004).
- [41] W. Meissner and R. Ochsenfeld, Naturwissenschaften **21**, 787 (1933).
- [42] A. Andreev, Sov. Phys. JETP **19**, 1228 (1964).
- [43] G. E. Blonder, M. Tinkham, and T. M. Klapwijk, Phys. Rev. B **25**, 4515 (1982).
- [44] R. C. Dynes, V. Narayanamurti, and J. P. Garno, Phys. Rev. Lett. **41**, 1509 (1978).
- [45] A. Plecenik, M. Grajcar, S. Benacka, P. Seidel, and A. Pfuch, Phys. Rev. B **49**, 10016 (1994).
- [46] C. W. J. Beenakker, *Mesoscopic Quantum Physics*, edited by E. Akkermans, G. Montambaux, J.-L. Pichard, and J. Zin-Justin (North Holland, Amsterdam, 1995).
- [47] I. K. Marmoros, C. W. J. Beenakker, and R. A. Jalabert, Phys. Rev. B **48**, 2811 (1993).
- [48] E. H. Hall, Am. J. Math. **2**, 287 (1879).
- [49] M. O. Goerbig, arxiv:0909:1998 (2009).
- [50] D. A. Abanin and L. S. Levitov, Phys. Rev. B **78**, 035416 (2008).
- [51] J. R. Williams, D. A. Abanin, L. DiCarlo, L. S. Levitov, and C. M. Marcus, Phys. Rev. B **80**, 045408 (2009).

- [52] A. K. Geim and K. S. Novoselov, *Nature Mater.* **6**, 183 (2007).
- [53] K. Novoselov, D. Jiang, F. Schedin, T. Booth, V. Khotkevich, S. Morozov, and A. Geim, *Proc. Natl. Acad. Sci. U.S.A.* **102**, 10451 (2005).
- [54] K. Yang, *Solid State Commun.* **143**, 27 (2007).
- [55] M. Ezawa, *J. Phys. Soc. Jpn.* **76**, 094701 (2007).
- [56] Y. Barlas, K. Yang, and A. H. MacDonald, arXiv:1110.1069 (2011).
- [57] K. Nomura and A. H. MacDonald, *Phys. Rev. Lett.* **96**, 256602 (2006).
- [58] R. Nandkishore and L. Levitov, *Phys. Rev. Lett.* **104**, 156803 (2010).
- [59] H. Min, G. Borghi, M. Polini, and A. H. MacDonald, *Phys. Rev. B* **77**, 041407 (2008).
- [60] R. Nandkishore and L. Levitov, arXiv:1002.1966 (2010).
- [61] R. Nandkishore and L. Levitov, *Phys. Rev. B* **82**, 115124 (2010).
- [62] F. Zhang, J. Jung, G. A. Fiete, Q. Niu, and A. H. MacDonald, *Phys. Rev. Lett.* **106**, 156801 (2011).
- [63] M. Y. Kharitonov, arXiv:1109.1553 (2011).
- [64] O. Vafek and K. Yang, *Phys. Rev. B* **81**, 041401 (2010).
- [65] P. Blake, E. Hill, A. Neto, K. Novoselov, D. Jiang, R. Yang, T. Booth, and A. Geim, *Appl. Phys. Lett.* **91**, 063124 (2007).
- [66] A. C. Ferrari, J. C. Meyer, V. Scardaci, C. Casiraghi, M. Lazzeri, F. Mauri, S. Piscanec, D. Jiang, K. S. Novoselov, S. Roth, and A. K. Geim, *Phys. Rev. Lett.* **97**, 187401 (2006).
- [67] D. Graf, F. Molitor, K. Ensslin, C. Stampfer, A. Jungen, C. Hierold, and L. Wirtz, *Nano Lett.* **7**, 238 (2007).
- [68] T. Dieing, O. Hollricher, and J. Toporski, eds., *Confocal Raman Microscopy* (Springer-Verlag Berlin Heidelberg, 2011).
- [69] A. C. Ferrari and J. Robertson, *Phys. Rev. B* **61**, 14095 (2000).
- [70] C. Stampfer, F. Molitor, D. Graf, K. Ensslin, A. Jungen, C. Hierold, and L. Wirtz, *Appl. Phys. Lett.* **91**, 241907 (2008).

- [71] Z. Ni, L. Ponomarenko, R. Nair, R. Yang, S. Anissimova, I. Grigorieva, F. Schedin, P. Blake, Z. Shen, E. Hill, *et al.*, *Nano Lett.* **10**, 3868 (2010).
- [72] M. Ishigami, J. H. Chen, W. G. Cullen, M. S. Fuhrer, and E. D. Williams, *Nano Lett.* **7**, 1643 (2007).
- [73] Z. Cui, *Nanofabrication* (Springer Science+Business Media, 2008).
- [74] K. Biswas and S. Kal, *Microelectron J* **37**, 519 (2006).
- [75] F. J. Feigl, D. R. Young, D. J. DiMaria, S. Lai, and J. Calise, *J. Appl. Phys.* **52**, 5665 (1981).
- [76] S. Morozov, K. Novoselov, M. Katsnelson, F. Schedin, L. Ponomarenko, D. Jiang, and A. Geim, *Phys. Rev. Lett.* **97**, 16801 (2006).
- [77] H. B. Heersche, P. Jarillo-Herrero, J. B. Oostinga, L. M. Vandersypen, and A. F. Morpurgo, *EPJ - Special Topics* **148**, 27 (2007).
- [78] N. Staley, C. Puls, and Y. Liu, *Phys. Rev. B* **77**, 155429 (2008).
- [79] C. Ojeda-Aristizabal, M. Ferrier, S. Gueron, and H. Bouchiat, *Phys. Rev. B* **79**, 165436 (2009).
- [80] V. Skákalová, A. B. Kaiser, J. S. Yoo, D. Obergfell, and S. Roth, *Phys. Rev. B* **80**, 153404 (2009).
- [81] J. Trbovic, N. Minder, F. Freitag, and C. Schönenberger, *Nanotechnology* **21**, 274005 (8 pp.) (2010).
- [82] Y.-F. Chen, M.-H. Bae, C. Chialvo, T. Dirks, A. Bezryadin, and N. Mason, *J. Phys.: Condens. Matter* **22**, 205301 (2010).
- [83] C. Ojeda-Aristizabal, M. Monteverde, R. Weil, M. Ferrier, S. Gueron, and H. Bouchiat, *Phys. Rev. Lett.* **104**, 186802 (2010).
- [84] M. F. Borunda, J. Berezovsky, R. M. Westervelt, and E. J. Heller, *ACS Nano* **5**, 3622 (2011).
- [85] D. Horsell, A. Savchenko, F. Tikhonenko, K. Kechedzhi, I. Lerner, and V. Fal'ko, *Solid State Commun.* **149**, 1041 (2009).
- [86] X. Du, I. Skachko, and E. Y. Andrei, *Phys. Rev. B* **77**, 184507 (2008).
- [87] F. Miao, W. Bao, H. Zhang, and C. N. Lau, *Solid State Commun.* **149**, 1046 (2009).

- [88] D. Jeong, J.-H. Choi, G.-H. Lee, S. Jo, Y.-J. Doh, and H.-J. Lee, *Phys. Rev. B* **83**, 094503 (2011).
- [89] C. Girit, V. Bouchiat, O. Naaman, Y. Zhang, M. F. Crommie, A. Zettl, and I. Siddiqi, *Nano Lett.* **9**, 198 (2009).
- [90] J.-H. Chen, C. Jang, S. Adam, M. S. Fuhrer, E. D. Williams, and M. Ishigami, *Nature Phys.* **4**, 377 (2008).
- [91] K. S. Novoselov, A. K. Geim, S. V. Morozov, D. Jiang, M. I. Katsnelson, I. V. Grigorieva, S. V. Dubonos, and A. A. Firsov, *Nature* **438**, 197 (2005).
- [92] Y. Zhang, Z. Jiang, J. P. Small, M. S. Purewal, Y.-W. Tan, M. Fazlollahi, J. D. Chudow, J. A. Jaszczak, H. L. Stormer, and P. Kim, *Phys. Rev. Lett.* **96**, 136806 (2006).
- [93] A. J. M. Giesbers, U. Zeitler, L. A. Ponomarenko, R. Yang, K. S. Novoselov, A. K. Geim, and J. C. Maan, *Phys. Rev. B* **80**, 241411 (2009).
- [94] J. G. Checkelsky, L. Li, and N. P. Ong, *Phys. Rev. B* **79**, 115434 (2009).
- [95] L. Zhang, Y. Zhang, M. Khodas, T. Valla, and I. A. Zaliznyak, *Phys. Rev. Lett.* **105**, 046804 (2010).
- [96] Z. Jiang, Y. Zhang, H. L. Stormer, and P. Kim, *Phys. Rev. Lett.* **99**, 106802 (2007).
- [97] K. I. Bolotin, F. Ghahari, M. D. Shulman, H. L. Stormer, and P. Kim, *Nature* **462**, 196 (2009).
- [98] X. Du, I. Skachko, F. Duerr, A. Luican, and E. Y. Andrei, *Nature* **462**, 192 (2009).
- [99] M. Y. Kharitonov, arXiv:1103.6285v1 (2011).
- [100] F. Ghahari, Y. Zhao, P. Cadden-Zimansky, K. Bolotin, and P. Kim, *Phys. Rev. Lett.* **106**, 046801 (2011).
- [101] C. R. Dean, A. F. Young, P. Cadden-Zimansky, L. Wang, H. Ren, K. Watanabe, T. Taniguchi, P. Kim, J. Hone, and K. L. Shepard, *Nat Phys* **7**, 693 (2011).
- [102] H. L. Stormer, D. C. Tsui, and A. C. Gossard, *Rev. Mod. Phys.* **71**, S298 (1999).
- [103] N. Tombros, A. Veligura, J. Junesch, M. H. D. Guimaraes, I. J. Vera-Marun, H. T. Jonkman, and B. J. van Wees, *Nat Phys* **7**, 697 (2011).

- [104] F. Guinea, M. I. Katsnelson, and A. K. Geim, *Nat Phys* **6**, 30 (2010).
- [105] W.-K. Tse, Z. Qiao, Y. Yao, A. H. MacDonald, and Q. Niu, *Phys. Rev. B* **83**, 155447 (2011).
- [106] N. Mounet and N. Marzari, *Phys. Rev. B* **71**, 205214 (2005).
- [107] W. Bao, F. Miao, Z. Chen, H. Zhang, W. Jang, C. Dames, and C. N. Lau, *Nat Nano* **4**, 562 (2009).
- [108] K. V. Zakharchenko, J. H. Los, M. I. Katsnelson, and A. Fasolino, *Phys. Rev. B* **81**, 235439 (2010).
- [109] T. M. G. Mohiuddin, A. Lombardo, R. R. Nair, A. Bonetti, G. Savini, R. Jalil, N. Bonini, D. M. Basko, C. Galiotis, N. Marzari, K. S. Novoselov, A. K. Geim, and A. C. Ferrari, *Phys. Rev. B* **79**, 205433 (2009).
- [110] E. McCann, K. Kechedzhi, V. I. Fal'ko, H. Suzuura, T. Ando, and B. L. Altshuler, *Phys. Rev. Lett.* **97**, 146805 (2006).
- [111] K. S. Novoselov, E. McCann, S. V. Morozov, V. I. Fal'ko, M. I. Katsnelson, U. Zeitler, D. Jiang, F. Schedin, and A. K. Geim, *Nature Phys.* **2**, 177 (2006).
- [112] D. C. Tsui, H. L. Stormer, and A. C. Gossard, *Phys. Rev. Lett.* **48**, 1559 (1982).
- [113] E. Wigner, *Phys. Rev.* **46**, 1002 (1934).
- [114] F. Zhang, H. Min, M. Polini, and A. H. MacDonald, *Phys. Rev. B* **81**, 041402 (2010).
- [115] E. V. Gorbar, V. P. Gusynin, and V. A. Miransky, *JETP Letters* **91**, 314 (2010).
- [116] E. McCann, *Phys. Rev. B* **74**, 161403 (2006).
- [117] J. B. Oostinga, H. B. Heersche, X. Liu, A. F. Morpurgo, and L. M. K. Vandersypen, *Nature Mater.* **7**, 151 (2008).
- [118] R. T. Weitz, M. T. Allen, B. E. Feldman, J. Martin, and A. Yacoby, *Science* **330**, 812 (2010).
- [119] S.-M. Choi, S.-H. Jhi, and Y.-W. Son, *Nano Lett.* **10**, 3486 (2010).
- [120] J. Moser, A. Barreiro, and A. Bachtold, *Applied Physics Letters* **91**, 163513 (2007).

- [121] B. E. Feldman, J. Martin, and A. Yacoby, *Nature Phys.* **5**, 889 (2009).
- [122] Y. Zhao, P. Cadden-Zimansky, Z. Jiang, and P. Kim, *Phys. Rev. Lett.* **104**, 066801 (2010).
- [123] D. A. Abanin, K. S. Novoselov, U. Zeitler, P. A. Lee, A. K. Geim, and L. S. Levitov, *Phys. Rev. Lett.* **98**, 196806 (2007).
- [124] S. Raghu, X.-L. Qi, C. Honerkamp, and S.-C. Zhang, *Phys. Rev. Lett.* **100**, 156401 (2008).
- [125] S. V. Morozov, K. S. Novoselov, M. I. Katsnelson, F. Schedin, D. C. Elias, J. A. Jaszczak, and A. K. Geim, *Phys. Rev. Lett.* **100**, 016602 (2008).
- [126] X. Du, I. Skachko, A. Barker, and E. Y. Andrei, *Nature Nanotech.* **3**, 491 (2008).
- [127] J. Martin, B. Feldman, R. Weitz, M. Allen, and A. Yacoby, *Phys. Rev. Lett.* **105**, 256806 (2010).
- [128] M. H. Devoret, D. Esteve, H. Grabert, G.-L. Ingold, H. Pothier, and C. Urbina, *Phys. Rev. Lett.* **64**, 1824 (1990).
- [129] D. A. Abanin, P. A. Lee, and L. S. Levitov, *Phys. Rev. Lett.* **96**, 176803 (2006).
- [130] I. Martin, Y. M. Blanter, and A. F. Morpurgo, *Phys. Rev. Lett.* **100**, 036804 (2008).
- [131] J. Velasco, Jr., L. Jing, W. Bao, Y. Lee, P. Kratz, V. Aji, M. Bockrath, C. N. Lau, C. Varma, R. Stillwell, D. Smirnov, F. Zhang, J. Jung, and A. H. MacDonald, *Nature Nanotech.* **7**, 156 (2012).
- [132] A. S. Mayorov, D. C. Elias, M. Mucha-Kruczynski, R. V. Gorbachev, T. Tudorovskiy, A. Zhukov, S. V. Morozov, M. I. Katsnelson, V. I. Fal'ko, A. K. Geim, and K. S. Novoselov, *Science* **333**, 860 (2011).
- [133] W. Bao, Z. Zhao, H. Zhang, G. Liu, P. Kratz, L. Jing, J. Velasco, D. Smirnov, and C. N. Lau, *Phys. Rev. Lett.* **105**, 246601 (2010).

APPENDIX A

FLAKE DEPOSITION

1. Cleaning of the wafer pieces:
 - a) 10 min sonication in acetone → 10 min sonication in 2-propanol
 - b) 30 min exposure to UV-ozone (Model 42-220, Jelight Company, USA)
2. UV-lithography for alignment marks:
 - a) Spin coating UV resist (ma-N 415, micro resist technology GmbH, Germany) at 5000 rpm, 2 s ramp, 40 s spin
 - b) Pre-bake for 60 s on hotplate at 100 °C
 - c) Exposure in UV mask aligner (MJB4, Süss MicroTec, Germany) for 10 s
 - d) Development for ca. 45 s in ma-D 332s (micro resist technology GMBH)
3. Metallisation
 - a) Evaporation of 2 nm titanium and 25 nm gold in a Balzers-Pfeiffer PLS 500, no cooling with liquid nitrogen required
 - b) Lift-off in acetone → sonication in acetone until lift-off complete → rinse in isopropanol
4. Reactive ion etching in Oxford Instruments Plasmalab^{80 Plus}:
 - a) Base pressure $5 \cdot 10^{-5}$ mbar, process pressure 25 mTorr, 8 sccm O₂, 16 sccm Ar, 10 W, 10 min
 - b) Immediately after opening the RIE chamber the tape with the graphite flakes is pressed on the wafer and gently rubbed with the thumb to improve sticking of the graphene to the wafer
5. Removing the tape and improving the yield:

A. Flake deposition

- a) Removing the Nitto tape in acetone: Wait until the tape goes off by itself, then remove the tape from the beaker. Rinse in isopropanol.
- b) Baking wafer on hotplate at 120 ° for 30 min
- c) Peel the graphene on the wafer with a fresh piece of tape
- d) Check optically for flakes and repeat peeling if too few are found

APPENDIX B

E-BEAM LITHOGRAPHY, METALLISATION AND HF ETCHING

PMMA spin coating

1. (*Optional*) Spin coating of PMMA/MA 33% (AR-P 617.03, Allresist, Germany): 4 s ramp, 40 s at 4000 rpm (\rightarrow 90 nm film).
10 min on hotplate at 180 °C.
2. Spin coating of PMMA (AR-P 671.09, Allresist, Germany), diluted with chlorobenzene to give a thickness of 200-400 nm: 4 s ramp, 40 s at 4000 rpm
3 min on hotplate at 180 °C.
3. Apply gold colloids (200 nm diameter) for focusing.

E-beam writing

All presented structures were written on a Zeiss Supra 40 SEM with an extraction voltage of 20 kV.

250 μm writefield:

Working distance : 16.9 mm

Area Step Size : 7.8 nm

Magnification : 240 \times

Area dose : 230 $\mu\text{As}/\text{cm}^2$

Aperture : 10 μm

Beam speed : <2 mm/s

Current : \sim 30 pA

2000 μm writefield:

Working distance : 16.9 mm

Area Step Size : 31 nm

Magnification : 30 \times

Area dose : 230 $\mu\text{As}/\text{cm}^2$

Aperture : 120 μm

Current : ~ 5 nA

Beam speed : < 80 mm/s

Development for 45 s in a solution of 4-Methylpentan-2-one (25 units) and isopropanol (75 units). Stopped in isopropanol.

Reactive ion etching of graphene

Process settings as for the wafer cleaning step in appendix A. The duration was reduced to 30 s - 1 min depending on the thickness of the flakes that should be etched.

Metallisation

Chromium and gold were evaporated with an e-gun in a Balzers-Pfeiffer PLS 500 system. The sample holder was cooled to between 0 $^{\circ}\text{C}$ and -10 $^{\circ}\text{C}$ with liquid nitrogen. The vacuum during evaporation was 10^{-5} - 10^{-7} mbar and the rates were kept between 0.5 $\text{\AA}/\text{s}$ and 1 $\text{\AA}/\text{s}$.

Lift-off was performed in acetone, followed by 10 min in fresh acetone at 40 $^{\circ}\text{C}$ and 10 min in warm isopropanol.

Al_2O_3 and TMAH

A thin (3 nm) film of aluminium was evaporated on the sample and left in the air to oxidise. After development of the PMMA mask, the Al_2O_3 layer was dissolved by dipping the sample for 10 s in a solution of 25% tetramethylammonium hydroxide (TMAH) in water, heated to 50 $^{\circ}\text{C}$.

After metallisation and lift-off, the TMAH-dip was repeated to remove the Al_2O_3 left on the graphene.

Hydrofluoric acid (HF) etch

Buffered HF was used to maintain a constant etch rate: 21 ml 40% HF, diluted in 248 ml H₂O with 155 g NH₄F

The etch rate was measured to be 40 nm/min at room temperature. Thus samples were etched for 4 min to remove 160 nm of SiO₂. After the etch, the reaction was stopped in water and the sample transferred to ethanol.

In order to dry the sample, critical point drying with CO₂ was used (Balzers CPD 030, Balzers AG, Liechtenstein) and the medium was exchanged 6-7×.

CURRICULUM VITAE

Frank Daniel Freitag
February 19 1983 born in Basel BS

Education

- | | |
|-----------|---|
| 1999–2002 | Gymnasium Münchenstein (C Typus) |
| 2003–2006 | Bachelor of Science in Nanosciences at the University of Basel |
| 2006–2008 | Master of Science in Nanosciences at the University of Basel
Master thesis in the group of Prof. A. Geim, Manchester:
"Scanning Probe Investigations and Lithography on Graphene" |
| 2008–2012 | PhD in experimental Physics at the University of Basel
PhD thesis in the group of Prof. C. Schönberger: "Graphene" |

For valuable lectures during my studies I am indebted to:

A. A'Campo, C. Bruder, G. Burkard, A. Bussmann-Holder, M. Calame, T. Christen, A. Engel, H.-J. Güntherodt, M. Hegner, K. Hencken, S. Goedecker, H.-J. Hug, J. Jourdan, B. Krusche, W. Meier, E. Meyer, C. Schönenberger, C. Vebert
H. Walser, H.-J. Wirz, D. Zumbühl

PUBLICATIONS

Publications

- *Giant Fluctuations and Gate Control of the g -factor in InAs Nanowire Quantum Dots*, S. Csonka, L. Hofstetter, F. Freitag, S. Oberholzer, T. S. Jespersen, M. Aagesen, J. Nygård and C. Schönenberger
Nano Lett. **8**, 3932-3935 (2008)
- *Nanolithography and manipulation of graphene using an atomic force microscope*, A.J.M. Giesbers, U. Zeitler, S. Neubeck, F. Freitag, K.S. Novoselov and J.C. Maan
Solid State Comm. **147**, 366–369 (2008)
- *From One Electron to One Hole: Quasiparticle Counting in Graphene Quantum Dots Determined by Electrochemical and Plasma Etching*, S. Neubeck, L.A. Ponomarenko, F. Freitag, A.J.M. Giesbers, U. Zeitler, S.V. Morozov, P. Blake, A.K. Geim and K.S. Novoselov
small **6**, 1469–1473 (2010)
- *Scanning probe lithography on graphene*, S. Neubeck, F. Freitag, R. Yang and K.S. Novoselov
Phys. Status Solidi B **247**, 2904–2908 (2010)
- *Superconductivity-enhanced conductance fluctuations in few-layer graphene*, J. Trbovic, N. Minder, F. Freitag and C. Schönenberger
Nanotechnology **21**, 274005 (2010)
- *Permalloy-based carbon nanotube spin-valve*, H. Aurich, A. Baumgartner, F. Freitag, A. Eichler, J. Trbovic and C. Schönenberger
Appl. Phys. Lett. **97**, 153116 (2010)

- *Conductance fluctuations in graphene devices with superconducting contacts in different charge density regimes*, F. Freitag, J. Trbovic and C. Schönenberger
Phys. Status Solidi B **248**, 2649–2652 (2011)
- *Spontaneously gapped ground state in suspended bilayer graphene*, F. Freitag, J. Trbovic, M. Weiss and C. Schönenberger
Phys. Rev. Lett. **108**, 076602 (2012)

Poster Contributions

- *Superconductivity enhanced conductance fluctuations in few-layer graphene ribbons*, F. Freitag, J. Trbovic, N. Minder and C. Schönenberger.
Poster at the International Winterschool on Electronic Properties in Novel Materials IWEPNM 2010 in Kirchberg i.T. (Austria), 6-13 March 2010.
- *Superconductivity enhanced conductance fluctuations in few-layer graphene ribbons*, F. Freitag, J. Trbovic, N. Minder and C. Schönenberger.
Poster at the Swiss Physical Society (SPS) annual meeting, 21-22 June 2010.
- *Spontaneously gapped ground state in suspended bilayer graphene*, F. Freitag, J. Trbovic, M. Weiss, and C. Schönenberger.
Poster at the Quantum Mesoscopic Conference, Rencontres de Moriond in LaThuile (IT), 13-20 March 2011.
- *Spontaneously gapped ground state in suspended bilayer graphene*, F. Freitag, J. Trbovic, M. Weiss, and C. Schönenberger.
Poster at the Graphene Week 2011 in Oberurgl, 24-29 April 2011.

ACKNOWLEDGEMENTS

First and foremost, I am very grateful to Christian Schönenberger for giving me the possibility to do my PhD in his group and even more for his guidance during the course of my thesis. His insights into physics and enthusiasm for science were a constant source of motivation.

Furthermore, I would like to thank Prof. Hélène Bouchiat and Dr. Jurgen Smet for making the effort of reading my thesis and for joining the Defence committee.

During my PhD studies I was lucky to have the support of Jelena Trbovic and Markus Weiss. Jelena started the graphene research in our group and supervised me for two and a half years. Markus then guided me through the remaining time. I sincerely thank both of you for the many discussions about physics and the tips and tricks that made the experimental work much easier. And, of course, for your input to my thesis.

Moreover, I could always learn something from the other low-temperature postdocs; Romain Maurand, Szabolcs Csonka and Andreas Baumgartner (whom I would like to thank additionally for his help with the BTK-model).

Office-life has been a pleasure thanks to all the people I shared it with over the time. Hagen Aurich (special thanks for permalloy-job!), Matthias Bräuninger, Samuel d'Hollosy, Alex Eichler, Gábor Fábrián, Lukas Hofstetter, Andreas Kleine, Oren Knopfmacher, Stefan Nau, Julia Samm, Jens Schindele and Peter Rickhaus. Every time I had a question, many answers came back and often lively debates developed. But not only scientific topics could be discussed, and the after-work-hours will also be fondly remembered.

The same holds true for all the other group members: Michel Calame, Claire Barrett, Wangyang Fu, Haichao Huang, Jianhui Liao, Jon Agustsson, Jan Brunner, Toni Fröhlich, Roman Huber, Cornelia Nef, Ralph Stoop, Alexey Tarasov, Mathias Wipf, Songmei Wu and Zheng-Ming Wu. The excursions with the whole group were highlights!

I am indebted to the secretaries, Astrid Kalt and Barbara Kammermann, for taking good care of all administrative matters encountered during the last years!

Further, I would like to acknowledge the people of the technical services and the workshops. Whenever something (complicated) was broken they had the time

Acknowledgements

and expertise to help quickly and efficiently. Especially Dominik Sifrig, Werner Erni, Daniel Sacker, Patrick Stöcklin and Bernd Heimann.

I appreciate that Kostya and Sören took the time to answer my questions about graphene and gave me precious advice.

Last but not least, I want to say thank you to my family and friends who gave me moral support during my studies and made this thesis possible.